UNIVERSITÀ DI PARMA

UNIVERSITÀ DEGLI STUDI DI PARMA

DOTTORATO DI RICERCA IN FISICA

CICLO XXXIII

From Data Storage to Quantum Computing:
a Combined Theoretical and Experimental Study of Molecular Nanomagnets for Information Technologies

Coordinatore:
Chiar.mo Prof. Stefano Carretta

Tutore:
Chiar.mo Prof. Stefano Carretta

Co-tutore:
Dr. Alessandro Chiesa

Dottorando:
Emilio Macaluso

Anni Accademici 2017/18 - 2019/20

Few may hear Galileo's song
Of tribulation
Adversities
Fuel for a living, feeds us all

Echo his madness
His heresy feeds us all

Spirit is fire
Uncompromising
Hidden hand, protect us from
The dead and dying

Spirit is fire
Feed on the senseless center

Contents

Abbreviations

MNM	Molecular NanoMagnet
SMM	Single-Molecule Magnet
SIM	Single-Ion Magnet
QIP	Quantum Information Processing
QC	Quantum Computing
QEC	Quantum Error Correction
INS	Inelastic Neutron Scattering
(cw)EPR	(continuous wave) Electron Paramagnetic Resonance
ZFS	Zero-Field Splitting
CF	Crystal Field
DFT	Density Functional Theory
(c)LDA	(constrained) Local Density Approximation
FWHM	Full Width at Half Maximum
RRM	Repetition Rate Multiplication
SQUID	Superconducting QUantum Interference Device
FGR	Fermi Golden Rule
TOF	Time Of Flight
CNOT	Controlled-NOT
CCNOT	Controlled-Controlled-NOT (Toffoli)
CZ	Controlled-Z
IT	Information Technology
NISQ	Noisy Intermediate Scale Quantum computers
TQC	Three-Qubit Code
ESE	Electron Spin Echo
DOS	Density Of States
QTM	Quantum Tunnelling of Magnetization
MB	Many-Body

Chapter 1

Molecular Nanomagnets: an Emerging Platform for Information Technology

1.1 MNM, fundamental properties and applications

Molecular nanomagnets (MNMs) are metal-organic molecules composed by a core of a small number of magnetic ions surrounded by an organic ligand cage. The ions are usually transition metals ($3d$), characterized by a dominant Heisenberg exchange interaction, or lanthanides ($4f$), characterized by high magnetic anisotropy originating from unquenched orbital angular momentum. Magnetic interactions within the molecular core are usually easy to describe with the spin Hamiltonian formalism, given the finite number of magnetic ions. When identical MNMs are arranged in a crystal lattice each molecule behaves as a isolated magnetic unit, since the screening due to the ligand cage suppresses inter-molecule magnetic interactions between the cores. Hence, when macroscopically probing the entire crystal one detects an amplified signal associated to a single molecule. This means that a crystal of identical MNMs probed by bulk measurements yields information at single-molecule level, providing important insights about the properties of the molecular core. This experimental opportunity have always brought much interest in the field of molecular magnetism, due to the possibility of studying fundamental quantum properties (like quantum tunnelling of the magnetization[1] or of the Neel vector) and innovative potential practical applications, such as quantum information processing[2–5] (QIP), high density information storage[6–8] and magnetocaloric refrigeration[9]. In this work I will focus on two very promising applications: one is quantum computing, and specifically the role that MNMs can play in building logical units embedding error correction[10] (see chapters 3 and 4), and the other is high density information storage using single-molecule magnets (a particular class of MNMs, see chapter 5), as nanometer-sized memories.

1.1.1 MNMs as qubits

One of the most interesting applications of MNMs is the possibility of being used as qubits in a future quantum computer. Quantum computing has attracted a growing interest in the last few decades and great results have been achieved in the most recent years[11,12], making it one of the most groundbreaking research fields in modern physics. The basic building unit of quantum computers is called *qubit* and it is a two-level quantum system, which can be prepared in both its states $|0\rangle$ and $|1\rangle$, which define the *computational basis*, as well as in any other superposition. Further details on quantum computing will be given in chapter 2.

Finding the physical object which provides the best qubit implementation for a quantum computer is one of the most challenging tasks in current research, given the stringent requirements imposed by DiVincenzo criteria[13]. Various platforms have been considered through the years: photons, cold atoms, trapped ions, nuclear and electron spins, nitrogen-vacancy pairs, and superconducting circuits[14] have all been proposed as qubits, each one with its advantages and its disadvantages. MNMs behaving as an effective spin $S = 1/2$ which splits in two levels ($m = \pm 1/2$) in presence of a magnetic field represent the ideal physical implementation of a qubit, in which the computational basis states $|0\rangle$ and $|1\rangle$ can be encoded in the two spin levels. QC operations can be implemented by manipulating the spin states of the system through electromagnetic pulses[15–19]. In some of these MNMs the effective $S = 1/2$ is obtained as the ground state emerging from transition metal ions coupled via a strong exchange interaction. As an example, MNMs whose magnetic core is composed by $[Cr_7Ni]$ heterometallic antiferromagnetic ring[5] can feature the desired two-level ground state and have been extensively studied as potential qubits[16]. Alternatively, MNMs composed by a single ion with a $S = 1/2$ spin are attractive platforms, especially the highly investigated vanadyl-based molecules, containing a single V^{4+} paramagnetic center[2,20–25]. In general, practical realization of one-qubit gates on MNM-based qubits have already been performed[20,24], as well as two-qubit entangling gates between pairs of permanently coupled qubits[15,26]. In addition, schemes for scalable two-qubit gates have already been put forward[16,27]. Moreover, they ensure good scalability in building multiple-qubit quantum hardware, which is a fundamental requirement for qubit candidates. The possibility to graft MNMs onto surfaces[6] together with their high chemical functionalization potential also led to the proposal for the realization of a spin-photon hybrid quantum hardware[3,28], which exploits the main advantages of both solid state and molecular spin quantum computing.

An important parameter to be taken in high consideration when evaluating qubit candidates is the coherence time during which it is possible to perform quantum gates without information loss. Advanced chemical engineering allowed a constant improvement of coherence times in these systems, reaching striking values of hundreds of microseconds[23,24,29]. These already remarkable results can be additionally improved by using quantum error correction codes, which encode a logical qubit in a larger Hilbert space in order to protect it from errors (of which dephasing is the most prominent one in molecular spins) achieving an even longer effective phase memory times. In this respect, MNMs proved to be a promising platform for the implementation of quantum error correction codes, something

that is still missing in state-of-the-art quantum computing but that represents a fundamental step towards the next generation of quantum hardwares.

However, in this work we won't simply treat single molecules as $S = 1/2$ qubits: thanks to great advances in coordination chemistry it is possible to synthesize molecules tailored for specific requirements, even exploiting multiple levels. In one of the works presented in this thesis we characterize a molecule whose magnetic core is composed by three weakly interacting rare-earth ions ([Er-Ce-Er]), each one behaving as an effective spin $S = 1/2$. Thus, each molecule can host three qubits and this enables us to implement within the molecule a minimal quantum error correction code which uses three physical qubits to encode a single logical qubit protected from a single phase error. Another way in which in this thesis we propose to exploit the tunability of the energy spectrum typical of MNMs is by using multiple levels (a *qudit*) in order to encode an error protected qubit into a single molecule. This goal can be achieved by using coupled electronic levels or by using nuclear energy levels in addition to the electronic ones (see chapter 4).

1.1.2 Single-molecule magnets as high-density information storage units

A particular class of MNMs called single-molecule magnets (SMMs) is characterized by the presence of magnetic hysteresis at single-molecule level. This peculiar phenomenon has been observed in a large variety of molecules since its discovery in Mn_{12}[7], which behaves as an effective giant-spin $S = 10$, experiencing a double-well potential whose energy barrier determines magnetic bi-stability. A great number of SMMs has been synthesised following the same recipe of Mn_{12}, namely with strongly coupled $3d$ ions generating an effective giant-spin ground state[30,31]. However, low anisotropy energy barrier typical of transition metal ions compounds leads to stringent temperature requirements for SMMs (usually liquid He), hindering potential applications in high-density information storage. This picture changed with the recent discovery of magnetic hysteresis up to 60 K in the dysprosocenium molecule[8], which belongs to a different class of SMMs, often referred to as single-ion magnets (SIMs). In these compounds the magnetic core of the molecule is composed by a single $4f$ ion, whose unquenched orbital angular momentum generates a high anisotropy barrier for the inversion of magnetization, causing magnetic bi-stability to appear at temperatures much higher than those previously reported. Further advances in the synthesis of SIMs led to temperatures as high as $80K$[32], effectively surpassing the important threshold of liquid nitrogen temperature, opening up room for potential applications. The driving interest behind this research field is the possibility of using SMMs in order to reach the ultimate frontier in miniaturization in high-density information storage devices. Indeed, magnetic hysteresis at the single-molecule level allows in principle to use a single SMM as physical support for a classical bit of information.

However, slow spin relaxation in SMMs is not always easy to describe and fully understand: different processes are involved in this phenomenon and their interplay is often non-trivial. The most common description[33] is obtained by combining the effects of three different relaxation mechanisms: quantum tunnelling of mag-

netization, Raman relaxation (critically relevant in rare-earth SIMs) and Orbach relaxation. The temperature dependence of their combined effect is what finally determines the blocking temperature of a given SMM, but it is often difficult to understand the role played by each one of them and how molecule structure and properties influences their behaviour (further details in Chapter 5). In one of the research works presented in this thesis we have thoroughly investigated relaxation mechanisms in Dy-based SIMs by means of various experimental and theoretical techniques, evidencing the prominent role of spin-phonon coupling. Theoretical models for these interactions have been confirmed through inelastic neutron scattering experiments, which provided the phonon density of states for the analysed systems. Results of this investigation (see chapter 5) showcase how appropriate molecule design and synthesis can provide SMMs characterized by even better performances.

1.2 Theoretical framework

In this section I will focus on introducing the main theoretical methods and models used in the research work reported in this thesis. Most of the analysis I carried out are based on spin Hamiltonian models, whose various terms will be discussed in the next pages. Many-body models are also useful in gaining deeper and more fundamental insights, hence they will be extensively discussed too. Such models allow us to precisely determine spin Hamiltonian parameters for specific systems, as well as being useful tools in interpreting experimental data when a spin Hamiltonian would have too many free parameters to get an unique fit.

1.2.1 Spin Hamiltonian

The spin Hamiltonian formalism is based on the assumption that each ion belonging to the magnetic core of the molecule can be described as an effective spin. Therefore, all magnetic contributions to the energy of the system can be expressed in terms of spin operators $\hat{\mathbf{s}}_\mathbf{i}$, each one associated to a single ion. The main contributions to the spin Hamiltonian that we considered during our analysis are: Zeeman interaction ($\hat{H_B}$), exchange interaction ($\hat{H_{ex}}$) and zero-field splitting ($\hat{H_{ZFS}}$).

$$\hat{H} = \hat{H}_B + \hat{H}_{ex} + \hat{H}_{ZFS} \tag{1.1}$$

Zeeman interaction The Zeeman Hamiltonian $\hat{H}_B$ describes the interaction of each spin with an external magnetic field $\mathbf{B}$.

$$\hat{H}_B = \mu_B \sum_i \mathbf{B} \cdot \underline{\mathbf{g}}_i \cdot \hat{\mathbf{s}}_i \tag{1.2}$$

Where μ_B is the Bohr magneton and $\underline{\mathbf{g_i}}$ is the spectroscopic g-tensor of the i-th ion. This term has the effect of breaking the $(2s_i+1)$-fold degeneracy of a spin s_i multiplet and it will prove fundamental in all of the proposed applications of MNMs in the next chapters.

Exchange interaction This term represents two-body magnetic interactions: the intensity, type and range of exchange interactions within a MNM are responsible for a great number of interesting behaviours. A notable example is the giant-spin ground state in $3d$ ions based SMMs, which arises from strong isotropic magnetic exchange coupling. Exchange interaction Hamiltonian couples electron spins, and it can be written in its most general form as

$$\hat{H}_{ex} = \sum_{i>j} \hat{\mathbf{s}}_i \cdot \underline{\mathbf{J}}_{ij} \cdot \hat{\mathbf{s}}_j \tag{1.3}$$

where $\underline{\mathbf{J}}_{ij}$ is the exchange coupling tensor. Usually in MNMs the two ions are too far apart for the short-range *direct* exchange interaction to be relevant, and hence they are magnetically coupled through *super-exchange* mediated by orbitals belonging to interposed ions. In systems like $3d$ ions-based MNMs the exchange Hamiltonian is usually dominated by its isotropic term, the well-known Heisenberg Hamiltonian:

$$\hat{H}_{iso} = \sum_{i>j} J_{ij} \hat{\mathbf{s}}_i \cdot \hat{\mathbf{s}}_j \tag{1.4}$$

Even though the ever-present dipole-dipole interaction has a completely different physical origin than exchange interaction (both direct and super-exchange), it is possible to write it in the same form as $\hat{H}_{ex}$, since the two interactions share the same dependence on spin operators $\mathbf{s}_i$. Dipolar interaction contribution to magnetic interaction is expressed by the dipolar coupling tensor $\underline{\mathbf{J}}_{ij}^{dip}$, which within the point-dipole approximation only depends on the distance between the ions (R_{ij}) and their g-tensors:

$$\left(J_{ij}^{\alpha\beta}\right)^{dip} = \frac{\mu_B^2}{R_{ij}^3}\left[\sum_{\delta} g_1^{\alpha\delta} g_2^{\delta\beta} - 3\frac{\sum_\delta g_1^{\alpha\delta} R_\delta \sum_\gamma R_\gamma g_2^{\gamma\beta}}{R_{ij}^2}\right] \tag{1.5}$$

where $\alpha, \beta, \gamma, \delta = x, y, z$. Note that this term generally leads to an anisotropic dipolar coupling tensor, which together with the exchange coupling tensor determines the overall interaction tensor.

Zero-field splitting The one-body zero-field splitting (ZFS) term of the spin Hamiltonian accounts for the interaction of a single ion with its surrounding charges. ZFS strongly depends on the symmetry and intensity of the field originating from neighbouring ions and can cause a strongly anisotropic effect. The ZFS Hamiltonian can be written as:

$$\hat{H}_{ZFS} = \sum_i \hat{\mathbf{s}}_i \cdot \underline{\mathbf{D}}_i \cdot \hat{\mathbf{s}}_i \tag{1.6}$$

where $\underline{\mathbf{D}}_i$ is the symmetric ZFS tensor on the i-th ion. By choosing the reference frame as the one defined by the principal axes of $\underline{\mathbf{D}}_i$ we can rewrite the i-th term of Equation 1.6 as

$$\hat{H}_{ZFS,i} = D_i\left[\hat{s}_{i,z}^2 - s_i(s_i+1)/3\right] + E_i\left(\hat{s}_{i,x}^2 - \hat{s}_{i,y}^2\right) \tag{1.7}$$

where $D_i = D_{i,zz} - (Di, xx - D_{i,yy})/2$ and $E_i = (D_{i,xx} - D_{i,yy})/2$, given that the i-th ZFS tensor is diagonal in this reference frame.

Nuclear spin Hamiltonian If some of the magnetic ions within the molecule also have a magnetic nucleus, it is necessary to add to the spin Hamiltonian nuclear spin-dependent terms. These account for the magnetic interaction of the nuclear spin on the i-th site $\mathbf{I}_i$ with and external magnetic field (Zeeman interaction) as well as with the corresponding electron spin $\mathbf{s}_i$ (hyperfine interaction). Additionally, quadrupole interaction represents the electrostatic interaction of each nucleus with local fields, hence its corresponding Hamiltonian term shares the same structure with the electronic ZFS Hamiltonian 1.6.

$$\hat{H}_{nuc} = \mu_N \sum_i g_{I,i} \mathbf{B} \cdot \hat{\mathbf{I}}_i + \sum_i \hat{\mathbf{I}}_i \cdot \underline{\mathbf{A}}_i \cdot \hat{\mathbf{s}}_i + \sum_i \hat{\mathbf{I}}_i \cdot \underline{\mathbf{U}}_i \cdot \hat{\mathbf{I}}_i \tag{1.8}$$

where μ_N is the nuclear magneton, $g_{I,i}$ is the nuclear g-factor and A_i defines the hyperfine coupling between nuclear and electronic spin. Zeeman effect acts in the same way as in the electron spin Hamiltonian, except that μ_N is more than 10^3 times smaller than μ_B, causing a much slighter splitting of the $(2I+1)$-fold degeneracy of the nuclear spin I. Hyperfine is the leading interaction, translating in an effective Zeeman splitting of the nuclear levels induced by the electronic spin. Quadrupole terms are much smaller, but can be important to distinguish nuclear excitations.

1.2.2 Many-body models

The spin Hamiltonian formalism gives a thorough representation of the magnetic interactions within the core of a MNM, but its determination often requires strong assumptions on its form and hierarchy of interactions. Moreover, the determination of Hamiltonian parameters can be inaccurate when computed *ab-initio* with density-functional theory (DFT) simulations. In the work presented in chapter 6 we employed a combination of DFT simulations and many-body models to determine the spin Hamiltonian of a Ni dimer without any assumption on its form. This result was achieved by using DFT simulations to find a basis to write a generalized Hubbard model and to determine its parameters. This model accounts for strong electron-electron correlation effects, often not properly included in *ab-initio* calculations. From this many-body model it is then possible to determine spin Hamiltonian parameters and the hierarchy of the magnetic interactions by limiting ourselves to the low-energy subspace.

We use the generalized form of the Hubbard model:

$$\begin{aligned}\hat{H} = &\sum_{i,m,\sigma} \mathcal{E}_{im}\hat{n}_{im\sigma} + \sum_{i,m} U_i \hat{n}_{im\uparrow}\hat{n}_{im\downarrow} \\ &+ \frac{1}{2}\sum_{i,\sigma,\sigma'}\sum_{m\neq m'} (U_i - 2J_{H,i} - J_{H,i}\delta_{\sigma,\sigma'})\hat{n}_{im\sigma}\hat{n}_{im'\sigma'} \\ &- \sum_{i,m\neq m'} J_{H,i}\left[\hat{c}^{\dagger}_{im\uparrow}\hat{c}^{\dagger}_{im\downarrow}\hat{c}_{im'\uparrow}\hat{c}_{im'\downarrow} + \hat{c}^{\dagger}_{im\uparrow}\hat{c}_{im\downarrow}\hat{c}^{\dagger}_{im'\downarrow}\hat{c}_{im'\uparrow}\right] \\ &+ \sum_{i,i'}\sum_{m,m',\sigma} t^{i,i'}_{m,m'}\hat{c}^{\dagger}_{im\sigma}\hat{c}_{i'm'\sigma} - \hat{H}_{DC} + \hat{H}_{SO}\end{aligned} \tag{1.9}$$

where i runs over each ion site, m runs over the orbitals on each site and $\sigma = \uparrow, \downarrow$ is the electron spin. In this notation $\hat{c}^{\dagger}_{im\sigma}$ ($\hat{c}_{im\sigma}$) creates (annihilates) an electron with spin σ in the m-th orbital on the i-th site and we also used the number operator defined as $\hat{n}_{im\sigma} = \hat{c}^{\dagger}_{im\sigma}\hat{c}_{im\sigma}$. The first term accounts for orbital energy, with each electron contributing by a quantity $\mathcal{E}_{im}$ which is the energy associated to the m-th orbital on the i-th site. The second term includes Coulomb repulsion on the same orbital, occurring when it is occupied by both a spin $\uparrow$ and a spin $\downarrow$ electron and associated to the value U_i. The third term represents Coulomb repulsion between electrons occupying different orbitals on the same site and its intensity (written as a function on U_i and $J_{H,i}$) also depends on if the two electron spins are parallel or antiparallel. The fourth term includes both pair hopping (a couple of electrons with antiparallel spin on the same orbital moving to a different orbital on the same site) and spin-flip (two electrons with antiparallel spin on different orbitals on the same site both change their spin state), their intensities both determined by $J_{H,i}$. The fifth term is the hopping term, associated to an electron moving between different sites, with the energy of each "jump" determined by the hopping integrals $t^{i,i'}_{m,m'}$. $\hat{H}_{DC}$ is the double counting correction, subtracting the long-range correlations of the Hubbard model already accounted for at a mean-field level in the LDA simulations. For systems with homonuclear magnetic ions this term only introduces an overall energy shift, identical for each orbital and each site. The last term is the spin-orbit coupling

$$\hat{H}_{SO} = \sum_i \lambda_i \sum_m \hat{\mathbf{l}}_{im}\cdot\hat{\mathbf{s}}_{im} = \sum_i \lambda_i \sum_m \left[\hat{l}^z_{im}\hat{s}^z_{im} + \frac{1}{2}(\hat{l}^-_{im}\hat{s}^+_{im} + \hat{l}^-_{im}\hat{s}^+_{im})\right] \tag{1.10}$$

where $\hat{l}_{im}$ and $\hat{s}_{im}$ are the angular momentum operator and the electron spin operator, respectively, on the m-th orbital on the i-th site. Spin-orbit coupling 1.10 can be written by using creation and annihilation operators $\hat{c}^{\dagger}_{im\sigma}$ ($\hat{c}_{im\sigma}$) as

$$\begin{aligned}\hat{H}_{SO} = \sum_i \frac{\lambda_i}{2}\sum_{m,m'}\Big[&\mathcal{L}^z_{i,mm'}(\hat{c}^{\dagger}_{im\uparrow}\hat{c}_{im'\uparrow} - \hat{c}^{\dagger}_{im\downarrow}\hat{c}_{im'\downarrow}) + \\ &+ \mathcal{L}^+_{i,mm'}\hat{c}^{\dagger}_{im\downarrow}\hat{c}_{im'\uparrow} + \mathcal{L}^-_{i,mm'}\hat{c}^{\dagger}_{im\uparrow}\hat{c}_{im'\downarrow}\Big]\end{aligned} \tag{1.11}$$

in which the spin of the $\hat{c}^{\dagger}_{im\sigma}$ ($\hat{c}_{im\sigma}$) operators is chosen respecting the action of the operators $\hat{s}^z$, $\hat{s}^+$, $\hat{s}^-$ (raising or lowering the electron spin) and $\mathcal{L}^z_{i,mm'}$, $\mathcal{L}^+_{i,mm'}$, $\mathcal{L}^-_{i,mm'}$ are the matrix elements of the total angular momentum operators $\hat{l}^z$, $\hat{l}^+$, $\hat{l}^-$ written in the CF basis.

1.2.3 Construction of many-body models from DFT *ab-initio* calculations

In this section we will focus on describing how we exploited DFT self-consistent calculations combined with many-body models to get a full description of the interactions within MNMs. In this compounds the partially filled d and f shells exhibit strong electron correlation, which are not included in most DFT calculations (LDA) or are treated at mean-field level (LDA+U)[34,35]. These two assumptions do not allow a precise determination of Hamiltonian parameters in most MNMs. What we did instead was computing from *ab-initio* calculations the parameters of a system-specific Hubbard model, which directly accounts for correlations and can be used to obtain an in-depth knowledge of the system's properties, including spin Hamiltonian parameters[36,37].

The first step in this process consists in performing DFT self-consistent runs in local density approximation (LDA) (See appendix), using the NWChem quantum chemistry code[38]. In this step, which only needs the molecular structure and the atomic basis choice as a starting point, we obtain the Kohn-Sham orbitals of the molecule, their respective energy and their occupancy. The molecular structure must include nuclear coordinates, atomic numbers and number of electrons, whereas the atomic basis choice is written in direct space as a linear combination of gaussians, approximating the atomic orbitals. From this result we focus our attention on the more correlated states, which in transition metal MNMs are d-states with energy close to the Fermi level, occupied by the electrons responsible for magnetism in the molecule. On the subspace generated by these states we apply the Foster-Boys localization, which minimizes their spatial extent, returning a set of orbitals (Foster-Boys orbitals) localized around the metal ions, and written in the one-electron basis $\{|\beta_{im}\rangle\}$ (using the same notation as before, where m runs over the orbitals on the i-th site). From these orbitals we can calculate the hopping integrals $t^{i,i'}_{m,m'} = \langle\beta_{im}|\hat{h}|\beta_{i'm'}\rangle$, where $\hat{h}$ is the one-body Hamiltonian obtain with the initial LDA calculations. By diagonalizing the on-site hopping matrices $t^{i,i}_{m,m'}$ it is possible to identify its eigenstates as the crystal field (CF) one-electron basis $\{|\xi_{im}\rangle\}$ and its eigenvalues ε_{im} are CF energy levels, whose splitting reflects the symmetry of the ligand field on the i-th site. At this point it is convenient to use this new CF basis as the basis on which to write the generalized Hubbard model in Eq. 1.9.

In order to build a system-specific model as in Equation 1.9, in which we have already calculated the hopping integrals $t^{i,i'}_{m,m'}$ and the orbital energy ε_{im}, we now need to determine for each site i the average screened direct Coulomb integral U_i and the average screened exchange integral $J_{H,i}$. These are obtained by performing DFT calculations in constrained local density approximation (cLDA) on the CF orbitals, in which the occupancy of each orbital is kept constant throughout the

simulations. After various iterations of this calculations with different fixed occupancies, it is possible to determine U_i and $J_{H,i}$ for each site by writing the energy differences (obtained from cLDA calculations) between different configurations as a function of these two parameters.

The spin-orbit coupling λ_i can be computed by performing *ab-initio* simulations including spin-orbit interaction, and then by comparing the results of these relativistic calculations with those obtained before. This process is highly time-consuming and in the work presented in this thesis we opted to use tabulated values of λ_i for single ions[39], which give a very good approximation, as demonstrated in [36].

Advantages of many-body DFT When determining spin Hamiltonian parameters from standard *ab-initio* calculations (LDA or LDA+U), an initial guess on the form of the Hamiltonian is needed in order to correctly address all contributions. Moreover, if one opted to include all possible interactions and corrections, results would not be good enough to justify the method, which quickly becomes greatly unpractical and time consuming. By exploiting the determination of a system-specific many-body model as an intermediate step we are not making any assumption on the magnetic interactions involved. From the many-body model by a canonical transformation it is then possible to limit ourselves to the low-energy subspace, in which we can determine spin Hamiltonian parameters in the most general way. The crucial advantage of this approach is the direct inclusion of strong electron-electron correlations in the Hubbard model, given how relevant these effects can be in the open d or f shells responsible for magnetism in MNMs. A determination of the spin Hamiltonian from DFT calculations may not correctly include such effects, with dramatic consequences on the correct description of magnetic interactions within the molecule.

The many-body DFT approach has already proven itself to be a valuable tool in determining spin Hamiltonian parameters with great accuracy in compounds whose magnetic properties are associated to transition metal ions[36,37,40]. The extension of this method to MNMs with rare-earth ions will be a topic of great interest in the near future as well as other implementations of the Hubbard model determined from *ab-initio* calculations, as discussed in chapter 6.

1.3 Experimental techniques

Theoretical methods only offer one side of the picture for MNMs: experimental characterization is complementary and fundamental in understanding the properties of these compounds. Moreover, tailored experiments allow the development of better theoretical tools by confirming or confuting theorized results, providing an ever-growing depth of understanding in the field of MNMs. In the research works presented in this thesis various experimental results have been of crucial importance, of which I carried out the data fitting procedure, based on the theoretical models described before. An experimental technique with which I had an hands-on experience is inelastic neutron scattering (INS), with two experiments performed at the MERLIN spectrometer at the ISIS neutron and muon source. The impor-

tance of neutron scattering in my PhD is also consolidated by my attendance to two extensive summer schools on the technique and its applications, especially in the field of magnetism. In the following, the first few sections will describe the experimental techniques used to characterize MNMs along with the most important formulas used for data interpretation. The next section will more extensively treat neutron scattering, with greater focus on INS and the theory behind the technique.

1.3.1 Magnetometry

One of the most important experimental techniques involved in the characterization of MNMs is SQUID (superconducting quantum interference device) magnetometry. A SQUID magnetometer works by moving the sample in a superconducting loop containing Josephson junctions, generating a superconducting current in the loop, directly linked to the magnetic moment of the sample. By measuring the variation of flux induced by the sample it is possible to detect extremely small magnetic moments with great precision. With this technique the physical quantities that can be extracted are magnetization and magnetic susceptibility, both as a function of temperature (T) and applied magnetic field ($\mathbf{B}$).

Starting from the spin Hamiltonian of the system, magnetization can be computed as

$$\mathbf{M}(T) = \frac{\mu_B}{Z} \sum_n \langle \psi_n | \mu | \psi_n \rangle \, e^{-\beta E_n}, \boldsymbol{\mu} = -\sum_i \underline{\mathbf{g}}_i \cdot \mathbf{s}_i \tag{1.12}$$

where μ_B is the Bohr magneton, $|\psi_n\rangle$ are the eigenstates of the system, E_n are their corresponding eigenvalues, $Z = \sum_n g_n e^{-\beta E_n}$ is the partition function, g_n is the degeneracy of the eigenvalue E_n and $\boldsymbol{\mu}$ is the magnetic moment of the molecule. Magnetic susceptibility can be derived from magnetization as the low magnetic field ($\mathbf{B}$) limit of the ratio M/B. The most general formula for the susceptibility tensor can be written as

$$\chi_{\alpha\beta} = \mu_B \frac{\partial \langle \mu_\alpha \rangle}{\partial B_\beta} \tag{1.13}$$

where $\alpha, \beta = x, y, z$ and $\langle ... \rangle$ represents thermal averaging.

1.3.2 Calorimetry

Specific heat measurements give important insight on the energy level structure of the spin Hamiltonian describing the magnetic core of a MNM. Specific heat can be derived as a function of the magnetic field $\mathbf{B}$ and of the temperature T as the thermodynamic derivative of the internal energy $\langle E \rangle$:

$$C_v = \frac{\partial \langle E \rangle}{\partial T} = -\frac{1}{K_B T^2} \frac{\partial \langle E \rangle}{\partial \beta} \tag{1.14}$$

where $\beta = 1/K_B T$, K_B is the Boltzmann constant and $\langle E \rangle = \frac{1}{Z} \sum_n g_n E_n e^{-\beta E_n}$. From this formula it is trivial to deduce an expression for the specific heat for unit mole as a function of the energy levels of the system:

$$\frac{C_v}{R} = \frac{N\beta^2}{Z^2} \sum_{m>n} g_n g_m (E_n - E_m)^2 e^{-\beta(E_n+E_m)} \tag{1.15}$$

where N is the number of magnetic ions in the molecule.

Significant information can be gained on the energy levels by plotting C_v as a function of T: increasing the temperature causes an increment in the population of the excited states, more precisely at temperatures comparable to the energy gap $\Delta_{ij} = E_j - E_i$ a great number of transitions takes place between the states i and j. This is directly associated to a steep increase in the internal energy of the system, therefore showing a peak (Schottky peak) in the specific heat at temperatures centred around $\Delta_{ij}/2$. The same peaks can be detected as a function of magnetic field, in which case the population change is due to the shift of the energy levels with varying B. Therefore, studying the position of Schottky peaks as a function of both B and T is useful in determining the energy level structure of the Hamiltonian (even detecting energy crossings and/or anti-crossings) and how it interacts the external field.

This type of analysis can be hindered by the presence of a phonon contribution to specific heat, which quickly grows with T and can dominate the signal associated to the magnetic properties of the sample, especially at higher temperatures. However, this contribution can be easily modelled[41] as

$$\frac{C_v^{ph}}{R} = \frac{r234T^3}{(\Theta + \delta T^2)^3} \tag{1.16}$$

where r is the number of atoms per molecule and $(\Theta + \delta T^2)$ is the Debye temperature. Including this effect in simulations can help correctly address magnetic contributions even at temperatures at which the vibrational contribution has a non-negligible effect.

1.3.3 Continuous-wave EPR

Continuous-wave electron paramagnetic resonance (cw-EPR) is a spectroscopic technique useful to study magnetic properties of atoms or molecules with unpaired electrons. A static magnetic field $\mathbf{B}$ is applied on the sample, which is then probed by an oscillating magnetic field of frequency ω, perpendicular to $\mathbf{B}$ and significantly smaller. The response of the sample induced by this oscillating field is associated to intra-multiplet transitions excited by the applied frequency ω. Then, by varying the static field while keeping ω fixed, one can probe how the excited transitions change with the applied field, gaining important insights on the magnetic ions of the sample. A great advantage of this technique comes from the negligible probability of transitions between different multiplets to take place within an EPR experiment, reducing the eventual noise that other techniques are susceptible to. Data collected by the means of cw-EPR experiments are fitted with the following formula for the imaginary part of susceptibility:

$$\chi''_{AA}(\theta, \phi) = \pi \sum_{i,i'} I_{i,i'}(\theta, \phi)(n_i - n_{i'})\delta(\hbar\omega - \Delta E_{i,i'}) \tag{1.17}$$

where (θ, ϕ) are polar coordinates for the orientation of the static field with respect to the reference frame in which the magnetic ions are described and n_i is the statistical population of the i-th state, defined as $n_i = e^{-\beta E_i}/Z$. The term $\delta(\hbar\omega - \Delta E_{i,i'})$ selects the transitions with energy equal to $\hbar\omega$ and it is to be replaced with the instrument resolution when fitting a real experiment, usually with a Gaussian or a Lorentzian line-shape. The transition intensity $I_{i,i'}(\theta, \phi)$ between the states i and i' is defined as

$$\begin{aligned} I_{i,i'}(\theta,\phi) = (1-\sin^2\theta\cos^2\phi)S^*_{x,ii'}S_{x,ii'} - \sin^2\theta\sin\phi\cos\phi(S^*_{x,ii'}S_{y,ii'} + S^*_{y,ii'}S_{x,ii'}) + \\ - \cos\theta\sin\theta\cos\phi(S^*_{x,ii'}S_{z,ii'} + S^*_{z,ii'}S_{x,ii'}) + (1-\sin^2\theta\sin^2\phi)S^*_{y,ii'}S_{y,ii'} + \\ - \cos\theta\sin\theta\sin\phi(S^*_{y,ii'}S_{z,ii'} + S^*_{z,ii'}S_{y,ii'}) + \sin^2\theta S^*_{z,ii'}S_{z,ii'} \end{aligned} \tag{1.18}$$

where $S_{k,ii'} = \langle i|\hat{S}_k|i'\rangle$ and $\hat{S}_k = \sum_j g_{j,k}\hat{S}_{j,k}$ is the total spin operator of the molecule along the direction $k = x, y, z$, in which the contribution of each ion j of the molecule is weighted by its g-factor. Since all cw-EPR experiments analysed in this work are performed on powder samples, we computed the spherical average of $\chi''_{AA}(\theta, \phi)$:

$$\chi''_{AA} = \frac{\sum_{\theta,\phi}\chi''_{AA}(\theta,\phi)\sin\theta}{\sum_{\theta,\phi}\sin\theta} \tag{1.19}$$

Therefore, the fitting procedure for a cw-EPR experiment involves the diagonalization of the spin Hamiltonian for each magnetic field $\mathbf{B}$, then we use the eigenstates and the eigenvalues to compute χ''_{AA}, averaging for all the different orientations (θ, ϕ). What is usually compared with experimental results is the derivative $d\chi''_{AA}/dB$, much more sensitive to small variations in signal. Please note that in order to obtain an exact fit of a cw-EPR spectrum we would also need to determine the rescaling factor. This quantity is related to several experimental parameters (such as cavity quality factor and sample mass) which often are not precisely known. Hence, simulations are reported in arbitrary units.

Performing a cw-EPR experiment on a MNM yields detailed insights on the structure of the energy levels of the spin Hamiltonian and how they interact with an external magnetic field. This is especially useful for determining g-tensors for ions with a well-isolated doublet ground state as well as other Hamiltonian parameters (exchange, ZFS, hyperfine interaction) when combined with other techniques like the ones described in the previous sections.

1.4 Inelastic neutron scattering

1.4.1 Neutron scattering

Scattering experiments cover a crucial role in modern physics since they enable the precise determination of structure, dynamics and properties of matter at the atomic level. This thorough description can be obtained by studying the deflection and change in energy of a coherent radiation beam incident on a sample, provided

that the interaction of the beam with the sample is known and well-described. In neutron scattering experiments the probe of choice is a neutron beam, bringing along many advantages: thermal neutrons have an energy of $\approx 12-100$ meV, close to the energy typical of interactions at the atomic level, and a wavelength of a few Å, similar to interatomic distances in solids. Another important property of neutrons when compared to other scattering probes (*e.g.* electrons) is the absence of an electric charge: neutrons do not strongly interact with electron clouds as they do with nuclei and are therefore highly penetrating and non-destructive with respect to the sample. Moreover, neutrons have a non-zero spin $s = 1/2$ and interact with spin and orbital momenta associated to unpaired electrons by the dipole-dipole interaction, making neutrons a great probe for investigating magnetic properties of materials. From these properties it is clear that neutron scattering is an optimal technique for studying MNMs: the interaction with nuclei allows one to probe molecular vibrations and the magnetic interaction allows for a precise determination of the spin Hamiltonian of the magnetic core and the coherent spin dynamics of these systems.

1.4.2 Neutron-scattering experiment

As for most scattering experiments each neutron of a monochromatic beam with incident energy E_i and wave vector $\boldsymbol{k_i}$ that experiences scattering from the sample is collected by a detector at position (θ, ϕ), which determines its final wave-vector $\boldsymbol{k_f}$ and energy E_f (in time-of-flight spectrometers determined by the detection time). These quantities define the exchange in energy $\hbar\omega$ and momentum $\boldsymbol{Q}$ between the sample and the neutron:

$$\begin{cases} \hbar\omega = E_f - E_i \\ \mathbf{Q} = \mathbf{k}_f - \mathbf{k}_i \end{cases} \tag{1.20}$$

An *elastic neutron scattering* experiment assumes that there is no energy exchange between sample and neutron ($\hbar\omega = 0$), whereas in the more general case $\hbar\omega \neq 0$ the experiment is called *inelastic neutron scattering*.

The measured quantity in a neutron scattering experiment is the neutron count rate at the detector I_{meas}, defined as the number of neutrons which emerge, per unit time, in a small solid angle $\Delta\Omega$ centred around the (θ, ϕ) direction with final energy between E_f and $E_f + \Delta E_f$ (ΔE_f is the uncertainty in determining the final energy).

$$I_{meas} = \eta(E_f) J_{in}(E_i) \left(\frac{d^2\sigma}{d\Omega dE_f} \right) \Delta\Omega\Delta E_f \tag{1.21}$$

where $J_{in}(E_i)$ is the incident neutron current, $\eta(E_f)$ is the efficiency of the detector and $d^2\sigma/d\Omega dE_f$ is the *double differential cross-section*. By realistically assuming that all the other terms of equation 1.21 are known, the relevant quantity to define is the double differential cross-section, as it contains all physical information about the sample.

1.4.3 Double differential cross-section

Given the neutron being a weak probe with regard to the sample, its interaction can be treated as a perturbation of the system, therefore an expression for the double differential cross-section can be obtained by employing Fermi's Golden Rule (FGR). In this approximation neutrons are treated as plane waves both before and after the scattering event and the neutron-sample system changes its state from $|\mathbf{k}_i, \nu_i\rangle$ to $|\mathbf{k}_f, \nu_f\rangle$, with $\vec{k}_f$ determined by $d\Omega$. The double differential cross-section associated to the transition $\nu_i \to \nu_f$ can be written as a function of the transition rate given by the FGR as:

$$\left(\frac{d^2\sigma}{d\Omega dE_f}\right)_{\nu_i \to \nu_f} = \left(\frac{m_n}{2\pi\hbar^2}\right)\frac{k_f}{k_i}|\left\langle \mathbf{k}_f, \nu_f|V|\mathbf{k}_i, \nu_i\right\rangle|^2 \delta(E_{\nu_i} - E_{\nu_f} + \hbar\omega) \tag{1.22}$$

where V is the interaction potential between the neutron and the sample. In an inelastic neutron scattering experiment there is no control over the initial and final state of the system: to finally obtain the doule-differential cross section that appears in equation 1.21 we need to sum over all the possible final states of the sample ν_f and to average over all its possible initial states ν_i employing Boltzmann statistics. Moreover, the interaction potential $V(\mathbf{r}, t)$ can be expressed through its Fourier transform $V(\mathbf{Q}, t)$, finally obtaining the formula:

$$\left(\frac{d^2\sigma}{d\Omega dE_f}\right) = \left(\frac{m_n}{2\pi\hbar^2}\right)\frac{k_f}{k_i}\int \langle V^\dagger(\mathbf{Q}, 0)V(\mathbf{Q}, t)\rangle\, e^{-i\omega t}dt \tag{1.23}$$

where $\langle\rangle$ denotes the thermal expectation value. From this expression we can further define the *scattering function* $S(\mathbf{Q}, \omega)$, in which all information about the physics of the sample is stored:

$$S(\mathbf{Q}, \omega) = \frac{1}{2\pi\hbar}\int \langle V^\dagger(\mathbf{Q}, 0)V(\mathbf{Q}, t)\rangle\, e^{-i\omega t}dt \tag{1.24}$$

The determination of this quantity is the ultimate goal of an inelastic neutron scattering experiment. The physical origin of the interaction potential V determines whether the nature of the scattering process is nuclear, magnetic or both, as it often is in the case of MNMs. Hence, the scattering function can be further decomposed into its nuclear and magnetic contributions as:

$$S(\mathbf{Q}, \omega) = S_{nuc}(\mathbf{Q}, \omega) + S_{mag}(\mathbf{Q}, \omega) \tag{1.25}$$

which can be both determined, as shown in the next two sections.

1.4.4 Nuclear contribution to double differential cross-section

The interaction potential relevant for the determination of the nuclear contribution to the double differential cross-section is called *Fermi's pseudopotential* and is expressed as:

$$V_{nuc}(r) = \sum_{j=1}^{N}\frac{2\pi\hbar^2}{m_n}b_j\delta(\boldsymbol{r} - \mathbf{R}_j(t)) \tag{1.26}$$

where the neutron at position $\mathbf{r}$ interacts with the j-th nucleus (at position $\mathbf{R}_j(t)$) with intensity related to the *scattering length* b_j, which can be a complex number (its imaginary part associated to neutron absorption). Given the short range nature of nuclear forces (10^{-15} m) when compared to thermal neutron wavelength (10^{-10} m), the nuclei are seen as point-like particles from the viewpoint of the neutrons, hence the Dirac delta. Calculating the double differential cross-section with this potential gives:

$$\left(\frac{d^2\sigma}{d\Omega dE_f}\right) = \frac{k_f}{k_i}\frac{1}{2\pi\hbar}\sum_{j,k}\langle b_k b_j\rangle \int \langle e^{-i\boldsymbol{Q}\cdot\mathbf{R}_k(0)} e^{i\boldsymbol{Q}\cdot\mathbf{R}_j(t)}\rangle\, e^{-i\omega t} dt \tag{1.27}$$

where $\langle b_k b_j\rangle = \langle b_j^2\rangle = \overline{b^2}$ if $k = j$ and $\langle b_k b_j\rangle = \langle b_k\rangle \langle b_j\rangle = \bar{b}^2$ otherwise. By adding and subtracting the terms with $k = j$ multiplied by $\bar{b}^2$ and defining *coherent* and *incoherent* cross sections as

$$\begin{cases} \sigma_{coh} = 4\pi\bar{b}^2 \\ \sigma_{inc} = 4\pi(\overline{b^2} - \bar{b}^2) \end{cases} \tag{1.28}$$

we can write the double differential cross-section as the sum of two terms:

$$\left(\frac{d^2\sigma}{d\Omega dE_f}\right) = \frac{\sigma_{coh}}{4\pi}\frac{k_f}{k_i} S(\boldsymbol{Q},\omega) + \frac{\sigma_{inc}}{4\pi}\frac{k_f}{k_i} S_{self}(\boldsymbol{Q},\omega) \tag{1.29}$$

where $S(\boldsymbol{Q},\omega) = S_{dist}(\boldsymbol{Q},\omega) + S_{self}(\boldsymbol{Q},\omega)$, in which $S_{self}(\boldsymbol{Q},\omega)$ contains all the terms with $j = k$ and $S_{dist}(\boldsymbol{Q},\omega)$ all the other terms. Incoherent scattering accounts for correlations between the position of the same nucleus at different times, whereas coherent scattering also includes correlations between the positions of different nuclei at different times, therefore accounting for interference effects. This distinction arises from the random distribution of the scattering lengths around their mean value. In fact, scattering lengths b_j also depend on the total spin of the nucleus-neutron system in a scattering event: both neutron spin and the isotope of the nucleus influence the value of b_j.

1.4.5 Inelastic neutron scattering probing phonon density of states

The time-dependency of the k-th nucleus positions $\mathbf{R}_j(t)$ can be expressed as motion around an equilibrium position $\mathbf{l}_j$ as $\mathbf{R}_j(t) = \mathbf{l}_j + \mathbf{u}_j(t)$. Substituting this expression in $S(\mathbf{Q},\omega)$ and defining $U = -i\mathbf{Q}\cdot\mathbf{u}_k(0)$ and $V = i\mathbf{Q}\cdot\mathbf{u}_j(t)$ we obtain this formula:

$$S(\mathbf{Q},\omega) = \frac{1}{2\pi\hbar}\sum_{j,k} e^{i\mathbf{Q}\cdot(\mathbf{l}_j - \mathbf{l}_k)} \int \langle e^U e^V\rangle\, e^{-i\omega t} dt \tag{1.30}$$

In the harmonic approximation the displacement induced by $\mathbf{u}_j(t)$ can be expressed in terms of phonon creation and annihilation operators $\hat{a}^\dagger(\mathbf{q})$ and $\hat{a}(\mathbf{q})$ ($\hat{n}(\mathbf{q}) = \hat{a}^\dagger(\mathbf{q})\hat{a}(\mathbf{q})$), thus $\hat{U}$ and $\hat{V}$ are Hermitian operators. Therefore, after some

considerations on the distribution of displacements within the harmonic approximation[42–44] we can write:

$$\langle e^{\hat{U}} e^{\hat{V}} \rangle = e^{\langle \hat{U}^2 \rangle} e^{\langle \hat{U}\hat{V} \rangle} \tag{1.31}$$

where $e^{\langle \hat{U}^2 \rangle} = e^{-2W(\mathbf{Q})}$ is called the Debye-Waller factor. Now we can expand $e^{\langle \hat{U}\hat{V} \rangle}$ into a Taylor series, based on the fact that displacements are small compared to lattice parameters, obtaining:

$$e^{\langle \hat{U}\hat{V} \rangle} \approx 1 + \langle \hat{U}\hat{V} \rangle + \frac{1}{2} \langle \hat{U}\hat{V} \rangle^2 + \cdots + \frac{1}{n!} \langle \hat{U}\hat{V} \rangle^n + \ldots \tag{1.32}$$

where the first term (0-th order, therefore $\langle \mathbf{u}_j(t) \rangle = 0$) gives the elastic scattering function, the second term gives the scattering function for all one-phonon processes, and so on the n-th order term gives the scattering function for all n-phonon processes. If we consider only the one-phonon term, we can calculate the matrix element of $\hat{U}\hat{V}$, where only terms involving the products $\hat{a}^\dagger(\mathbf{q})\hat{a}(\mathbf{q})$ and $\hat{a}(\mathbf{q})\hat{a}^\dagger(\mathbf{q})$ yield a non-zero contribution, raising or lowering by $\hbar\omega$ the energy of the harmonic oscillator. Now we can write the scattering function for phonon emission (-1) and absorption ($+1$) as:

$$S(\mathbf{Q},\omega)_{\pm 1} = \frac{(2\pi)^3}{2Mv_0} e^{-2W(\mathbf{Q})} \sum_{s,\mathbf{q},\mathbf{G}} \frac{(\mathbf{Q}\cdot\boldsymbol{\varepsilon}_s(\mathbf{q}))^2}{\omega_s(\mathbf{q})} \langle \hat{n}_s(\mathbf{q}) + \frac{1}{2} \pm \frac{1}{2} \rangle \, \delta(\omega \mp \omega_s(\mathbf{q})) \delta(\mathbf{Q} \mp \mathbf{q} - \mathbf{G}) \tag{1.33}$$

where $\mathbf{q}$ is the wave-vector of a normal mode, s its polarization index, $\omega(\mathbf{q})$ its eigenvalue, $\varepsilon(\mathbf{q})$ its eigenvector, M the atomic mass, v_0 the volume of the unit cell of the crystal and $\mathbf{G}$ a vector in the reciprocal lattice. The two Dirac-δ factors in this formula ensure that the energy and momentum transferred from (to) the neutron to (from) the sample are equal to those of the created (annihilated) phonon. This strict selection on both energy and momentum allows to measure *phonon dispersion relations* by studying how the energy of each mode $\omega_s(\mathbf{q})$ varies with $\mathbf{q}$.

If we now consider an incoherent scattering experiment, where $\mathbf{l}_j = \mathbf{l}_k$, we obtain:

$$S(\mathbf{Q},\omega)_{self,\pm 1} = \frac{1}{2M} e^{-2W(\mathbf{Q})} \sum_{s,\mathbf{q}} \frac{(\mathbf{Q}\cdot\boldsymbol{\varepsilon}_s(\mathbf{q}))^2}{\omega_s(\mathbf{q})} \langle \hat{n}_s(\mathbf{q}) + \frac{1}{2} \pm \frac{1}{2} \rangle \, \delta(\omega \mp \omega_s(\mathbf{q})) \tag{1.34}$$

where we immediately note that there in the incoherent contribution to the double-differential cross section of an inelastic neutron scattering experiment there is no selection over the exchanged momentum, but only over the exchanged energy ω. Thus, $S(\mathbf{Q},\omega)_{self,\pm 1}$ only depends on the *number* of modes whose $\omega_s(\mathbf{q})$ respects $\delta(\omega \mp \omega_s(\mathbf{q}))$ and because of this we can write this quantity as a function of the *phonon density of states* $\rho(\omega)$, where we average over all $(s,\mathbf{q})$.

$$S(\mathbf{Q},\omega)_{self,\pm 1} = \frac{N}{4M} e^{-2W(\mathbf{Q})} \frac{Q^2}{\omega} \rho(\omega) \langle n + \frac{1}{2} \pm \frac{1}{2} \rangle \tag{1.35}$$

where $3N$ is the total number of modes, $\langle n + \frac{1}{2} \pm \frac{1}{2} \rangle$ stands for the Bose-Einstein occupancy factor and since this formula does not depend on the direction of $\mathbf{Q}$,

we averaged $(\mathbf{Q}\cdot\boldsymbol{\varepsilon}_s(\mathbf{q}))^2$ over all directions, obtaining $Q^2/3$. In presence of more elements and/or nuclear isotopes, what is probed by an INS experiment is the *neutron-weighted phonon density of states*[45], defined as:

$$\rho_{nw}(\omega) = \sum_k \frac{\sigma_{inc,k}}{2M_k}\rho_k(\omega) \tag{1.36}$$

where k runs over all the elements (isotopes), and each $\rho_k(\omega)$ (partial density of states) is weighted by the mass and the cross section of its corresponding element (and isotope). A valuable tool in determining the phonon density of states for non-entirely incoherently scattering samples is the *incoherent approximation*[42,43]. This consists in measuring the double-differential cross section over a wide range of Q, effectively suppressing the Q-dependence of the coherent contribution to the signal and approximate all the signal as incoherent, thus determining the (neutron-weighted) phonon density of states.

1.4.6 Magnetic contribution to double differential cross-section

Magnetic scattering is given by the Zeeman interaction of the magnetic moment of the neutron $\boldsymbol{\mu}_n$ with the magnetic field distribution $\mathbf{B}(\mathbf{r})$ inside the sample:

$$V_{mag} = \boldsymbol{\mu}_n \cdot \mathbf{B}(\mathbf{r}) \tag{1.37}$$

where $\mathbf{B}(\mathbf{r})$ depends on both spin and orbital angular momenta of the unpaired electrons. Magnetic moments of neutrons and electrons are given by $\boldsymbol{\mu}_n = -\gamma\mu_N\boldsymbol{\sigma}_n$ ($\gamma = 1.913$) and $\boldsymbol{\mu}_e = -2\mu_B\mathbf{s}_e$. By writing $\mathbf{p}_e$ as the electron's momentum operator and $\mathbf{R}$ as the distance vector from the electron, we can write the interaction potential 1.37 in more detail:

$$V_{mag}(\mathbf{R}) = -\frac{\mu_0}{4\pi}2\gamma\mu_B\mu_N\boldsymbol{\sigma_n}\cdot\left[\nabla\times\left(\frac{\mathbf{s}_e\times\mathbf{R}}{R^2}\right)+\frac{1}{\hbar}\frac{\mathbf{p}_e\times\mathbf{R}}{R^2}\right] \tag{1.38}$$

where the first term between square brackets accounts for dipolar interaction, while the second term accounts for the magnetic interaction associated to the motion of the electron. Given the magnetic origin of the scattering event, calculating the matrix element of this interaction potential also requires to consider the spin state of the neutron: the initial state is $|\mathbf{k}_i,\nu_i,\sigma_i\rangle$ and the final state is $|\mathbf{k}_f,\nu_f,\sigma_f\rangle$. For the purposes of this thesis we only show the resulting formula for the double-differential cross section in the case of spin-only magnetic scattering of unpolarized neutrons by identical magnetic ions with localized electrons:

$$\left(\frac{d^2\sigma}{d\Omega dE_f}\right)_{mag} = (\gamma r_0)^2\frac{k_f}{k_i}F^2(\mathbf{Q})e^{-2W(\mathbf{Q})}\sum_{\alpha,\beta}\left(\delta_{\alpha\beta}-\frac{Q_\alpha Q_\beta}{Q^2}\right)S^{\alpha\beta}_{mag}(\mathbf{Q},\omega) \tag{1.39}$$

where $r_0 = \mu_0 e^2/(4\pi m_e)$ is the classical electron radius, $\alpha,\beta = x,y,z$ and $F(\mathbf{Q})$ is the magnetic form factor, defined as the Fourier transform of the spin density on the magnetic ions. The magnetic scattering function $S^{\alpha\beta}_{mag}(\mathbf{Q},\omega)$ can be written as:

$$S^{\alpha\beta}_{mag}(\mathbf{Q},\omega) = \sum_{j,k} e^{i\mathbf{Q}\cdot(\mathbf{R}_j-\mathbf{R}_k)} \sum_{\lambda,\lambda'} p_\lambda \langle\lambda|\hat{S}^\alpha_k|\lambda'\rangle \langle\lambda'|\hat{S}^\beta_j|\lambda\rangle \delta(\hbar\omega + E_\lambda - E_{\lambda'}) \quad (1.40)$$

where $\hat{S}^\alpha_k$ is the spin operator along direction α on the k-th nucleus site at position $\mathbf{R}_k$. All relevant information on the magnetic properties of the sample is stored in the magnetic scattering function, but the $\mathbf{Q}$-dependence of the double-differential cross section is also interestingly relevant thanks to the *polarization factor* and the *magnetic form factor*. The factor with the Kronecker delta in equation 1.39 (polarization factor) showcases how neutrons are sensitive only to components of the magnetic moment perpendicular to the scattering vector $\mathbf{Q}$, therefore allowing to determine moment directions or to distinguish different orientation of spin fluctuations. The magnetic form factor $F(\mathbf{Q})$ on the other hand, decreases by increasing the modulus of $\mathbf{Q}$, marking a behaviour typical of magnetic scattering and useful in isolating the magnetic contribution to the double-differential cross section.

1.4.7 Time-of-flight spectrometers

All the experiments performed throughout this work consisted in *inelastic neutron scattering* experiments on MERLIN[46], a time-of-flight (TOF) spectrometer located at the *ISIS Neutron and Muon Source* facility (UK). The basic working principle of a TOF spectrometer is that, by knowing the energy of the incident neutron, we can determine its final energy by measuring the time it took to fly from the sample to the detector. In fact, if L is the sample-detector distance and Δt is the elapsed time between sample and detector, the final energy is:

$$E_f = \frac{1}{2} m_n \frac{L^2}{\Delta t^2} \quad (1.41)$$

Since the exchanged energy is obtained by measuring a time delay, detectors allow to determine the exchanged momentum $\mathbf{Q}$ by measuring the scattering angle. On MERLIN it is possible to measure all three components of $\mathbf{Q}$ by exploiting its position-sensitive detectors, but it in this work we limited ourselves to measure its modulus, given the powder samples we studied.

A pulsed neutron beam is required for a TOF spectrometer since it allows us to exactly determine the time at which the neutron reaches the sample. This condition is easily met on MERLIN, where the neutrons originate from a spallation source, whose neutrons come naturally in pulses. On the other hand, the incident energy needs to be fixed by a monochromator before the sample, namely with a Fermi chopper[46]. In the experiments carried out in this work, we employed a Gd chopper, which imposes a 200 meV upper bound to the incident energy, but allows the use of the *repetition-rate multiplication mode*[47] (RRM). By exploiting RRM it is possible to separate the incoming pulse in pulses of different incident energy, determined by the rotating frequency of the Fermi chopper. All these pulses travel to the sample at different times, given the different energies, therefore it is possible to obtain spectra generated from multiple incident energies within a single neutron pulse. However, it is important to make sure that neutrons belonging to faster

pulses reach the detectors before neutrons belonging to slower pulses, otherwise causing a frame overlap and disrupting collected spectra. An example of this mode is displayed in Figure 1.1, representing the time at which neutrons with different energies reach the sample, in a particular RRM configuration.

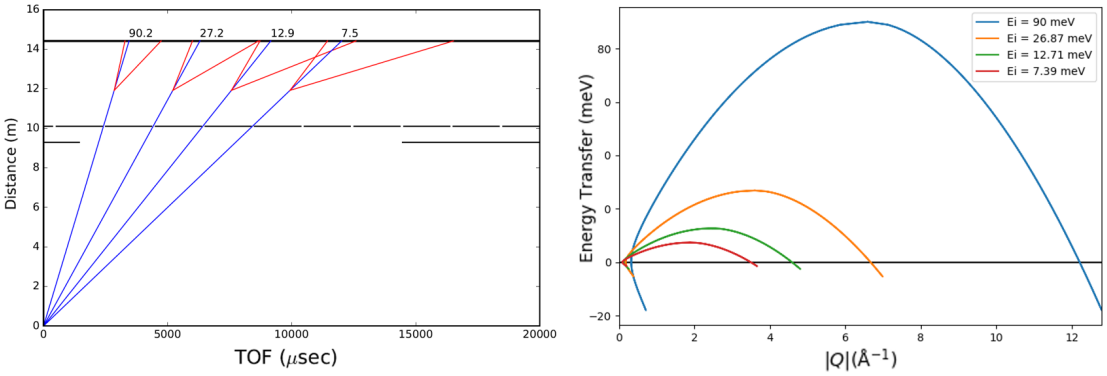

Figure 1.1: Left: distance vs time of flight plot for neutrons with incident energy $E_i = 90$ meV and Fermi chopper frequency $\nu = 250$ Hz. The four different energies incident on the sample are indicated at the solid line representing the detectors. Red lines define the TOF (i.e. exchanged energy) range that we can detect for each incident energy. Note that some of these regions slightly overlap each other, hindering signal collection in those energy ranges. Right: accessible kinematic range (Q, ω) for the same four configuration shown in the left panel.

Another relevant point for inelastic neutron scattering experiments concerns the accessible kinematic range of neutrons: with a given incident energy not all (Q, ω) values can be measured in an experiment. In fact, starting from equations 1.20 we can write energy $E_{i,f}$ as a function of the modulus of the wave-vector $|\boldsymbol{k}_{i,f}|$, obtaining a formula for Q^2:

$$\begin{aligned} Q^2 &= k_i^2 + k_f^2 - 2k_i k_f \cos(2\theta) \\ &= \frac{2m_n}{\hbar^2}\left[2E_i - \hbar\omega - 2\sqrt{E_i(E_i - \hbar\omega)}\cos(2\theta)\right] \end{aligned} \tag{1.42}$$

where 2θ is the scattering angle and, since it ranges from 0 to π, we can see that not every Q value is permitted for a given E_i, as shown in the right panel of Figure 1.1.

Chapter 2

Quantum Information Processing

In this chapter I will give an introduction to quantum information processing (QIP), starting from the basic mathematical concepts[48,49]. Then, I will introduce the topic of quantum error correction[50,51] (QEC) and its importance in the evolution of QIP. This topic will prove fundamental in two distinct sections of this thesis (see 3 and 4), since the works exposed within those chapters show how MNMs can be exploited in the future of QEC in an unparalleled manner.

2.1 Introduction to QIP

2.1.1 The *qubit*

The basic component of a quantum computer is the *qubit* (quantum bit), a quantum object defined in a 2-D Hilbert space spanned by the *computational basis* $\{|0\rangle, |1\rangle\}$. Here resides the main difference between a qubit and a classical bit: the former can exist in the states $|0\rangle$, $|1\rangle$ and in every possible *superposition* of these two.

$$|\psi\rangle = \alpha\,|0\rangle + \beta\,|1\rangle \tag{2.1}$$

where α and β are both complex numbers, denoting the fact that a qubit can be prepared in an infinite number of different states. However, always due to its quantum behaviour, a qubit can only be measured in $|0\rangle$ and $|1\rangle$ depending on the values of the coefficients α and β. In fact, a measurement of the generic state $|\psi\rangle$ will yield $|0\rangle$ with probability $|\alpha|^2$ and $|1\rangle$ with probability $|\beta|^2$. Since probability must sum to one it is safe to assume that $|\alpha|^2 + |\beta|^2 = 1$, therefore we can define the two complex coefficients as

$$\alpha = \cos(\theta/2) \quad , \quad \beta = e^{i\phi}\sin(\theta/2) \tag{2.2}$$

By using this notation $|\psi\rangle$ can be easily visualized as a point on a unitary sphere (Bloch sphere) defined by the two angular coordinates (θ, ϕ), where the two basis state occupy the two poles. With this picture in mind it might seem that a qubit can represent an infinite quantity of information, given the infinite points on the sphere. However, this *analogic* property of QIP is directly hindered by the fact that the measurement process can only yield one of two states, without further knowledge on an eventual previous superposition, hence the output is *digital*. In fact, the

quantum properties of qubits become especially relevant when considering multiple qubits, where the computational capabilities of the system increase exponentially.

If we consider the quantum state of two qubits, it can be written as a superposition of the four computational basis states

$$|\psi\rangle = \alpha\,|00\rangle + \beta\,|01\rangle + \gamma\,|10\rangle + \delta\,|11\rangle \tag{2.3}$$

where normalization still holds as $|\alpha|^2 + |\beta|^2 + |\gamma|^2 + |\delta|^2 = 1$, in which each term represents the probability of measuring the associated 2-qubit state. It is trivial to extend these considerations to n qubits, defining the computational basis as composed of 2^n different states, each one with its own coefficient in a generic superposition. Even by considering a relatively small number of qubits $n \approxeq 100$, the number of states contributing to the n-qubit state becomes incredibly large. Therefore, the *size* of the Hilbert space and how it scales exponentially with the number of qubits are key factors behind the computational power of quantum systems. Moreover, multiple qubits can experience *entanglement*, a quantum phenomenon which is also crucial in the development of quantum algorithms which outclass classic computation.

In order to comprehend how we can talk about *computation* with qubit-based systems, we must first define single-qubit gates and multiple-qubit gates, the building blocks of quantum computing.

2.1.2 One-qubit gates

Qubit gates are the quantum equivalent of logic gates in classical computation. A general qubit state, such as in Eq. 2.1, can be written in vector notation as:

$$|\psi\rangle = \begin{pmatrix} \alpha \\ \beta \end{pmatrix} \tag{2.4}$$

Therefore, single qubit gates can be expressed as 2×2 unitary matrices which change the state of the qubit. Basic single qubit operations can be represented by the Pauli matrices:

$$\sigma_x = \begin{pmatrix} 0 & 1 \\ 1 & 0 \end{pmatrix}, \sigma_y = \begin{pmatrix} 0 & -i \\ i & 0 \end{pmatrix}, \sigma_z = \begin{pmatrix} 1 & 0 \\ 0 & -1 \end{pmatrix} \tag{2.5}$$

where σ_x has the effect of switching the coefficients of $|0\rangle$ and $|1\rangle$, σ_z flips the sign of $|1\rangle$ and σ_y switches the coefficients while also flipping the sign. Note that, by considering the qubit state as a point (θ, ϕ) on Bloch sphere (2.2), every rotation about the x, y and z axis on the surface of the sphere can be expressed in terms of Pauli matrices as:

$$\begin{aligned}
R_x(\theta) &= e^{-i\theta\sigma_x/2} = \cos\frac{\theta}{2}\mathbb{1} - i\sin\frac{\theta}{2}\sigma_x = \begin{pmatrix} \cos\frac{\theta}{2} & -i\sin\frac{\theta}{2} \\ -i\sin\frac{\theta}{2} & \cos\frac{\theta}{2} \end{pmatrix} \\
R_y(\theta) &= e^{-i\theta\sigma_y/2} = \cos\frac{\theta}{2}\mathbb{1} - i\sin\frac{\theta}{2}\sigma_y = \begin{pmatrix} \cos\frac{\theta}{2} & -\sin\frac{\theta}{2} \\ \sin\frac{\theta}{2} & \cos\frac{\theta}{2} \end{pmatrix} \\
R_z(\theta) &= e^{-i\theta\sigma_z/2} = \cos\frac{\theta}{2}\mathbb{1} - i\sin\frac{\theta}{2}\sigma_z = \begin{pmatrix} e^{-i\theta/2} & 0 \\ 0 & e^{i\theta/2} \end{pmatrix}
\end{aligned} \tag{2.6}$$

Another important single qubit gate is the Hadamard gate, which transforms a computational basis state in a superposition of both, and is defined as:

$$H = \frac{1}{\sqrt{2}}\begin{pmatrix}1 & 1\\ 1 & -1\end{pmatrix} \quad , \quad H|0\rangle = \frac{|0\rangle + |1\rangle}{\sqrt{2}} \quad , \quad H|1\rangle = \frac{|0\rangle - |1\rangle}{\sqrt{2}} \tag{2.7}$$

2.1.3 Two-qubit gates and beyond

Since the computational power of QIP arises when considering multiple qubits, it is important to define also gates acting on more than one qubit. In fact, some properties of multiple-qubit gates have no classical counterpart and are key to the success of quantum computing. Additionally, such gates will hereby help us to introduce the phenomenon of quantum *entanglement*, which introduces correlations between distinct qubits which cannot be replicated by classical computation in any way. The most well-known of these gates is the controlled-not (CNOT) gate. This two-qubit gate has two input qubits, defined as the *control* qubit (C) and the *target* qubit (T). The CNOT gate applies a σ_x gate on the target qubit only if the control qubit is in $|1\rangle$, otherwise the target qubit is unaffected. This gate belongs to a class of two-qubit gates (controlled-U) which perform a one-qubit gate (U) on the target qubit depending on the state of the control qubit. Therefore, the CNOT gate can be seen as a controlled-σ_x gate and we can define in the same fashion any other controlled gate based on one-qubit gates, like controlled-σ_z (CZ). By writing the two-qubit state as a column vector of its coefficients in the order $|00\rangle$, $|01\rangle$, $|10\rangle$ and $|11\rangle$ and considering the first qubit as the control qubit, we can write CNOT and CZ gates in matrix form as

$$U_{CNOT} = \begin{pmatrix}1 & 0 & 0 & 0\\ 0 & 1 & 0 & 0\\ 0 & 0 & 0 & 1\\ 0 & 0 & 1 & 0\end{pmatrix}, U_{CZ} = \begin{pmatrix}1 & 0 & 0 & 0\\ 0 & 1 & 0 & 0\\ 0 & 0 & 1 & 0\\ 0 & 0 & 0 & -1\end{pmatrix} \tag{2.8}$$

and thanks to this matrix representation we can easily note how these gates leave unchanged the states $|00\rangle$ and $|01\rangle$ (with the control qubit in $|0\rangle$) whereas they perform a σ_x or σ_z on the subspace defined by the other two states (with the control qubit in $|1\rangle$). Two-qubit gates have an extraordinary property which closely links to the computational power of quantum computation: given that the operators associated to these gates are unitary, they are perfectly revertible. Hence, if we know the output state of a two-qubit gate, we can exactly determine the input state of that gate, which is not possible to do with classical logic gates.

Another innovation of quantum computation which separates it from classical computation is entanglement. In this regard, it is of great interest to see how a CNOT gate acts on the following state:

$$\hat{U}_{CNOT}\left[\frac{1}{\sqrt{2}}(|0\rangle_C + |1\rangle_C)\,|0\rangle_T\right] = \frac{1}{\sqrt{2}}(|0\rangle_C\,|0\rangle_T + |1\rangle_C\,|1\rangle_T) = \frac{1}{\sqrt{2}}(|00\rangle + |11\rangle) \tag{2.9}$$

In the initial state the target qubit is perfectly factorized from the control qubit, hence a measurement of one of the two qubits will yield no information about

the state of the other. This is not valid after the effect of the CNOT gate: by measuring one of the two qubits we are certain that the other qubit is found in the same state, without directly investigating its state. Therefore in the final two-qubit state the two qubits are *correlated* in such a way that they cannot be independently described. This property is called *entanglement* and it is of crucial importance in QIP, as well as being something strictly belonging to quantum physics, without a real classical counterpart. The aforementioned entangled state $(|00\rangle + |11\rangle)/\sqrt{2}$ is one of the so-called *Bell states*, defined as being *maximally entangled*, since the measurement of one qubit ensures the state in which we can find the other. As a matter of fact, qubits can also be entangled in such a way that the measurement of one qubit influences the measurement outcome on the other but without providing certainty of its state, like in 2.3.

However, not all two-qubit gates have this entangling property: gates such as the *swap* gate (exchanging the state of the two qubits) do not introduce any entanglement between unentangled qubits.

$$U_{SWAP} = \begin{pmatrix} 1 & 0 & 0 & 0 \\ 0 & 0 & 1 & 0 \\ 0 & 1 & 0 & 0 \\ 0 & 0 & 0 & 1 \end{pmatrix} \tag{2.10}$$

All these considerations on two-qubit gates and entanglement are easily extended on a greater number of qubits, keeping in mind that the number of multiple-qubit states accessible increases exponentially with the number of qubits. A three-qubit gate that will be used in one of the works presented in this thesis is the *Toffoli* gate (also known as *controlled-controlled-NOT* gate, CCNOT), which switches the state of the target qubit T depending on the state of the other two control qubits C1 and C2. By using the same criteria of the CNOT gate for control qubits, we can summarize the action of the Toffoli gate as:

$$\begin{aligned} \hat{U}_{CCNOT}\,|110\rangle &= \hat{U}_{CCNOT}\,|1\rangle_{C1}\,|1\rangle_{C2}\,|0\rangle_{T} = |1\rangle_{C1}\,|1\rangle_{C2}\,|1\rangle_{T} = |111\rangle \\ \hat{U}_{CCNOT}\,|111\rangle &= \hat{U}_{CCNOT}\,|1\rangle_{C1}\,|1\rangle_{C2}\,|1\rangle_{T} = |1\rangle_{C1}\,|1\rangle_{C2}\,|0\rangle_{T} = |110\rangle \end{aligned} \tag{2.11}$$

since it does not have any effect on the other six states of the three-qubit basis set. Therefore the matrix representation of this gate is an identity matrix in the subspace of these six states and a σ_x matrix in the $\{|110\rangle, |111\rangle\}$ subspace.

Entanglement on more than two qubits works in the same way as noted above, but with the main difference that within multiple qubits it is possible to have entanglement show up between a subset of qubits as well as between all of them.

2.1.4 Quantum circuits and algorithms

Analogously to classic computers, a quantum computing algorithm is associated to a precise sequence of gates, which in this case can be a bit more intricate to visualize. An accessible representation of quantum algorithms is given by quantum circuits, in which each *wire* represents a qubit and each gate is represented by a "box" or a symbol that connects all the qubits (wires) over which it acts. The order

in which the gates must be implemented is read from left to right and usually a quantum circuit ends with one or more measurements of the state. An example of a simple quantum circuit is given by the swap algorithm in figure 2.1, in which we swap the state of two qubits by the means of three CNOT gates. Note that the same result can be obtained by applying the *swap* gate, also represented in figure 2.1.

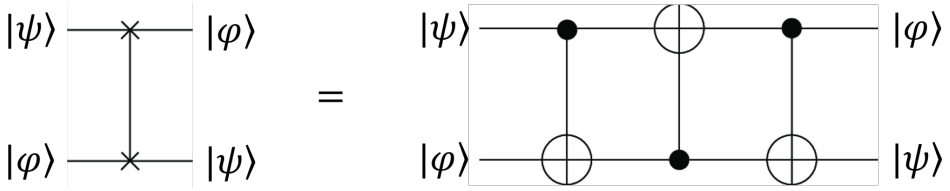

Figure 2.1: Left: representation of the *swap* gate in a quantum circuit. Right: decomposition of the swap gate in terms of three CNOT gates. The target qubit is indicated by the cross, whereas the dot indicates the control qubit.

The great interest of modern physics and IT in quantum computing emerges from the incredible possibilities granted by the quantum algorithms proposed in the last decades. A notable example of these is Shor's algorithm, which allows one to find the prime factors of an integer in a much more efficient way than what is possible within classical computation. This algorithm, as many others, is based on the idea of *quantum parallelism*: with a quantum computer it is indeed possible to evaluate a function $f(x)$ for different values of x at the same time. This is based on the possibility to obtain a generic superposition of all the states of the system. As an example, if we start with n qubits in $|0\rangle$ and we apply to each one of them a Hadamard gate, we obtain the n-qubit state

$$|\psi\rangle = \left(\frac{|0\rangle + |1\rangle}{\sqrt{2}}\right) \otimes \left(\frac{|0\rangle + |1\rangle}{\sqrt{2}}\right) \otimes \cdots \otimes \left(\frac{|0\rangle + |1\rangle}{\sqrt{2}}\right) = \frac{1}{2^{n/2}} \sum_x |x\rangle \tag{2.12}$$

where x runs over all the 2^n possible n-qubit states, all of them equally represented in this superposition, thanks to the action of the Hadamard gates. Now we consider an $n+1$-qubit state defined as $|\psi\rangle\,|0\rangle$ and a function which has the first n qubits as input and the last qubit as the output. If the function is implemented by the operator U_f, we define its action on a generic $n+1$-qubit state as

$$\hat{U}_f\,|x\rangle\,|0\rangle = |x\rangle\,|f(x)\rangle \tag{2.13}$$

where the output of $f(x)$ is computed on the $n+1$-th qubit. Therefore, if we apply this operator to the $n+1$-qubit state defined above, we obtain the state

$$\hat{U}_f\,|\psi\rangle\,|0\rangle = \hat{U}_f \left(\frac{1}{2^{n/2}} \sum_x |x\rangle\right) \otimes |0\rangle = \frac{1}{2^{n/2}} \sum_x |x\rangle\,|f(x)\rangle \tag{2.14}$$

in which the $n+1$-th qubit is in a superposition of all the possible values of $f(x)$. We have apparently calculated $f(x)$ for 2^n different values of x by applying only n Hadamard gates before implementing U_f. However, measurement and state

collapse put a limit to this procedure since only one output state can be measured of all the 2^n computed ones. Nonetheless, it is possible to extract information from such states with proper algorithms, still making some tasks exponentially faster thanks to quantum computers.

2.1.5 No-cloning theorem

The extraordinary properties of quantum entanglement have already shown us some of the great advantages it brings to quantum computation, but it can also cause some hurdles which are not trivial to circumvent. An important limit of QIP is the so-called *no-cloning theorem*. Being able to perfectly copy a bit of information is a key process in classical computing, but its implementation in quantum computing is much more difficult. The easiest method we could think of for copying a qubit onto another one is by using a CNOT gate: we begin by initializing the first qubit as $|\psi\rangle = \alpha|0\rangle + \beta|1\rangle$ and the second one as $|0\rangle$, then we apply a CNOT gate which has the first qubit as control and the second one as target, obtaining:

$$\hat{U}_{CNOT}\left(\alpha|00\rangle + \beta|10\rangle\right) = \alpha|00\rangle + \beta|11\rangle \tag{2.15}$$

At first sight this may look like a successful cloning of $|\psi\rangle$, but in reality this is true only if $\alpha = 0$ or $\beta = 0$, and note that these two cases represent the action of copying a classical bit of information. The correct copy of the state $|\psi\rangle$ should lead to the two-qubit state

$$|\psi\rangle|\psi\rangle = \alpha^2|00\rangle + \alpha\beta|01\rangle + \alpha\beta|10\rangle + \beta^2|11\rangle \tag{2.16}$$

which is impossible to obtain from the initial qubit, as we will shortly see. Another problem associated to the "badly-cloned" state $\alpha|00\rangle + \beta|11\rangle$ is that it is a highly entangled state: by measuring one of the two qubits we also exactly determine the state of the other one. This prevents us to obtain further information from these two qubits. On the other hand, by measuring one qubit in the "correctly-cloned" state $\alpha^2|00\rangle + \alpha\beta|01\rangle + \alpha\beta|10\rangle + \beta^2|11\rangle$ we do not lose the information stored in the other qubit at all, since it is a non-entangled state.

This is a simple and intuitive explanation of the no-cloning theorem, but it can be exactly proved in a fairly easy manner[48]: suppose we want to copy the unknown quantum state $|\psi\rangle$ in a target state which starts out in $|s\rangle$, so that the initial state of our system is $|\psi\rangle \otimes |s\rangle$. If we now suppose that the unitary operator $\hat{U}_c$ ideally performs the copying procedure for every possible input:

$$\begin{aligned} \hat{U}_c(|\psi\rangle \otimes |s\rangle) &= |\psi\rangle \otimes |\psi\rangle \\ \hat{U}_c(|\phi\rangle \otimes |s\rangle) &= |\phi\rangle \otimes |\phi\rangle \end{aligned} \tag{2.17}$$

where we applied $\hat{U}_c$ on two different unknown states. By taking the inner product of these two equations (left-hand side with left-hand side and right-hand side with right-hand side) we finally obtain

$$\langle\psi|\phi\rangle = \langle\psi|\phi\rangle^2 \tag{2.18}$$

which is true only when $\langle\psi|\phi\rangle = 1$ or when $\langle\psi|\phi\rangle = 0$. The former represents the trivial case in which $|\psi\rangle = |\phi\rangle$. The latter represents the case in which $|\psi\rangle$ and $|\phi\rangle$ are orthogonal, therefore it is not possible to perform quantum cloning operation on a generic state.

2.2 QIP: state of the art and current limits

In the most recent years, QIP received an important boost towards practical applications, occurred thanks to the efforts of the scientific community together with great IT companies (Google, Microsoft, Rigetti, Intel, IBM). These joint efforts ultimately culminated in building quantum processors composed of up to 53 qubits[52]. Some smaller quantum devices are already publicly available[53]: anyone can write simple quantum algorithms on its laptop and then run them remotely on quantum computers composed of few qubits. While these are all outstanding goals, QIP scientific research managed to reach the most important non-scientific news pages with the publication of an article announcing the achievement of *quantum supremacy*[52], the point at which quantum computers outclass the best classical computers available today. Despite being a controversial statement[54], it clearly displays how quantum computing is rapidly growing as a research field, really close to bringing information technology to an unprecedented turning point.

The most advanced quantum computers available nowadays are built using superconducting circuits as qubits, which guarantee good scalability and control. These quantum hardware are defined as noisy intermediate scale quantum computers[11] (NISQ) and represent the first big step towards the so-called "second quantum revolution". With these systems it will be in fact possible to perform calculations out of reach for a classical hardware and even quantum simulations of simple systems. However, even with the high control over qubit state and manipulation typical of superconducting qubits, there is a limit to the precision of each operation, hence the "noisy" definition. The more we increase the number of qubits and operations, the more we obtain imperfect results, causing the need to implement quantum error correction (QEC) codes. These codes aim to compensate the inherent errors in qubit manipulation and environment interaction by subsequently correcting such errors. However, QEC requires the information of a single logical qubit to be encoded in a larger Hilbert space, causing an additional growth of the size of the system. An effective implementation of QEC codes is one of the most challenging tasks to go beyond NISQ devices, towards a scalable, fault-tolerant architecture.

Given the limits of current technologies, it is a profitable time to look for physical alternatives to superconducting qubits. In this regard, $S = 1/2$ MNMs are interesting platforms. The possibility of chemical functionalization allows one to build supramolecular structures, as well as to graft these systems on surfaces. Moreover, one can engineer environmental interactions and coherence times. In this thesis we will introduce a striking advantage of molecular spins for QIP: the possibility of implementing simple QEC codes within a single molecule, effectively defining *error-protected units*. This possibility is of great interest, circumventing the inherent problem of QEC codes needing multiple physical units within current

NISQ hardware.

In the remaining sections of this chapter we will more extensively discuss the problem of *errors* in quantum systems and how QEC codes aim at correcting them. In Chapters 3 and 4 we will instead show how we implemented error-protected qubits within single-molecule systems, obtaining promising results.

2.3 Quantum error correction

Strictly quantum properties like superposition and entanglement are the key ingredients making QIP a thriving and fascinating research field, but quantum advantages are often associated to quantum problems. The main problem can in fact be identified in *quantum errors*: interaction with the environment can easily disrupt quantum information stored in a qubit, let alone in a whole quantum computer. Moreover, quantum gates and measurements are inherently flawed to some extent, introducing additional errors during their implementation. Many efforts in designing and building quantum hardware resistant to such errors have been successfully made: either by directly enhancing error resistance of the qubit and improving gate implementation, or by increasing computation speed, effectively reducing the probability of such errors taking place. However, qubits are intrinsically susceptible to such errors and, in order to reach a definitive breakthrough of quantum computation, this problem must be challenged head-first. Not surprisingly, the idea of being able to prevent or correct quantum errors have always been taken into high consideration since the birth of this research field. The most seminal papers on *quantum error correction*[55,56] (QEC) were in fact published in the same years as Shor's crucial publication of his algorithm for factoring integers[57]. QEC main goal consists in developing quantum algorithms suited for correcting errors that would otherwise disrupt quantum information. An inherent flaw of this approach can be summed up in the obvious question "How can we be sure to not introduce further errors during error correction procedures?". This problem is addressed by the theory of *fault-tolerant quantum computation*, which considers how even without a perfect implementation of QEC algorithms it is possible to obtain a substantial information recovery. In the next few sections we will discuss the physical origin and properties of quantum errors, the ideas behind QEC codes, some notable examples and how MNM can prove fundamental in the race towards *fault-tolerant quantum computation*.

2.3.1 Quantum errors

When a qubit interacts with the environment, it becomes entangled with it and this may lead to a loss of the information stored in the qubit. This phenomenon is referred to as *environmental decoherence* and it is the main source of error that QEC codes aim at correcting. On the other hand, incorrect implementation of the gates leads to a coherent and systematic error, better fixed by improving gate realization (if possible) or by coherent manipulation targeted for that specific error.

As an example, a generic quantum error on a single qubit can be written as a function of Pauli matrices (Eq. 2.6)[48]. Therefore, a quantum error on a single

qubit can act in three different ways: *phase flip*, *bit flip*, a combination of both, or neither. Phase flip can be represented with the action of the σ_z Pauli matrix on the qubit state. In the same fashion bit flip and bit & phase flip act as σ_x and σ_y matrices. To these three matrices we also add the 2×2 identity matrix (σ_I), which represents the "no error" case. Every error on a single qubit can be expressed as a linear combination of these matrices, which form the *Pauli group*.

At this point we have to address two important issues: the *continuous* nature of quantum errors and the possibility of multiple errors to be *correlated*. The former is quite obvious: qubits do not undergo discrete phase flips or bit flips, but *continuous* errors. In this regard QEC protocols have the effect of *digitizing* the error by collapsing through a non-destructive measurement the state of the system into a discrete set of bit flips and/or phase flips (depending on the specific code). This will be much clearer when we will introduce some notable examples of QEC algorithms. The latter, on the other hand, represents a weakness of QEC: a crucial assumption of the simplest QEC codes is that errors on different qubits are independent from one another. This is not always true and, as we will shortly see, most QEC codes are based on the idea of encoding a single logical qubit in multiple physical qubits, exploiting the larger size of the Hilbert space. This choice has the side-effect of introducing the possibility of errors occurring on more than one qubit, therefore physical implementations of such codes have to be carefully designed in order to avoid correlated errors.

Lastly, there are other possible errors in QIP that we will not further investigate but it is nonetheless important to mention them. The first two are qubit *loss* and *leakage*. Qubit loss occurs when the information of a qubit is entirely lost, usually through relaxation, whereas qubit leakage is associated to the unwanted population of a level of the system outside of the computational basis. Other potential sources of error are state *initialization* and *measurement*, usually found at the beginning and at the end, respectively, of a quantum algorithm. In the former case the initial state is different from what had to be prepared, while in the latter the measurement outcome does not match to the real collapsed state.

2.3.2 QEC: basic ideas and QEC codes

In classical information processing, the preservation of the bit state against errors is based around the idea of *redundancy*: the bit state (either 0 or 1) is copied to other qubits and, when each one of them is measured after a given time, the correct state is chosen as the most measured of the bunch. This is called *majority voting*, which is a simple but efficient way of detecting and correcting errors on classical bits of informations and its only assumption is a low enough error probability on each qubit. In QIP the idea of majority voting has an inherent problem: the *no-cloning theroem* (2.1.5) prevents us from copying the qubit state without irreversibly entangling it with its copy. However, QEC codes circumvent this major hurdle by *exploiting* this entanglement.

Three-qubit code The paradigm of all QEC codes is the three-qubit code (TQC), and it is indeed really useful in understanding the key ideas behind QEC, as well as all the more complex *repetition codes*, of which the TQC is the easiest

example. Such codes are based on encoding a single logical qubit into multiple physical qubits,a process reminiscent of the redundancy typical of classical majoruty voting-based error correction. Not surprisingly, TQC utilizes three physical qubits to correct a single error on a logical qubit. The version of the TQC that we are going to introduce now is designed to correct a single bit-flip error, whereas the TQC that corrects phase-flip errors will be shortly treated afterwards, since it involves only small tweaks to the bit-flip TQC.

We start with a generic qubit state $|\psi\rangle$ which we would like to preserve:

$$|\psi\rangle = \alpha\,|0\rangle + \beta\,|1\rangle \tag{2.19}$$

Then we prepare a three qubit state $|\overline{\psi}\rangle$ by entangling this qubit with two other qubits both previously prepared in $|0\rangle$ via the quantum circuit in figure 2.2. This procedure is called *encoding*: the state of a single *physical* qubit $|\psi\rangle$ is encoded in three physical qubits, defining a *logical* qubit $|\overline{\psi}\rangle$, with its own logical $|\overline{0}\rangle$ and $|\overline{1}\rangle$ states.

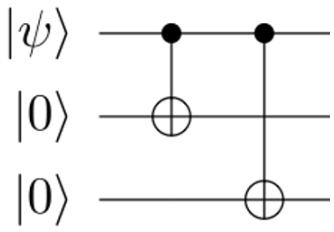

Figure 2.2: Quantum circuit for the encoding of the qubit state $|\psi\rangle$ in the three-qubit state $|\overline{\psi}\rangle$.

The quantum circuit implementing the encoding is composed of two CNOT gates, which act on the initial three-qubit state $\alpha\,|000\rangle + \beta\,|100\rangle$ obtaining the *encoded* state:

$$|\overline{\psi}\rangle = \alpha\,|000\rangle + \beta\,|111\rangle = \alpha\,|\overline{0}\rangle + \beta\,|\overline{1}\rangle \tag{2.20}$$

The encoded state is the state on which any single bit flip error on one of the three physical qubits can be detected and corrected. Note that any error that takes place before or during encoding (e.g. poor initialization or imperfect gate implementation) is impossible to detect with this code, and the same is true for all QEC codes.

At this point the encoded state can experience four different scenarios that we are able to detect with the TQC:

$$\begin{aligned}
\text{no error:}\quad & |\overline{\psi}\rangle = \alpha\,|000\rangle + \beta\,|111\rangle \\
\text{bit flip on qubit 1:}\quad & |\overline{\psi}\rangle = \alpha\,|100\rangle + \beta\,|011\rangle \\
\text{bit flip on qubit 2:}\quad & |\overline{\psi}\rangle = \alpha\,|010\rangle + \beta\,|101\rangle \\
\text{bit flip on qubit 3:}\quad & |\overline{\psi}\rangle = \alpha\,|001\rangle + \beta\,|110\rangle
\end{aligned} \tag{2.21}$$

We now have to distinguish which one of these four events actually took place, but keep in mind that measuring the state of the logical qubit would destroy the

quantum information associated to the superposition. Therefore, we need two *ancillary qubits* (simply referred to as *ancillae*, both prepared in $|0\rangle$) which are coupled to the three physical qubits and that we can measure without collapsing the logical qubit state. The measurement of these ancillae is called *syndrome diagnosis* (figure 2.3) and it determines in which one of the four cases we find the system is.

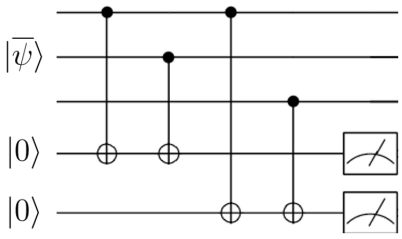

Figure 2.3: Quantum circuit implementing the error detection procedure in the TQC. The bottom two wires are the two ancillae, whereas the top three are the qubits encoding the logical qubit. The boxes at the end of the ancillae wires represent a measurement process.

By applying the quantum circuit in figure 2.3 to each case reported in 2.21 it is easy to see that we obtain these four different states:

$$\begin{aligned} \text{no error: } & (\alpha\,|000\rangle + \beta\,|111\rangle) \otimes |00\rangle_A \\ \text{bit flip on qubit 1: } & (\alpha\,|100\rangle + \beta\,|011\rangle) \otimes |11\rangle_A \\ \text{bit flip on qubit 2: } & (\alpha\,|010\rangle + \beta\,|101\rangle) \otimes |10\rangle_A \\ \text{bit flip on qubit 3: } & (\alpha\,|001\rangle + \beta\,|110\rangle) \otimes |01\rangle_A \end{aligned} \tag{2.22}$$

where $|\rangle_A$ indicates the state of the two ancillae, which are disentangled from the logical qubit, hence they can be measured preserving the superposition of the logical state. Each one of the four possible ancillae measurement outcomes (*syndromes*) is univocally associated to one of the four cases which the TQC can correct. Once we know the error syndrome we can easily correct any error by applying a σ_x one-qubit gate to the physical qubit for which we diagnosed the error, or by doing nothing in the *no error* case. At this point we have successfully restored the encoded state from a single bit flip on one of the three physical qubits.

If we wanted to write a quantum circuit for a TQC that corrects a single phase flip on one qubit we should have added to the encoding procedure an Hadamard gate on each qubit after the two CNOT gates, obtaining the encoded state

$$|\overline{\psi}\rangle = \alpha\,|+++\rangle + \beta\,|---\rangle = \alpha\,|\overline{0}\rangle + \beta\,|\overline{1}\rangle \tag{2.23}$$

where $|+\rangle = (|0\rangle + |1\rangle)/\sqrt{2}$ and $|-\rangle = (|0\rangle - |1\rangle)/\sqrt{2}$. On this encoded state the effect of a phase flip error is that of switching $|+\rangle$ and $|-\rangle$ on the qubit on which it acts, causing four possible scenarios, analogous to those of the TQC for bit flip errors. In order to correctly perform the syndrome detection procedure we now have to add a Hadamard gate on each qubit before the CNOT gates that couple

the qubit to the ancillae. In this way we obtain the same logical qubit states as in 2.22, where by measuring the ancillae state we are now able to detect a single phase flip error on one of the physical qubits and then correct it with the action of a σ_z gate on that specific qubit.

As already stated, the TQC is able to correct only a single error on a qubit, but what happens if an error occurs on more than one physical qubit? Let us focus on the bit-flip code since it is easier to visualize and every observation that will be made still holds true for the phase-flip code, given that the syndrome extraction is analogous. In the case of two or three independent bit-flip errors we have four possible outcomes:

$$\begin{aligned} \text{bit flip on qubit 1 and 2: } & |\overline{\psi}\rangle = \alpha\,|110\rangle + \beta\,|001\rangle \\ \text{bit flip on qubit 1 and 3: } & |\overline{\psi}\rangle = \alpha\,|101\rangle + \beta\,|010\rangle \\ \text{bit flip on qubit 2 and 3: } & |\overline{\psi}\rangle = \alpha\,|011\rangle + \beta\,|100\rangle \\ \text{bit flip on qubit 1, 2 and 3: } & |\overline{\psi}\rangle = \alpha\,|111\rangle + \beta\,|000\rangle \end{aligned} \tag{2.24}$$

Each one of these logical qubit states then interacts with the ancillae in the same way as before, as shown by the circuit in figure 2.3, finally measuring the following error syndromes:

$$\begin{aligned} \text{bit flip on qubit 1 and 2: } & (\alpha\,|110\rangle + \beta\,|001\rangle) \otimes |01\rangle_A \\ \text{bit flip on qubit 1 and 3: } & (\alpha\,|101\rangle + \beta\,|010\rangle) \otimes |10\rangle_A \\ \text{bit flip on qubit 2 and 3: } & (\alpha\,|011\rangle + \beta\,|100\rangle) \otimes |11\rangle_A \\ \text{bit flip on qubit 1, 2 and 3: } & (\alpha\,|111\rangle + \beta\,|000\rangle) \otimes |00\rangle_A \end{aligned} \tag{2.25}$$

If we now apply a σ_x gate correcting the errors associated to each syndrome following what we learnt in 2.22 we notice that we do not correctly restore the encoded state while instead we further destroy the information stored in the logical qubit. Hence, not only the TQC is not able to correct more than one error, but it is also not possible for it to detect multiple errors, since it mistakes those cases for single correctable errors. Therefore, it is important in all implementations of such codes to have a very low probability of an error occurring on more than one qubit, given the impossibility to detect this event as a fail-case scenario.

Chapter 3

A Rare-Earth Trimer as a Quantum Error Corrected Logical Qubit

E. Macaluso, M. Rubín, D. Aguilà, A. Chiesa, L. A. Barrios, J. I. Martínez, P. J. Alonso, O. Roubeau, F. Luis, G. Aromí and S. Carretta, A heterometallic [LnLn'Ln] lanthanide complex as a qubit with embedded quantum error correction, *Chemical Science*, **11**, 10337-10343, 2020

This work has been made possible thanks to the help of the group from *Universitat de Barcelona*, which synthesized the molecule and performed chemical and structural characterization, and of the group from *Universidad de Zaragoza*, which performed magnetic characterization of the sample.

This chapter presents the first of two different works which constituted a big part of the research I carried out in my PhD years, the second one being shown in the next chapter. Both are focused on the innovation that MNMs can bring to QIP, namely in the field of QEC. The possibility to perform entire QEC schemes within a single molecule, which encodes a logical qubit, is the common ground between the two chapters. This innovation could solve big limits for the implementation of such codes in current quantum computation hardware. Moreover, chemical engineerability of MNMs allows one to synthesize tailored molecules for specific codes. In this chapter we propose to use three rare-earth ions of a MNM to encode as many physical qubits into a molecular logical qubit. By designing a proper pulse sequence, a variation of the TQC can be implemented on this molecule, protecting one of the qubits from a single phase flip error.

The main protagonist of this work is the molecule $[CeEr_2(LA)_2(LB)_2(py)(NO_3)]$, whose molecular structure is shown in Figure 3.1 and from now on referred to as $[ErCeEr]^{58}$ (**1**). As clearly displayed in the figure, the magnetic core of this MNM is composed of three rare-earth ions, whose positions are almost collinear. All three ions can be efficiently described as an effective spin 1/2, given their well isolated ground state. Hence, by using each ion as a single physical qubit, we can exploit all three of them to encode a logical qubit on which it is possible to perform a

QEC code based on the well-known three qubit code (TQC, see section 2.3.2). This has been made possible by thorough experimental characterization, which allowed us to determine the Hamiltonian parameters describing the 8 lowest energy levels of the trimer. Moreover, the same characterization has also been performed on the isostructural analogues [LuCeLu] (**2**) and [ErLaEr] (**3**), in which Ce^{3+} and Er^{3+} ions have been replaced by the diamagnetic ions La^{3+} and Lu^{3+}, respectively. This allowed an even more precise determination of the aforementioned parameters. With the Hamiltonian describing the trimer fully fleshed out, we proceeded to simulate the performance of the TQC, correcting a phase flip on the central Ce^{3+} ion. This has been achieved by numerically simulating a tailored pulse sequence together with pure dephasing in the Lindblad formalism, obtaining a significant suppression of the error.

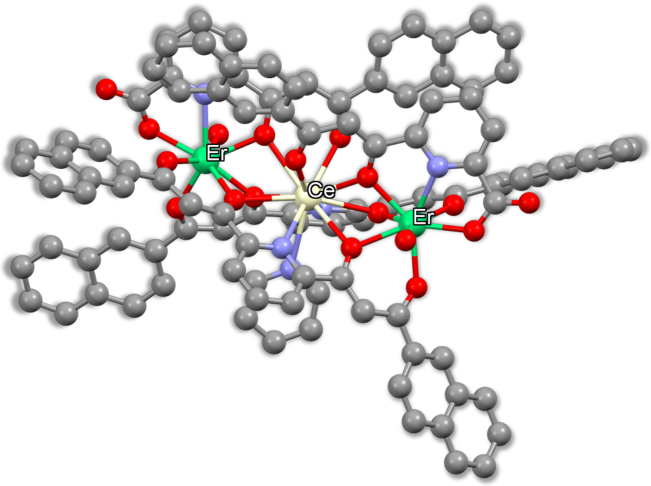

Figure 3.1: Molecular structure of **1**. Er^{3+} ions are displayed in green and Ce^{3+} in yellow. O atoms are in red, C in grey and N in light purple. Hydrogen atoms not shown for simpler visualization.

3.1 Characterization

All three molecules have been characterized via continuous wave EPR (cw-EPR), magnetometry and calorimetry measurements. Experiments on **2** and **3** allowed us to independently determine g tensors for both magnetic ions. Using these values when fitting experimental data collected on **1**, we have been able to more precisely determine the nature and intensity of magnetic interaction between the ions.

Magnetic measurements were performed using a Quantum Design SQUID MPMS-XL magnetometer through the Physical Measurements unit of the Servicio de Apoyo a la Investigación-SAI, Universidad de Zaragoza. Heat capacity data were measured with a commercial physical property measurement system (PPMS, Physical Measurements unit of the Servicio de Apoyo a la Investigación-SAI, Universidad de Zaragoza) that makes use of the relaxation method. Cw-EPR measurements were performed in Universidad de Zaragoza with a Bruker Biospin ELEXSYS E-580 spectrometer operating in the X-band.

All experiments were performed on polycrystalline samples obtained by crushing single crystals. We also performed cw-EPR measurements on a frozen saturated solution of **1** in a 1 : 1 MeOH/EtOH nondeuterated mixture. My contribution to sample characterization consisted in properly fitting all data collected on the three samples, finally obtaining the spin Hamiltonian parameters.

In addition, pulsed Time Domain (TD) EPR measurements were performed at X-band frequencies on the aforementioned frozen solution of **1**. These experiments were done by the group in Universidad de Zaragoza in order to estimate the coherence time scales typical of this system, even under non-optimal conditions.

3.1.1 [LuCeLu]

Through susceptibility measurements performed on **2** (Figure 3.2) it has been possible to ensure that, at liquid Helium temperatures, the Ce^{3+} ion can be described as an effective spin doublet, separated from the closest excited doublet by a gap $\Delta = 210$ K. Data analysis of susceptibility measurements was performed by our collaborators at Universidad de Zaragoza.

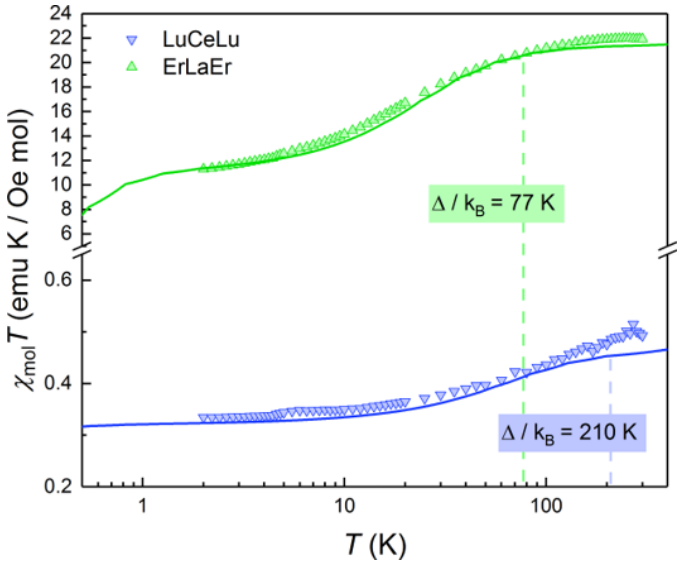

Figure 3.2: χT as a function of T measured on samples **2** and **3**. its increase with T is associated to a growing population of excited doublets, showing that at liquid Helium temperatures Ce^{3+} and Er^{3+} behave as effective spin doublets. Solid lines are least-square fits made with a simplified version of the Van-Vleck susceptibility[59] model that takes into account two spin doublets, allowing the estimation of the energy gap Δ that separates them. Reproduced from Ref. [60] with permission from the Royal Society of Chemistry.

Given the possibility to describe the Ce^{3+} ion as an effective spin $S = 1/2$, the low-energy Hamiltonian describing this molecule is the easiest of the three:

$$H_{\mathbf{2}} = \mu_B \mathbf{S} \cdot \mathbf{g}_{Ce} \cdot \mathbf{B} \tag{3.1}$$

which only contains a Zeeman term, given the absence of interaction with other

magnetic ions. The g-tensor $\mathbf{g}_{Ce}$ was determined through combined cw-EPR, magnetization and specific heat measurements.

By fitting cw-EPR data with the model in Eq. 1.19 (Figure 3.3, right panel), we determined an almost isotropic $g_{Ce} \approx 1.85$. Note that the dip near 200 mT in the EPR spectrum and the background signal above 500 mT correspond with features observed in measurements of the bare quartz tubes, which have likely not been completely corrected, on account of the low signal arising from the sample. Magnetization data allowed for a more precise determination of $\mathbf{g}_{Ce}$, by fitting experimental data with the model in Eq. 1.12, obtaining an axially anisotropic $\mathbf{g}_{Ce} = (1.7, 1.7, 2.2)$ (Figure 3.3. left panel). The fitting of specific heat data using the model 1.15 with the same choice $\mathbf{g}_{\mathrm{Ce}} = (1.7, 1.7, 2.2)$ gave a really good agreement (Figure 3.3, central panel), therefore fixing the value of the Ce^{3+} ion g-factor.

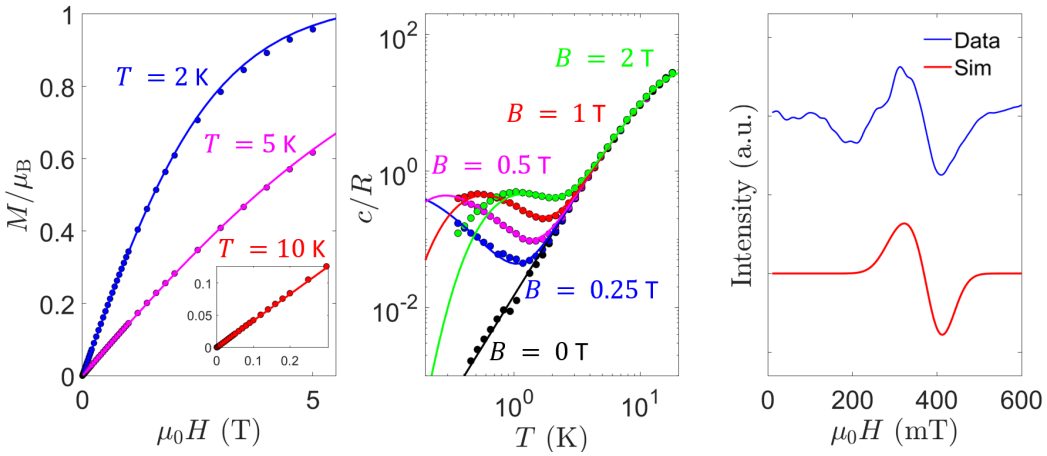

Figure 3.3: Left panel: magnetization as a function of magnetic field on **2**, experimental data (circles) and calculation (solid lines) at three different temperatures. Central panel: specific heat as a function of temperature on **2**, experimental data (circles) and calculation (solid lines) at five different static field values. Right panel: cw-EPR data measured on **2** (blue line) at $T = 4.5$K together with the spectrum simulated with the Easyspin[61,62] package for MATLAB (red line). In all calculations we used an anisotropic $\mathbf{g}_{\mathrm{Ce}} = (1.7, 1.7, 2.2)$. Reproduced from Ref. [60] with permission from the Royal Society of Chemistry.

In order to simplify the subsequent determination of magnetic interactions between the ions, we chose to keep the model as simple as possible by using the isotropic $\mathbf{g}_{\mathrm{Ce}} = (1.85, 1.85, 1.85)$, which still shows an overall very good agreement with experimental data, as shown in Figure 3.4. Both choices for $\mathbf{g}_{\mathrm{Ce}}$ are compatible with the lowest energy doublet of a spin $J = 5/2$ (with $g_J = 6/7$) in a proper crystal field cage, albeit not with cubic symmetry. The isotropic $\mathbf{g}_{\mathrm{Ce}}$ choice proved itself very helpful when fitting experimental data collected on **1**, given the higher number of degrees of freedom that would be introduced by having three anisotropical g-factors. Moreover, eigenvalues and eigenstates of **1** used for simulations of the QEC code are not sensitively influenced by this choice, making our conclusions valid in both cases.

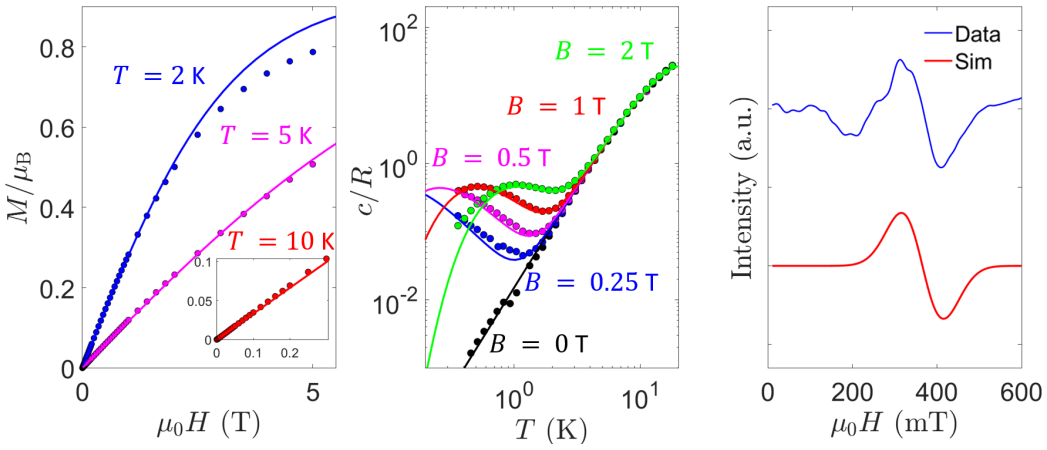

Figure 3.4: Left panel: magnetization as a function of magnetic field on **2**, experimental data (circles) and calculation (solid lines) at three different temperatures. Central panel: specific heat as a function of temperature on **2**, experimental data (circles) and calculation (solid lines) at five different static field values. Right panel: cw-EPR data measured on **2** (blue line) at $T = 4.5$K together with the spectrum simulated with the Easyspin[61,62] package for MATLAB (red line). In all calculations we used an isotropic $\mathbf{g}_{\mathrm{Ce}} = (1.85, 1.85, 1.85)$. Reproduced from Ref. [60] with permission from the Royal Society of Chemistry.

3.1.2 [ErLaEr]

In the same fashion as on **2**, susceptibility measurements on **3** allowed the detection of an effective spin $S = 1/2$ ground state, well isolated from the closest excited doublet by a gap $\Delta = 77$ K (Figure 3.2). The low-energy Hamiltonian describing this molecule includes Zeeman contributions from the two ions, as well as magnetic interaction between them:

$$H_{\mathbf{3}} = \mu_B(\mathbf{S}_1 \cdot \mathbf{g}_{Er,1} \cdot \mathbf{B} + \mathbf{S}_2 \cdot \mathbf{g}_{Er,2} \cdot \mathbf{B}) + \mathbf{S}_1 \cdot \mathbf{J}_{1,2} \cdot \mathbf{S}_2 \tag{3.2}$$

Given the distance between the magnetic Er^{3+} ions and the abundance of interposing ligands (as shown in Figure 3.5), we expected the strength of the exchange interaction to be negligible. On the other hand, dipolar interaction has to be evaluated (point dipole approximation with Eq. 1.5) in order to correctly determine the value of $\mathbf{J}_{1,2}$. Additionally, molecules in the crystal are arranged in such a way that the two closest Er^{3+} ions of neighbouring molecules are closer to each other (≈ 6 Å) than the two belonging to the same molecule (≈ 7.9 Å), causing a sizeable inter-molecule dipolar interaction. This interaction is fortunately restricted to couples of molecules, since each molecule has only one nearest neighbour. Hence, simulations on **3** have been performed by considering two molecules, whose spin Hamiltonian describes a "chain" of four Er^{3+} ions with closest-neighbour magnetic interaction:

$$\begin{aligned} H_{\mathbf{3}} =& \mu_B(\mathbf{S}_1 \cdot \mathbf{g}_{Er,1} \cdot \mathbf{B} + \mathbf{S}_2 \cdot \mathbf{g}_{Er,2} \cdot \mathbf{B} + \mathbf{S}_1 \cdot \mathbf{g}_{Er,3} \cdot \mathbf{B} + \mathbf{S}_2 \cdot \mathbf{g}_{Er,4} \cdot \mathbf{B}) \\ &+ \mathbf{S}_1 \cdot \mathbf{J}_{1,2} \cdot \mathbf{S}_2 + \mathbf{S}_2 \cdot \mathbf{J}_{2,3} \cdot \mathbf{S}_3 + \mathbf{S}_3 \cdot \mathbf{J}_{3,4} \cdot \mathbf{S}_4 \end{aligned} \tag{3.3}$$

where subscripts 1 and 2 denote the ions of one molecule, 3 and 4 those of the other, $\mathbf{J}_{1,2}$ and $\mathbf{J}_{3,4}$ intra-molecule interaction, and $\mathbf{J}_{2,3}$ inter-molecule interaction. Quite obviously, all observables computed from these simulations must be divided by 2 to refer to the single molecule. Another important consideration we made by observing the molecular structure is that the two Er^{3+} ions within a single molecule have almost the same ligand cage, albeit rotated. Therefore, their g-tensors are also related by a rotation matrix, which we determined by comparing the two surroundings:

$$R = \begin{pmatrix} -0.9980 & 0.0628 & 0.0000 \\ 0.0568 & 0.9030 & -0.4258 \\ -0.0267 & -0.4249 & -0.9048 \end{pmatrix} \tag{3.4}$$

With this matrix we defined $\mathbf{g}_{Er,2} = R^{-1}\mathbf{g}_{Er,1}R$, leaving us with $\mathbf{g}_{Er,1}$ as the only free parameter of the fit, together with an eventual exchange interaction on top of dipolar interaction.

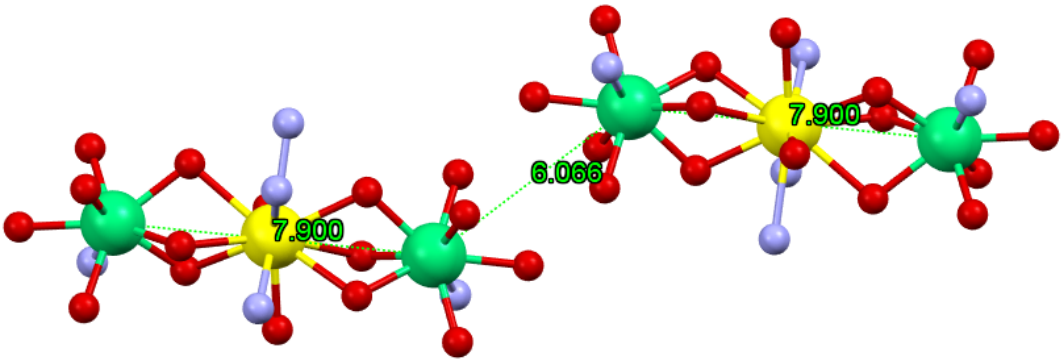

Figure 3.5: Two neighbouring [ErCeEr] molecules in a crystal. Note that Er^{3+} ions of different molecules are closer than those in the same molecule (distances are reported in Å), hence inter-molecule dipolar interaction is relevant. Er^{3+} ions are displayed in green and Ce^{3+} in yellow. O atoms are in red, C in grey and N in light purple (H atoms not shown). Note that this figure only shows the ligand cage of each magnetic ion, for an easier readability.

With this in mind we can now fully characterize **3**. Specific heat experiments clearly display the presence of an energy gap at $B = 0$ T, indicating sizeable magnetic interaction (3.6, central panel). This is very well represented by simulations including only dipolar interaction and considering the largest $\mathbf{g}_{Er,1}$ component to be around (11.5 ± 0.3) and directed along the axis between the two ions of the same molecule. Such a big value of $\mathbf{g}_{Er,1}$ is also confirmed by the low-field features of the cw-EPR spectrum measured on **3** (Figure 3.6, right panel). Moreover, features around $100 - 200$mT clearly point towards an intermediate $\mathbf{g}_{Er,1}$ value of (5.0 ± 0.3). Finally, by simultaneously fitting magnetization measurements (Figure 3.6, left panel) and other experimental data, we found the lowest value of $\mathbf{g}_{Er,1}$ to be of (1 ± 1). Such a big uncertainty in its determination is due to the broadening of high-field features in cw-EPR spectra and the consequent difficulty in precisely determine a lower bound.

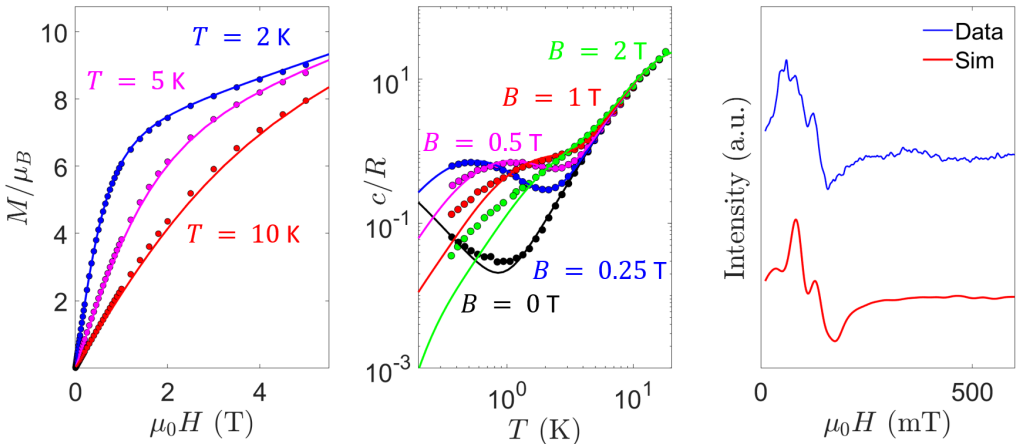

Figure 3.6: Left panel: magnetization as a function of magnetic field on **3**, experimental data (circles) and calculation (solid lines) at three different temperatures. Central panel: specific heat as a function of temperature on **3**, experimental data (circles) and calculation (solid lines) at five different static field values. Right panel: cw-EPR data measured on **3** (blue line) at $T = 4.5$K together with the spectrum simulated with the Easyspin[61,62] package for MATLAB (red line). Reproduced from Ref. [60] with permission from the Royal Society of Chemistry.

In summary, by fitting experimental data collected on **3**, we obtained:

$$\mathbf{g}_{Er,1} = \begin{pmatrix} 1 & 0 & 0 \\ 0 & 5 & 0 \\ 0 & 0 & 11.5 \end{pmatrix} \tag{3.5}$$

which through the rotation matrix R allows us to calculate $\mathbf{g}_{Er,2}$. Note that these two g-tensors exactly determine the dipolar interaction between the two Er^{3+} ions (Eq. 1.5), since no additional term was needed.

3.1.3 [ErCeEr]

Having determined g-tensors for Ce^{3+} and both Er^{3+} ions, we proceeded by using these parameters in the Hamiltonian describing **1**, looking for a potential exchange interaction between the closest Er and Ce ions.

$$\begin{aligned} H_0 =& \mu_B(\mathbf{S}_{Er,1} \cdot \mathbf{g}_{Er,1} + \mathbf{S}_{Ce} \cdot \mathbf{g}_{Ce} + \mathbf{S}_{Er,2} \cdot \mathbf{g}_{Er,2}) \cdot \mathbf{B} \\ &+ \mathbf{S}_{Er,1} \cdot \mathbf{J}_{1,2} \cdot \mathbf{S}_{Ce} + \mathbf{S}_{Ce} \cdot \mathbf{J}_{2,3} \cdot \mathbf{S}_{Er,2} + \mathbf{S}_{Er,1} \cdot \mathbf{J}_{1,3} \cdot \mathbf{S}_{Er,2} \end{aligned} \tag{3.6}$$

where $\mathbf{J}_{1,2}$ and $\mathbf{J}_{2,3}$ describe dipolar magnetic interaction between the ions of different species, and $\mathbf{J}_{1,3}$ describes dipolar magnetic interaction between the two Er^{3+} ions within the same molecule. Similarly to what we did for **3**, we had to consider two adjacent molecules when simulating data for specific heat and magnetization measurements, given the relevant inter-molecule dipolar interaction. However, cw-EPR measurements were performed on a diluted sample, allowing us to focus on the intra-molecular interaction. Without including any additional isotropic Er-Ce

magnetic interaction besides dipolar interaction in the Hamiltonian, our model reasonably fits the zero-field gap which appears on specific heat measurements (3.7, panel (a)). Additionally, it gives a good fit also for magnetization data (3.7, panel (b)) and the cw-EPR spectrum (3.7, panel (c)).

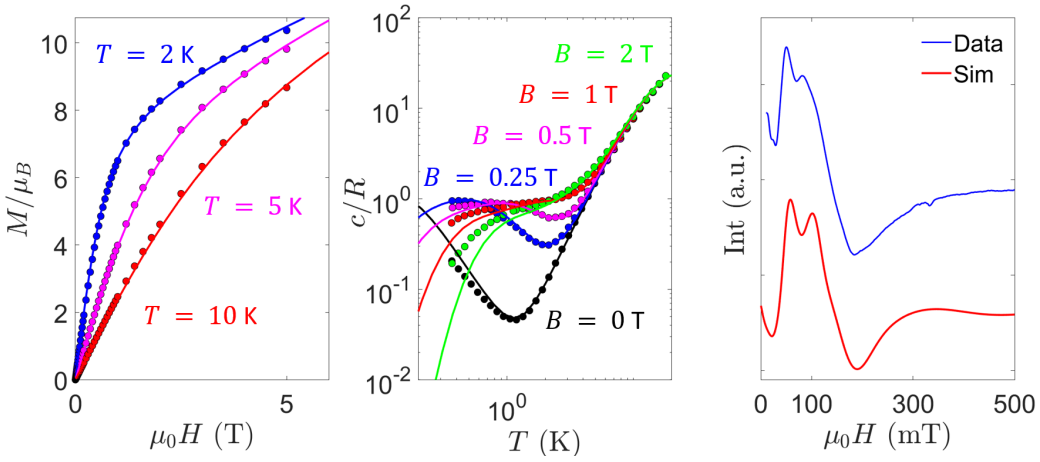

Figure 3.7: Left panel: magnetization as a function of magnetic field on **1**, experimental data (circles) and calculation (solid lines) at three different temperatures. Central panel: specific heat as a function of temperature on **1**, experimental data (circles) and calculation (solid lines) at five different static field values. Right panel: cw-EPR data measured on a diluted **1** sample (blue line) at $T = 4.5$K together with the spectrum simulated with a tailored program (red line), which uses an energy-fixed peak width[63,64]. Reproduced from Ref. [60] with permission from the Royal Society of Chemistry.

We also performed some simulations in presence of a smaller isotropic exchange contribution J to be added to $\mathbf{J}_{1,2}$ and $\mathbf{J}_{2,3}$. Also in this case, zero-field specific heat measurements allow us to rule out a significant ferromagnetic exchange, since even a small $J = -0.1\text{cm}^{-1}$ clearly worsens the agreement between data and simulation (Figure 3.8). Anti-ferromagnetic exchange is more easily ruled out by cw-EPR spectra, where $J = 0.1-0.15\text{cm}^{-1}$ evidently distorts various features in an incompatible way (Figure 3.9). Such small values for the exchange interaction J do not alter the performance of our code, hence we opted to neglect them for the sake of simplicity. Note that, in the case of anisotropic $\mathbf{g}_{Ce}$, the relative orientation of $\mathbf{g}_{Er,1}$ and $\mathbf{g}_{Ce}$ is unknown and can only be determined by single crystal measurements. Although these experiments would help to precisely conclude the experimental characterization of the sample, they do not change our conclusions on the use of this molecule as a QEC unit.

In summary, the model describing the trimer that we used for simulations implementing the TQC is the one in Eq. 3.6. The three g-tensors we determined are:

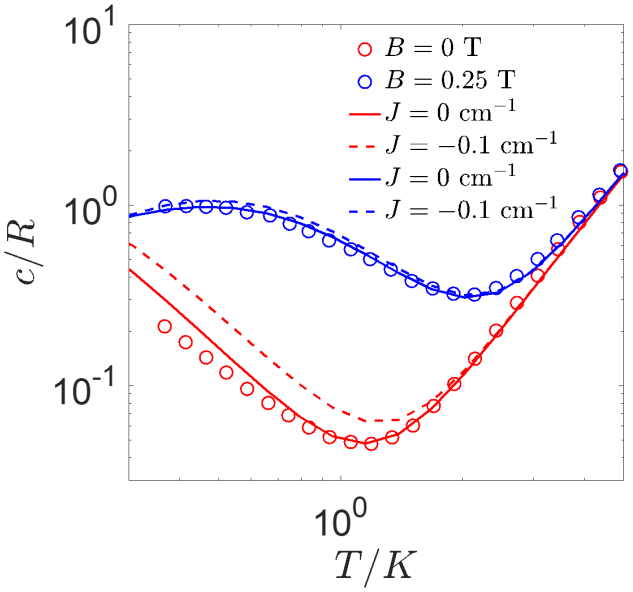

Figure 3.8: Low-field specific heat vs. T on **1**: simulated without (continuous line) or with (dashed line) a ferromagnetic isotropic exchange contribution $J = -0.1\text{cm}^{-1}$. Reproduced from Ref. [60] with permission from the Royal Society of Chemistry.

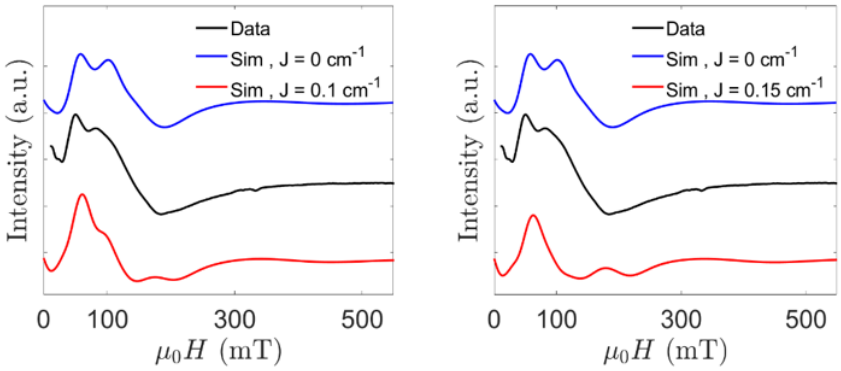

Figure 3.9: Cw-EPR spectra (black lines) on **1**, simulated with (red lines) or without (blue lines) an anti-ferromagnetic isotropic exchange contribution $J = 0.1\text{cm}^{-1}$ (left) or $J = 0.15\text{cm}^{-1}$ (right). Reproduced from Ref. [60] with permission from the Royal Society of Chemistry.

$$\mathbf{g}_{Er,1} = \begin{pmatrix} 1 & 0 & 0 \\ 0 & 5 & 0 \\ 0 & 0 & 11.5 \end{pmatrix}, \mathbf{g}_{Ce} = \begin{pmatrix} 1.85 & 0 & 0 \\ 0 & 1.85 & 0 \\ 0 & 0 & 1.85 \end{pmatrix}$$
$$\mathbf{g}_{Er,2} = \begin{pmatrix} 1.0203 & 0.3242 & 0.1569 \\ 0.3242 & 6.1572 & 2.4987 \\ 0.1569 & 2.4987 & 10.3212 \end{pmatrix} \tag{3.7}$$

We recall that $g_{Er,2}$ is obtained from $g_{Er,1}$ by a rotation. We used these g-factors to calculate $\mathbf{J}_{1,2}$, $\mathbf{J}_{2,3}$ and $\mathbf{J}_{1,3}$ with Eq. 1.5 since we did not add any additional exchange coupling. The resulting magnetic interaction is:

$$\mathbf{J}_{1,2} = \begin{pmatrix} 0.0129 & 0.0000 & 0.0016 \\ 0.0016 & 0.0581 & -0.0347 \\ 0.0161 & -0.0799 & -0.2823 \end{pmatrix} \text{cm}^{-1}$$
$$\mathbf{J}_{2,3} = \begin{pmatrix} 0.0137 & 0.0105 & 0.0186 \\ 0.0024 & 0.0363 & -0.0815 \\ -0.0056 & -0.1202 & -0.2621 \end{pmatrix} \text{cm}^{-1} \tag{3.8}$$
$$\mathbf{J}_{1,3} = \begin{pmatrix} 0.0008 & 0.0008 & -0.0040 \\ 0.0008 & 0.0153 & -0.0879 \\ 0.0016 & -0.0210 & -0.2081 \end{pmatrix} \text{cm}^{-1}$$

3.1.4 Pulsed EPR experiments on [ErCeEr]

The aim of these experiments was that of measuring the decoherence time T_2 on **1**, giving us a reasonable guess for the performance of this molecule as an error-protected unit. The amplitude of the spin echo (ESE) as a function of magnetic field was recorded using a Hahn echo pulse sequence ($\pi/2 - \tau - \pi - \tau -$ echo) for a fixed pulse separation $\tau = 120$ns (Fig. 3.10, top left panel). A direct comparison between the derivative of the ESE spectrum and the cw-EPR spectrum is not an easy task, mainly due to the modulation of the ESE signal associated to the coupling to nuclear spins, more relevant at short times and low magnetic fields. The decays with τ of the ESE signals show a non-exponential dependence (Fig. 3.10, right panel), likely associated with the still non-negligible influence of inter-molecule dipolar couplings, thus of spin diffusion phenomena, in a relatively concentrated solution. Fits to a double exponential decay, with two components of comparable amplitudes but different T_2, provide a reasonably good account of these data. The data reported in Fig. 3.10, (bottom left panel), with $T_2 \approx 0.5\mu$s and nearly independent of magnetic field, correspond to the slower decaying component, which eventually determines the characteristic time for which coherence vanishes at each field[29].

It is important to note that longer (and better) coherence times could be obtained by chemically optimizing these samples. In fact, inter-molecule dipolar coupling and nuclear spins fluctuations surrounding the magnetic ions are the most relevant decoherence sources in this system. Performing experiments on frozen solutions using a deuterated solvent should reduce the effect of coupling to H nuclei

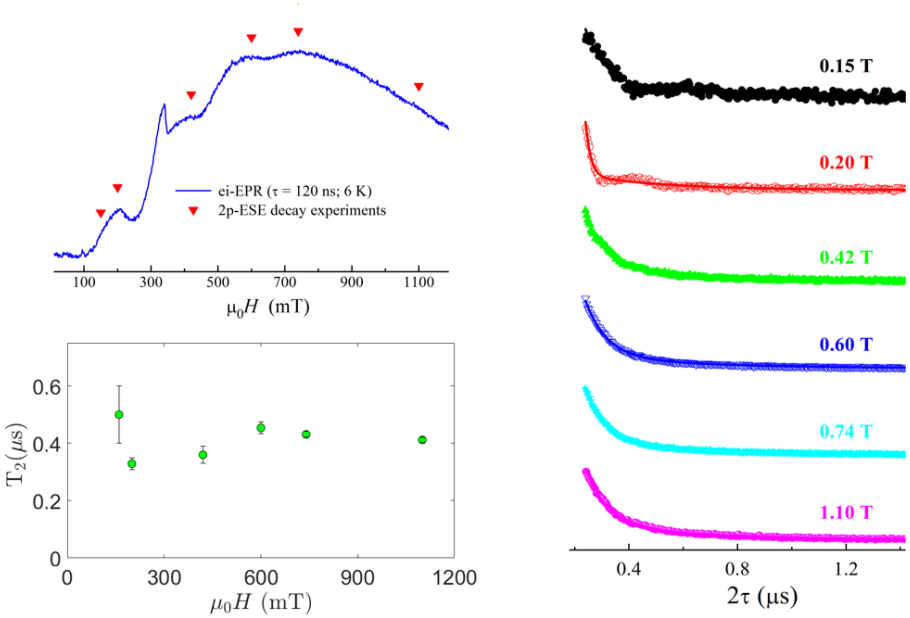

Figure 3.10: Top left: echo-induced EPR spectrum on **1** at $T = 6$K; red triangles indicate the magnetic field values at which τ dependence was measured through two-pulse experiments. Right: decay of the ESE measured with a two-pulse sequence ($\pi/2 - \tau - \pi -$ ESE) at the magnetic fields shown in labels; solid lines are least-squares fits to the sum of two exponential decays. Bottom left: phase memory time T_2 at various magnetic fields obtained from the slower decaying exponential used to fit the curves in the right panel. Reproduced from Ref. [60] with permission from the Royal Society of Chemistry.

in the solvent, significantly improving T_2, especially at low temperature[65]. Along the same line, deuteration of the ligand cage of the rare-earth ions would effectively eliminate the coupling to protons, leading to even longer T_2 values. Additionally, the aforementioned effect of inter-molecule interaction could be weakened by reducing the concentrations, which were kept relatively high for signal measurements purposes.

3.2 The QEC code

Since in MNMs the most common source of decoherence is pure dephasing, we chose to study the efficiency of the TQC in which the encoded state is protected from phase-flip errors, which are the direct effect of pure dephasing on a qubit. The circuit we considered is shown in figure 3.11.

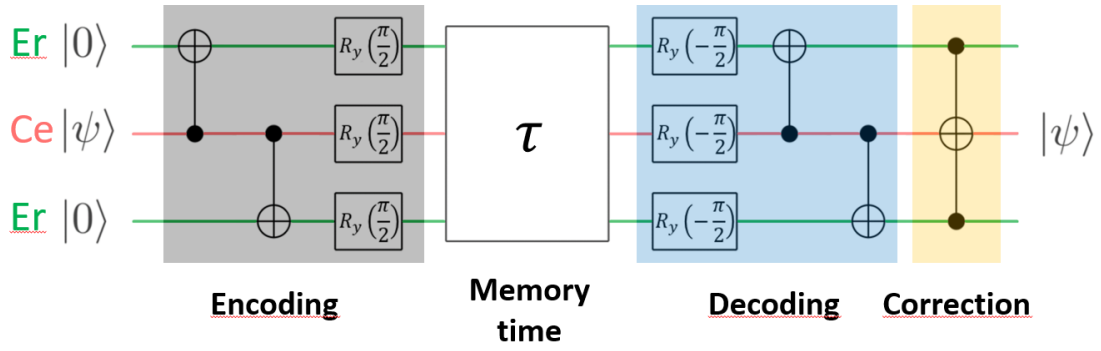

Figure 3.11: Quantum computing circuit describing the version of the TQC implemented in this work, which corrects a single phase-flip error on the central qubit. The encoding step is composed of two CNOT gates (both with the central qubit as control qubit) and three qubit rotations $R_y(\pi/2)$, one for each qubit. After memory time τ the decoding step consists in three $R_y(-\pi/2)$ rotations followed by the same CNOT gates found during encoding. Correction is achieved via a Toffoli gate, in which the central qubit acts as target. Reproduced from Ref. [60] with permission from the Royal Society of Chemistry.

This QEC code is aimed at correcting a single phase-flip error on the central qubit (Ce), which is the unit carrying the logical information and is initialized in a generic state $|\psi\rangle = \alpha|0\rangle + \beta|1\rangle$. The other two qubits are instead initialized in $|0\rangle$.

The first step of the code is the *encoding*: two CNOT gates followed by a rotation on each qubit bring the three-qubit state $|\overline{\psi}\rangle$ to an encoded state, which protects the information from a phase error. The two CNOT gates both have the central qubit as control, while targeting each one a different qubit. Their action brings the three-qubit state to $|\overline{\psi}\rangle = \alpha|000\rangle + \beta|111\rangle$. The three $R_y(\pi/2)$ rotations (see Eq. 2.6) are used in place of the three Hadamard gates which should be implemented in the phase-flip TQC (see Section 2.3.2). This choice is made since in the proposed implementation a Hadamard gate would require an additional $R_x(\pi)$ rotation, overall taking three times longer to perform. A simpler

(and faster) $R_y(\pi/2)$ rotation still works fine in this case, provided that after the error we apply a $R_y(-\pi/2)$ rotation, obtaining only an overall phase on the three-qubit state with respect to the code using Hadamard gates. The encoded state is then stored for a *memory time* τ, during which it is supposed to be subject to environmental pure dephasing. Afterwards, the decoding step is composed of the three aforementioned $R_y(-\pi/2)$ and two CNOT gates perfectly analogous to those of the encoding step. Note that the effect of the $R_y(\pm\pi/2)$ rotations is that of transforming σ_x errors into σ_z errors, since $R_y(\pi/2)\sigma_x R_y(-\pi/2) = \sigma_z$. Hence, after decoding, any single phase-flip error on one qubit is converted into a bit-flip on the same qubit, obtaining one of the four possible three-qubit states:

$$\begin{aligned}
\text{no error:} \quad & |\overline{\psi}\rangle = \alpha\,|000\rangle + \beta\,|010\rangle = |0\rangle \otimes (\alpha\,|0\rangle + \beta\,|1\rangle) \otimes |0\rangle \\
\text{phase-flip on qubit 1:} \quad & |\overline{\psi}\rangle = \alpha\,|100\rangle + \beta\,|110\rangle = |1\rangle \otimes (\alpha\,|0\rangle + \beta\,|1\rangle) \otimes |0\rangle \\
\text{phase-flip on qubit 2:} \quad & |\overline{\psi}\rangle = \alpha\,|111\rangle + \beta\,|101\rangle = |1\rangle \otimes (\alpha\,|1\rangle + \beta\,|0\rangle) \otimes |1\rangle \\
\text{phase-flip on qubit 3:} \quad & |\overline{\psi}\rangle = \alpha\,|001\rangle + \beta\,|011\rangle = |0\rangle \otimes (\alpha\,|0\rangle + \beta\,|1\rangle) \otimes |1\rangle
\end{aligned} \tag{3.9}$$

Differently from the general description provided in Section 2.3.2, here error correction is implemented via a Toffoli gate, with the central qubit (Ce) as target and the other two (Er) as control, effectively switching the two states $|111\rangle$ and $|101\rangle$. This allows us to correct the state of the central qubit without using ancillae for error detection. It is immediate to see that this gate has effect only in the case in which the phase-flip error happened on the central qubit, bringing its state to $|\overline{\psi}\rangle = \alpha\,|101\rangle + \beta\,|111\rangle = \alpha\,|111\rangle + \beta\,|101\rangle = |1\rangle \otimes (\alpha\,|0\rangle + \beta\,|1\rangle) \otimes |1\rangle$. Note that in this corrected state and in all the other unaffected states in 3.9 the superposition $|\psi\rangle = \alpha\,|0\rangle + \beta\,|1\rangle$ is preserved for the central qubit, and its state is perfectly factorized from that of the other two qubits.

3.3 Implementing the phase-flip TQC

The manipulation of quantum states necessary to implement quantum gates is achieved through Gaussian-shaped micro-wave pulses resonant with targeted transitions. An important requirement for this kind of manipulation to be possible is that each transition must be individually addressable. This is made possible by the dipolar couplings that we found in this molecule, which make the transition energy of each qubit dependent on the state of the other two qubits. Note that Er-Er interaction is not strictly needed for this implementation, but it nonetheless helps by further improving spectral resolutions of some transitions. Having well-distinguishable transition energies means that the Toffoli gate can be implemented by a *single* pulse resonant with the $|101\rangle \leftrightarrow |111\rangle$ (see the correction step in Figure 3.12), given that its action is conditioned by the states of both the external qubits. On the other hand, two-qubit CNOT gates must be done regardless of the state of the other qubit, hence each one of them is implemented via *two* pulses (see the decoding step in Figure 3.12). Lastly, single-qubit rotations all require *four* different pulses (see the decoding step in Figure 3.12), one for each possible state of the other two qubits. However, being well separated in energy, these four pulses can be sent at the same time, hence not causing a slowdown of the QEC code at all.

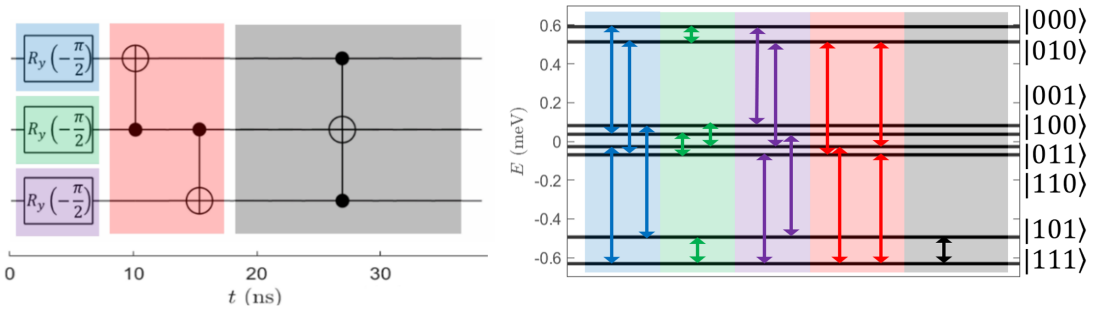

Figure 3.12: Left panel: decoding and correction blocks of the TQC highlighting the approximate duration of each set of gates. The three $R_y(-\pi/2)$ gates are performed in parallel with an overall duration of 8 ns (shaded areas with different colours refer to different qubits); the two CNOT gates are performed in sequence with a total duration of 11.2 ns (red shaded area); the Toffoli gate is by far the longest one, with a duration of 16.1 ns (grey shaded area). Right panel: scheme of the transitions that we need to excite performing each gate (energies calculated with a 1T static field along z), with the colour code being the same as in the left panel for better readability. Reproduced from Ref. [60] with permission from the Royal Society of Chemistry.

Very good factorization of the states, fundamental in the definition of the computational basis, is obtained via a static field of 1T applied along the z direction, as shown in Figure 3.13. As a matter of fact, an important aspect that we need to take into account at this point is that the computational basis on which we work must consist of direct product states. This is mandatory, since the QEC code we introduced is only able to correctly detect *independent* errors and a basis composed of entangled states would instead introduce correlated errors. In our case, this condition is met as the transverse component of the magnetic interaction between the ions is not big enough ($J_\perp \lesssim 0.3\text{cm}^{-1}$) to induce mixing between the basis states (see Figure 3.13).

The micro-wave pulses are sent via an oscillating field $B_1 = 50\text{G}$ along the y axis, that is the direction in which we find the intermediate value of $\mathbf{g}_{Er,1}$ and $\mathbf{g}_{Er,2}$, ensuring short transition times.

3.4 Simulating the QEC code

Simulations implementing the proposed QEC code on **1** have been performed by numerically integrating the Liouville-von Neumann equation of motion for the system density matrix ρ[66]:

$$\dot{\rho} = -i[H_0 + H_1, \rho] + \sum_i \frac{2}{T_{2,i}} \left(S_i^z \rho S_i^z - \frac{\rho}{4} \right) \tag{3.10}$$

where H_0 is the static spin Hamiltonian (Eq. 3.6), H_1 is the time-dependant spin Hamiltonian including all of the gaussian-shaped pulses, and $T_{2,i}$ is the phase memory time of the i-th qubit. The first term simulates the coherent evolution associated to the spin Hamiltonian, whereas the second term models pure dephasing. In

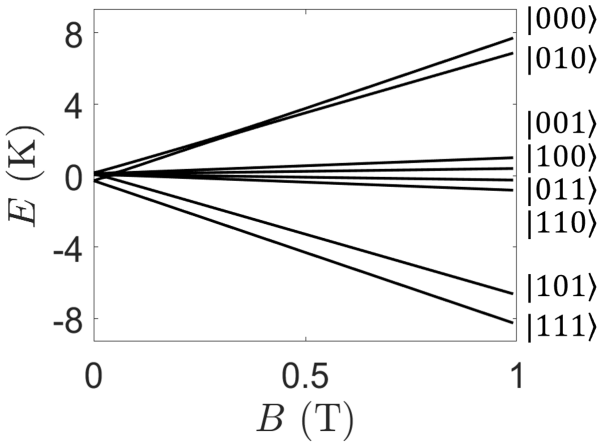

$S_{z,Er}$	$S_{z,Ce}$	$S_{z,Er}$
−0.5000	−0.4989	−0.4851
−0.5000	0.4989	−0.4858
−0.4998	−0.4993	0.4849
0.4998	−0.4993	−0.4857
−0.4998	0.4993	0.4857
0.4999	0.4993	−0.4867
0.5000	−0.4959	0.4858
0.5000	0.4959	0.4869

Figure 3.13: Left: static field dependency of the energy levels, labelled on the right in the order in which the states are found at 1T. Reproduced from Ref. [60] with permission from the Royal Society of Chemistry. Right: $\langle j|S_{z,i}|j\rangle$ computed for each ion on all basis states $|j\rangle$; note the good approximation of this basis with direct product states.

all simulations, the central qubit was initialized in the state $|\psi\rangle = (|0\rangle + i\,|1\rangle)/\sqrt{2}$, which is the most susceptible to pure dephasing (see next section), and the other two qubits were both initialized in $|0\rangle$. The efficiency of the error recovery procedure was quantified by computing the error probability

$$\mathcal{E} = 1 - \langle\psi|\rho_{\mathrm{Ce}}|\psi\rangle \tag{3.11}$$

where ρ_{Ce} is the density matrix reduced on the second qubit and $|\psi\rangle$ the initial error-free logical state. This quantity is a measure of the distance between the Ce^{3+} qubit state after QEC and the logical state $|\psi\rangle$ we want to preserve, hence a small value of $\mathcal{E}$ corresponds to a good recovery. Another quantity we used to gain further insights on the performance of the code is the ratio

$$\mathcal{R} = \mathcal{E}_U/\mathcal{E}_C \tag{3.12}$$

where $\mathcal{E}_C$ is simply the error probability after QEC and $\mathcal{E}_U$ is the error probability computed on an uncorrected isolated qubit undergoing pure dephasing. We refer to $\mathcal{R}$ as *gain*, since it indicates an advantage of the QEC procedure when $\mathcal{R} > 1$ and higher values correspond to better performances.

3.4.1 Testing the pulse sequence

As a first step, we checked the performance of our proposed pulse sequence simulating only the coherent evolution of the system (first term in Eq. 3.10), introducing an instantaneous phase-flip error between encoding and decoding on one of the three qubits or none of them. In all four cases we correctly recovered the logical state on the central qubit, as we can see from Figure 3.14. Here, we plot the diagonal element of ρ for each state as a function of time, evidencing the action of the

pulse sequence and the effectiveness of the code. Coloured panels showcase how the final states in all four cases represent the $\alpha|0\rangle + \beta|1\rangle$ superposition that we want to preserve.

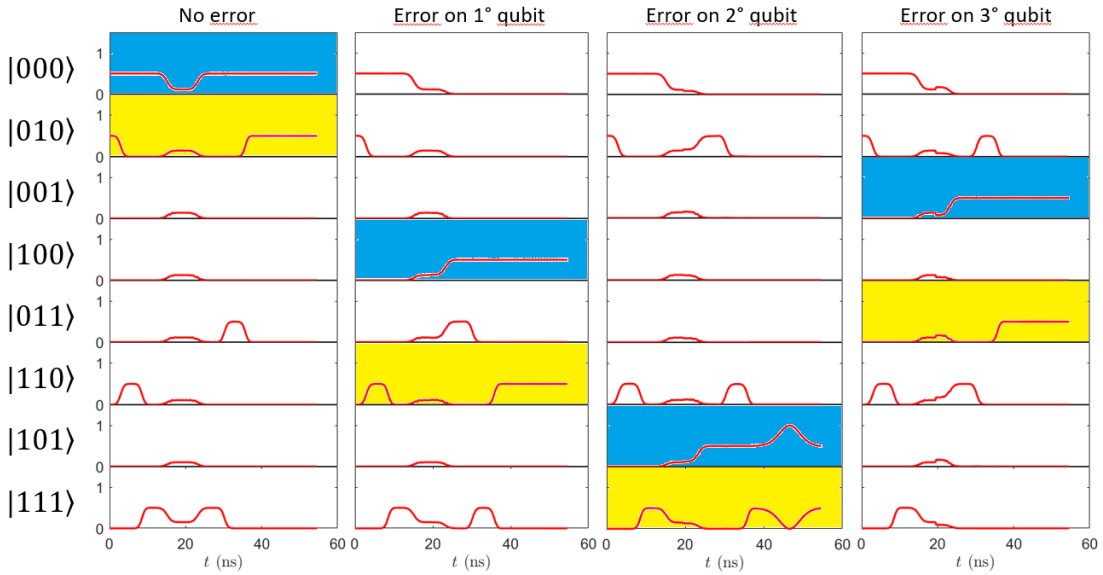

Figure 3.14: Populations of each state as a function of time. From left to right: no error is introduced after encoding; S_z error on the first qubit; S_z error on the second qubit; S_z error on the third qubit. Blue (yellow) panels represent final states with the central qubit in $|0\rangle$ ($|1\rangle$).

A more realistic error implementation allows us to see how our proposed scheme performs on a mixture state. This is modelled considering a phase-flip error that happens instantaneously after encoding on any one of the three qubits with probability p. The expected error probability after QEC can be analytically computed as a function on p in an ideal implementation of the code[48], starting from the density matrix mixture after the error:

$$\begin{aligned}\rho_{err} = &(1-3p(1-p)^2-3p^2(1-p)-p^3)\rho+\\ &+p(1-p)^2\sum_{i=1}^{3}\sigma_{z,i}\rho\sigma_{z,i}+\\ &+p^2(1-p)\sum_{\substack{i,j=1\\ i\neq j}}^{3}\sigma_{z,i}\sigma_{z,j}\rho\sigma_{z,i}\sigma_{z,j}+\\ &+p^3\sigma_{z,1}\sigma_{z,2}\sigma_{z,3}\rho\sigma_{z,1}\sigma_{z,2}\sigma_{z,3}\end{aligned} \tag{3.13}$$

where $\rho = |\overline{\psi}\rangle\langle\overline{\psi}|$ and $|\overline{\psi}\rangle$ is the three-qubit state after encoding. ρ_{err} is a mixture of four terms, each one with its probability: the first describes the "no error" case, the second describes all three possible single-qubit phase-flips, the third describes all three possible two-qubit phase-flips and the fourth is the three-qubit phase flip. The error detection and correction procedure has a different effect when applied to

each one of these terms. In the first term it leaves intact the logical superposition on the central qubit. In the second term it restores the superposition in the case in which the error happened on the central qubit, otherwise it is left in the correct state. In the third and fourth term it always gives the wrong superposition $\alpha|1\rangle + \beta|0\rangle$ on the central qubit. Hence, the reduced density matrix on the Ce^{3+} ion after correction can be written as

$$\rho_{\mathrm{Ce}} = (1 - 3p^2(1-p) - p^3)\rho_{\mathrm{Ce},corr} + (3p^2(1-p) + p^3)\rho_{\mathrm{Ce},err} \tag{3.14}$$

where $\rho_{\mathrm{Ce},corr} = |\psi\rangle\langle\psi|$, with $|\psi\rangle$ being the correct logical state and $\rho_{\mathrm{Ce},err} = |\psi\rangle_{err}\langle\psi|_{err}$, with $|\psi\rangle_{err} = \alpha|1\rangle + \beta|0\rangle$. If we now calculate the error probability $\mathcal{E}$ with equation 3.11 we obtain

$$\mathcal{E} = \left(3p^2(1-p) + p^3\right)\left[1 - 4|\mathrm{Re}(\alpha^*\beta)|^2\right] \tag{3.15}$$

where we exploited the fact that $\langle\psi|\rho_{\mathrm{Ce},corr}|\psi\rangle = 1$ and $\langle\psi|\rho_{\mathrm{Ce},err}|\psi\rangle = |\alpha\beta^* + \alpha^*\beta|^2 = 4|\mathrm{Re}(\alpha^*\beta)|^2$. Note that for a given p the maximum of $\mathcal{E}$ is obtained when $\alpha^*\beta$ is purely imaginary, hence the logical state $|\psi\rangle = (|0\rangle + i|1\rangle)/\sqrt{2}$ leads to the highest error probability after correction, as stated before. We then performed numerical simulations in this ideal case as a function of p in order to compare our result with this analytical expression for the error probability, with our results shown in Figure 3.15. In this figure we immediately note how our simulations (blue circles) are really close to the ideal performance of the QEC code (black line). This means that the pulse sequence we designed correctly implements the desired code. Moreover, we compared the computed $\mathcal{E}$ with that of an uncorrected isolated qubit prepared in $|\psi\rangle$ undergoing a phase-flip error with probability p, noticing a relevant gain in our recovery of the correct logical state.

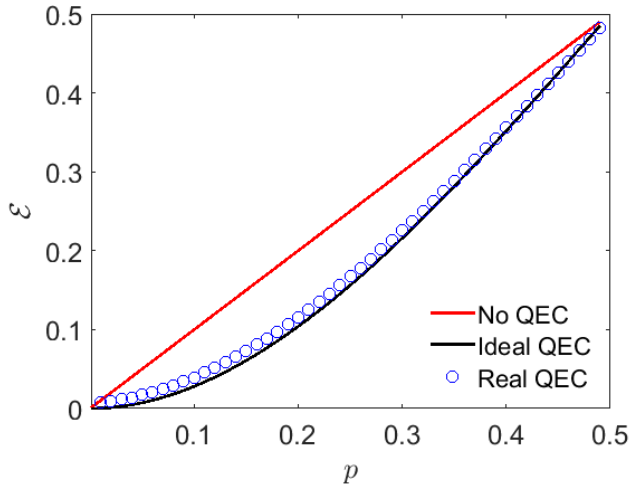

Figure 3.15: Simulated $\mathcal{E}$ after implementation of the QEC code as a function of the probability p of a phase-flip error occurring on any of the three qubits immediately after encoding. Simulations (blue circles) are compared to the ideal performance of the TQC (black line) and with an isolated qubit on which no QEC has been applied (red line). Reproduced from Ref. [60] with permission from the Royal Society of Chemistry.

3.4.2 Simulations with pure dephasing

After having confirmed the effectiveness of the pulse sequence in implementing the QEC code, we proceeded to perform simulations including pure dephasing effect, that is the second term in Eq. 3.10. We considered various T_2 values in order to get a better understanding of our code performance under various conditions, using for simplicity the same T_2 for each ion in all simulations. A parameter of great importance in these simulations is the *memory time* τ during which the encoded state is only subject to pure dephasing, without additional external manipulation. The effect of pure dephasing on the encoded state is that of creating a ρ_{err} analogous to that in Eq. 3.13, where we obtain its dependency on τ by substituting $p = (1 - e^{-\tau/T_2})/2$[48]. On this state we reasonably expect the designed pulse sequence to work correctly as it was in the case of instantaneous phase-flip errors. However, the main difference with the previous case is that now pure dephasing introduces errors also during encoding, decoding and correction steps, whose realistic durations are not negligible compared to the phase memory time. The results for $\mathcal{E}$ and $\mathcal{R}$ are reported in Figure 3.16 for seven different values of T_2 and compared to the effect of pure dephasing on an isolated qubit.

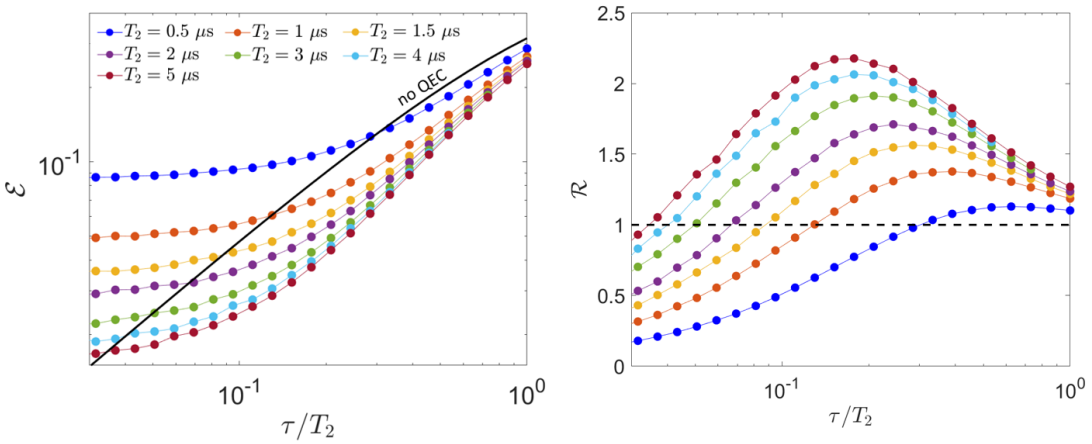

Figure 3.16: Left: final error $\mathcal{E}$ as a function of memory time τ in units of T_2 for seven different values of T_2. Solid black line represents $\mathcal{E}$ for an isolated qubit undergoing pure dephasing. Right: gain $\mathcal{R}$ after correction as a function of memory time τ/T_2. Reproduced from Ref. [60] with permission from the Royal Society of Chemistry.

Note that by varying T_2 the error on the isolated qubit does not change when plotted against τ/T_2, that is because it can be analytically computed as:

$$\mathcal{E}_U = 2|\alpha|^2|\beta|^2\left(1 - e^{-\tau/T_2}\right) \tag{3.16}$$

where its dependence on T_2 appears only through the ratio τ/T_2. The same is not true for the results of our simulations: shorter T_2 times are associated to higher-error plateaus at low τ/T_2 values. This is the disruptive effect of pure dephasing during pulse sequences, in fact errors that occur during this steps are not correctable with the TQC code, thus introducing a deviation from the ideal case that depends only from the duration of the pulse sequences with respect to

T_2. At higher τ/T_2 all simulated curves converge to one another: that is the ideal performance of the code. This happens because the uncorrectable errors introduced during pulse sequences become negligible compared to two- and three-qubit errors that are more likely to happen at longer memory times.

The gain $\mathcal{R}$, shown in the right panel of Figure 3.16, is useful in understanding the performance of our procedure. For a given T_2 each $\mathcal{R}$ shows a maximum $\tilde{\mathcal{R}}$ at $\tilde{\tau}$, which we identified as the *optimal working point* for this QEC code, where the most gain is obtained by its implementation. Quite obviously, higher $\tilde{\mathcal{R}}$ correspond to better performances, but it is nonetheless important to take into account the value of $\mathcal{E}$ at $\tilde{\tau}/T_2$, since $\mathcal{R}$ does not give any information on the final error probability. The value of $\tilde{\tau}$ is also really useful: since QEC codes are meant to be repeated after a fixed memory time, $\tilde{\tau}$ represents a good choice given the higher gain. Thus, a long $\tilde{\tau}$ is important since it is related to a greater number of operations that can be performed before repeating the error correction. Our simulations display an overall good performance, since even with a $T_2 \approx 3$ μs we have $\tilde{\mathcal{R}} \approx 2$, which means that the error is halved by our procedure, and $\tilde{\tau} \approx 700$ ns, during which it is possible to implement up to $50 - 100$ gates. However, even at shorter T_2 we always find a τ after which it is advantageous to implement the QEC code with respect to the uncorrected qubit case.

3.4.3 Performance in less optimal experimental conditions

The performance of our proposed implementation was also simulated in less optimal experimental condition, testing the robustness of the scheme. In particular, we considered a lower ($B = 0.5$ T) and slightly tilted ($\theta = 5°$) static field, causing a weaker factorization of the basis states. Nevertheless, as we can see from Figure 3.17, the performance of our code is only slightly worsened when compared to the previous case ($B = 1$T, $\theta = 0°$).

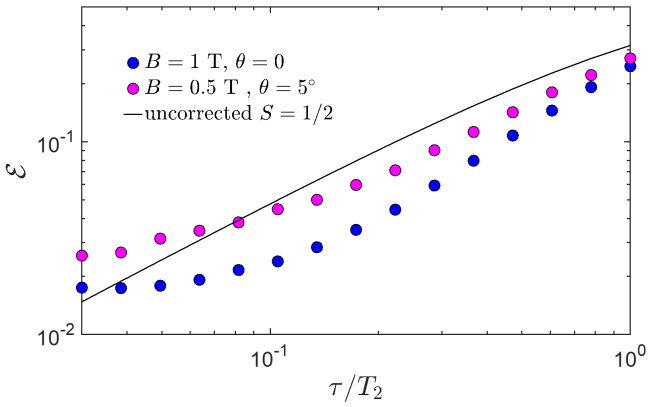

Figure 3.17: Simulation (with $T_2 = 5\mu$s) of the final error $\mathcal{E}$ as a function of τ/T_2 with a smaller ($B = 0.5$T) and slightly tilted ($\theta = 5°$) external field (pink circles), compared with the $B = 1$T, $\theta = 0°$ case reported in the text (blue circles). Reproduced from Ref. [60] with permission from the Royal Society of Chemistry.

An approach we undertook in order to circumvent the uncorrectable errors caused by pure dephasing during gate implementation, especially relevant when

considering shorter T_2, is that of shortening the duration of the code. This is achieved by using a stronger oscillating field B_1, which in turn speeds up qubit manipulation time. In Figure 3.18 we report a comparison between $\mathcal{E}$ simulated with $T_2 = 0.5$ μs and two different oscillating fields: $B_1 = 50$ G (the same as in Figure 3.16, left panel) and $B_1 = 100$ G, which halves gate duration. The use of faster pulses clearly displays a big improvement in the performance of the code, whose final error probability is close to that of the $T_2 = 1$ μs and $B_1 = 50$ G simulation (also reported in Figure 3.18). It is natural to expect that these last two cases should have the exact same performance, since the initial error plateau depends on the ratio between code implementation time and T_2, both changed by a factor 2. However, the slightly worse performance of the $B_1 = 100$ G case is due to the fact that shorter pulses are broader in energy, hence leakage is more likely to happen during certain transitions.

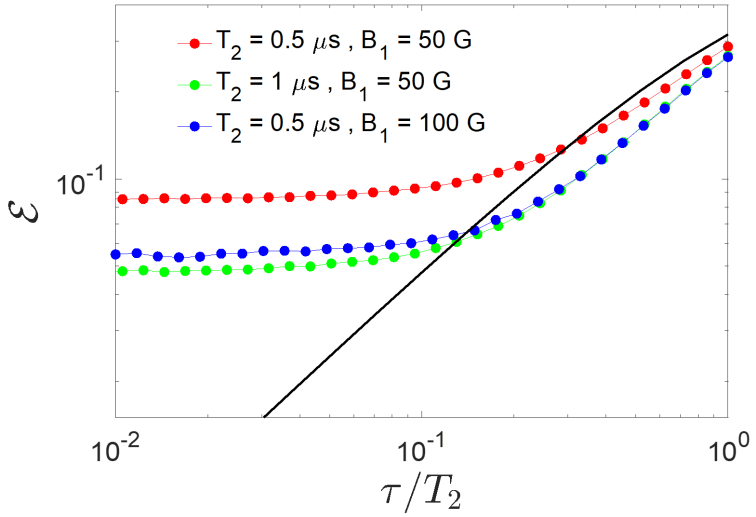

Figure 3.18: Simulation of the final error $\mathcal{E}$ as a function of τ/T_2 comparing the decrease of T_2 with the increase of the oscillating field amplitude B_1. $T_2 = 0.5$ μs for red and blue points, $T_2 = 1$ μs for green points. $B_1 = 50$ G for red and green points, $B_1 = 100$ G for blue points. Reproduced from Ref. [60] with permission from the Royal Society of Chemistry.

3.5 Conclusion and perspectives

In summary, we fully characterized three rare-earth ions of a molecular [Er-Ce-Er] trimer, thanks to properly synthesized [Er-La-Er] and [Lu-Ce-Lu] analogues, obtaining highly anisotropic g-factors and weak magnetic interactions. These Hamiltonian parameters fulfil the requirements to implement the three-qubit phase flip code within a single molecule, encoding quantum information in three qubits (each ion acts a physical qubit) within the same molecule and protecting it from pure dephasing. We performed numerical simulations, obtaining a good performance of the QEC code using experimentally-determined parameters and demonstrating

that this trimer can effectively encode an error-protected qubit. It is important to point out how an experimental test of the proposed QEC scheme would require a diluted single crystal, exploiting the co-alignment of all molecules. Single crystal measurements would also be valuable in obtaining an even more precise determination of the directions of all g-factors. We also note how several improvements can be made in this system: longer dephasing times T_2, pulse sequence design and tailored molecule synthesis can all lead to even better performances.

This work, together with the one exposed in next chapter, represents the first proposal for using a MNM as a single unit embedding a quantum error-corrected qubit. The possibility of enabling QEC within a single physical unit allows much easier implementation of codes, without the major hurdle of having to perform quantum gates between a large number of physical objects. Moreover, the single molecule nature of our approach is a key element towards the realization of a scalable quantum processor. Here we utilized a standard QEC code which suited the molecular trimer, but specific QEC schemes can be derived for specific energy level structures. In this regard, molecule synthesis and QEC code design are mutually fundamental in future improvements of such implementations.

Chapter 4

A Molecular Nanomagnet Encoding a Qubit with Embedded Quantum Error Correction

A. Chiesa, E. Macaluso, F. Petiziol, S. Wimberger, P. Santini and S. Carretta, Molecular Nanomagnets as Qubits with Embedded Quantum-Error Correction, *The Journal of Physical Chemistry Letters*, **11**, 20, 8610–8615, 2020

The work presented in this chapter shows how multiple low-energy states accessible in MNMs can be exploited to encode an error-protected qubit within a single molecule. As shown in chapters 2 and 3 the standard approach for QEC theory is that of encoding a single logical qubit in multiple levels, obtained by combining many physical qubits. Nevertheless, manipulation of the states in such systems can be difficult, given the potentially large numbers of physical units on which to operate both locally and non-locally. Here we propose to use a single multi-level quantum object to encode a logical unit. In this regard, a possibility would be to implement standard QEC codes on a single n-level unit, as an example by mapping the 2^3 levels of the TQC to an 8-level molecule[67]. However, this strategy does not properly work because real errors in these systems do not directly correspond to single-qubit errors on the encoded states that the QEC procedure is built to correct. Hence, we derived a QEC procedure tailor-made for this class of molecules and aimed at correcting dephasing errors (as in Chapter 3), the most common source of errors in MNMs. We also designed the magnetic pulse sequence that implements this code on a generic spin S system and simulated its performance in a wide variety of cases. Additionally, we simulated the performance of the minimal $S = 3/2$ case using the nuclear spin levels on an existing molecule.

4.1 Dephasing of spin S MNMs

The prototypical system that we investigated in this work can be described with the following Hamiltonian:

$$H = g\mu B S_z + g^A \mu_B B \sigma_z^A + D S_z^2 + \mathbf{S} \cdot \mathbf{\Gamma} \cdot \boldsymbol{\sigma}^A \tag{4.1}$$

where S is the $(2S+1)$-levels qudit spin, D its single spin anisotropy and $\sigma^A = 1/2$ an ancillary electronic spin used for error detection (*ancilla*), coupled to the qudit via the ancilla-qudit coupling $\mathbf{\Gamma}$. In this work we proposed two possible implementations that are described by this Hamiltonian: a nuclear spin S coupled to its electronic spin σ^A or a dimer where a (molecular) spin S weakly interacts with a spin σ^A. In the former case $\mu = \mu_N$ and $\mathbf{\Gamma}$ describes hyperfine interaction; in the latter case $\mu = \mu_B$ and $\mathbf{\Gamma}$ describes a weak exchange interaction. It is important to have $\Gamma_{x,y}$ values much smaller than S and σ^A excitation energies in order to obtain eigenstates which can be written as simple products of the eigenstates of S_z ($\{|m\rangle\}$) and of σ_z^A ($\{|\sigma\rangle\}$). This is because error detection is implemented through the measurement of the ancilla state, which is required to be performed without collapsing the qudit state.

The effect of pure dephasing on a multi-level spin S can be described by using the Lindblad formalism as:

$$\dot{\rho}(t) = \frac{2}{T_2}\left(S_z \rho(t) S_z + \frac{1}{2} S_z^2 \rho(t) + \frac{1}{2}\rho(t) S_z^2\right) \tag{4.2}$$

where $\rho(t)$ is the density operator of the qudit and T_2 its characteristic dephasing time. For small t/T_2 values we can perform a perturbative expansion of $\rho(t)$ using the *error operators* E_k:

$$\rho(t) = \sum_{k=0}^{\infty} E_k \rho(0) E_k^\dagger \quad , \quad E_k = \sqrt{\frac{(2t/T_2)^k}{k!}} e^{-S_z^2 t/T_2} S_z^k \tag{4.3}$$

If we want our QEC code to correct errors up to order $(t/T_2)^n$ in $\rho(t)$ we need it to be able to correct error operators E_k up to $k = n$. Inspired by bosonic binomial codes[68] we introduced the *code words* $\{|\overline{0}\rangle, |\overline{1}\rangle\}$. These code words are the logical qubit computational basis on which we need our information to be encoded in order for it to be protected from dephasing errors. They are defined as a linear combination of the S_z eigenstates $\{|m\rangle\}$ as:

$$\begin{aligned} |\overline{0}\rangle &= \frac{1}{\sqrt{2^{2S-1}}} \sum_{\substack{k=1 \\ k\text{odd}}}^{2S} \sqrt{\binom{2S}{k}} |k - S\rangle \\ |\overline{1}\rangle &= \frac{1}{\sqrt{2^{2S-1}}} \sum_{\substack{k=0 \\ k\text{even}}}^{2S} \sqrt{\binom{2S}{k}} |k - S\rangle \end{aligned} \tag{4.4}$$

The error operators E_k that can be corrected using these code words can be determined by requiring them to satisfy the Knill-Laflamme conditions[69]:

$$\begin{aligned}\langle\overline{0}|E_k^\dagger E_j|\overline{0}\rangle &= \langle\overline{1}|E_k^\dagger E_j|\overline{1}\rangle \\ \langle\overline{0}|E_k^\dagger E_j|\overline{1}\rangle &= 0\end{aligned} \tag{4.5}$$

which ensure that the code words $\{|\overline{0}\rangle, |\overline{1}\rangle\}$ are a valid choice for correcting the error operators E_k. The first condition implies that correctable errors E_k preserve the superposition $\alpha|\overline{0}\rangle + \beta|\overline{1}\rangle$, making it possible to exactly recover the correct state. The second condition ensures that the E_k brings the two code words to orthogonal subspaces, which are detectable from one another. One can verify that the code words in Equation 4.4 satisfy these two conditions for S_z^k with $0 \leq k \leq 2n$. Hence, perturbative order n needs at least a spin $S = n + \frac{1}{2}$ qudit. As an example a spin $S = 5/2$ qudit encoding the code words in Equation 4.4 protects from errors described by $k = 2$. Note that each perturbative order needs two more levels in the qudit, therefore an integer spin S_{int} will correct the same powers of S_z as the half-integer spin $S_{int} - 1/2$. Because of this, we only focused on half-integer spins in this work.

In order to implement these code words on qudits to correct S_z^k errors, we designed a pulse sequence that accounts for information encoding, error detection through measurement of the electronic ancilla and error correction. Let us go into more detail in regard of the QEC procedure in the following section, where we use an existing molecule to simulate the performance of the code in the minimal case of qudit spin $S = 3/2$.

4.2 Minimal implementation: S=3/2 qudit

If we choose a qudit spin $S = 3/2$ we are able to detect and correct only S_z errors, which however represent the leading contribution with $k \neq 0$ to the expansion of $\rho(t)$ for low t/T_2. In this case, the code words in Equation 4.4 can be explicitly written as:

$$\begin{aligned}|\overline{0}\rangle &= \frac{1}{2}\left(\sqrt{3}\,|-1/2\rangle + |3/2\rangle\right) \\ |\overline{1}\rangle &= \frac{1}{2}\left(|-3/2\rangle + \sqrt{3}\,|1/2\rangle\right)\end{aligned} \tag{4.6}$$

And we can see that an S_z error on these encoded states leads to:

$$\begin{aligned}|\overline{E_0}\rangle &= \frac{S_z|\overline{0}\rangle}{||S_z|\overline{0}\rangle||^2} = \frac{1}{2}\left(-|-1/2\rangle + \sqrt{3}\,|3/2\rangle\right) \\ |\overline{E_1}\rangle &= \frac{S_z|\overline{1}\rangle}{||S_z|\overline{1}\rangle||^2} = \frac{1}{2}\left(-\sqrt{3}\,|-3/2\rangle + |1/2\rangle\right)\end{aligned} \tag{4.7}$$

where both states have been renormalized after the error. Note that the two error states are orthogonal to each other and also to both the code words $\{|\overline{0}\rangle, |\overline{1}\rangle\}$, thus making the error detectable and correctable.

Error detection is performed through the use of a two-level ancilla. Initially the code words are defined within the subspace where the ancilla is in its $|\downarrow\rangle$ state. During error recovery the ancilla is excited to $|\uparrow\rangle$ only in presence of a S_z error (further details in the next section). This is realized by exciting the ancilla conditionally on the qudit state $|m\rangle$, which is made possible by the presence of the ancilla-qudit coupling Γ. By measuring the ancilla state we therefore collapse its state either in the $|\uparrow\rangle$ (error) or in the $|\downarrow\rangle$ (no-error) state and finally encode again the information in the code words $\{|\overline{0}\rangle, |\overline{1}\rangle\}$. This is possible since Knill-Laflamme conditions ensure us that the information carried by the superposition is not lost through this process and we know how it can be re-encoded from the measured state.

We performed simulations for this code, which is implemented through a carefully-designed pulse sequence, using Hamiltonian parameters reported in [70] for the compound $(PPh_4)_2[Cu(mnt)_2]$ (**1**). In this complex the spin qudit consists in a nuclear spin $I = 3/2$ (which in this case corresponds to the qudit spin S) coupled through hyperfine coupling $\Gamma = (118, 118, 500)$MHz to an electronic spin with $g_z^A = 2.09$. We assumed $D = 50$ MHz for the nuclear quadrupole term of the Hamiltonian, which is a reasonable value for a ^{63}Cu nucleus. A static field $B = 0.3$ T gives a good factorization of the states, which can be expressed as $|m\rangle\,|\sigma\rangle$ tensor products (see Figure 4.1). In [70] it is reported a $T_2^A \approx 10^{-1}$ms for the electronic ancilla, making it safe for us to assume a $T_2 \approx 1$ms for the nuclear qudit. In the next section we will go into details on how the pulse sequence was designed in order to implement our code on a $I = 3/2$ nuclear qudit.

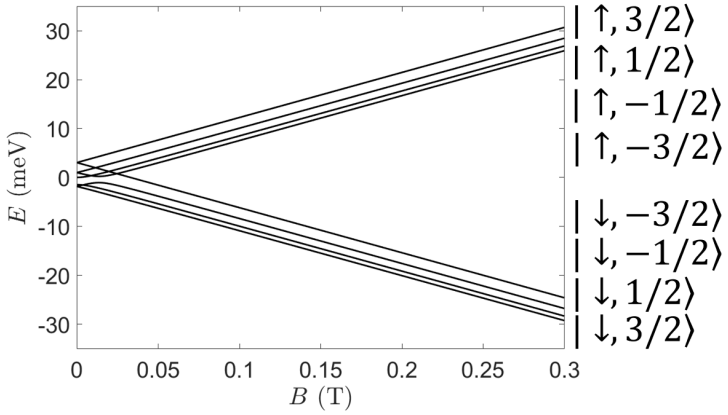

	σ_z^A	I_z
$\|\uparrow, 3/2\rangle$	0.5000	1.5000
$\|\uparrow, 1/2\rangle$	0.4997	0.5003
$\|\uparrow, -1/2\rangle$	0.4996	−0.4996
$\|\uparrow, -3/2\rangle$	0.4996	−1.4996
$\|\downarrow, -3/2\rangle$	−0.5000	−1.5000
$\|\downarrow, -1/2\rangle$	−0.4996	−0.5004
$\|\downarrow, 1/2\rangle$	−0.4996	0.4996
$\|\downarrow, 3/2\rangle$	−0.4997	1.4997

Figure 4.1: Left: static field dependency of the energy levels, labelled on the right in the order in which the states are found at 0.3T. Right: $\langle m, \sigma|\sigma_z^A|m, \sigma\rangle$ and $\langle m, \sigma|I_z|m, \sigma\rangle$ computed on basis states $|m, \sigma\rangle$; note the good approximation of this basis with direct product states.

4.2.1 Pulse sequence on a I=3/2 qudit

The pulse sequence implementing our QEC code on a $I = 3/2$ qudit is shown in its entirety in Figure 4.2, divided in three sections that we now describe in detail:

encoding, *detection* and *recovery*.

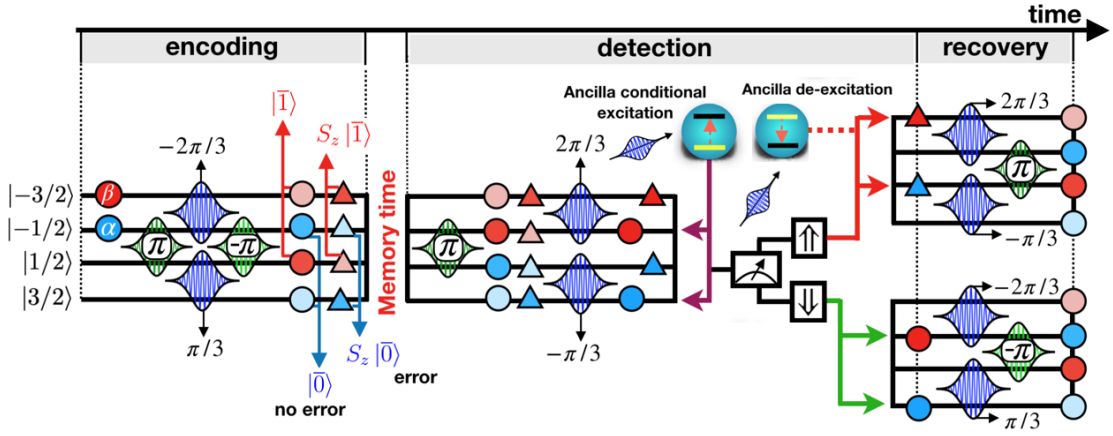

Figure 4.2: Visual representation of the pulse sequence designed to implement the QEC code on the $I = 3/2$ qudit. Horizontal lines represent the time evolution (from left to right) of the four eigenstates of the Hamiltonian in Eq. 4.1 with the ancilla in its non-excited state: $|m, \downarrow\rangle$. Gaussian-shaped peak functions placed between two levels represent magnetic pulses resonant with the associated $\Delta m = \pm 1$ transitions, with the rotation angle θ indicated. Blue (red) circles represent $|\overline{0}\rangle$ ($|\overline{1}\rangle$) states and blue (red) triangles represent $I_z|\overline{0}\rangle$ ($I_z|\overline{1}\rangle$) states. The colour intensity of circles and triangles is proportional to the modulus of the component. After the conditional excitation of the ancilla at the end of detection our procedure splits in two distinct path, depending on the result of ancilla measurement. Reprinted (adapted) with permission from [71]. Copyright (2020) American Chemical Society.

We initialize the system into the generic superposition:

$$\alpha|-1/2,\downarrow\rangle + \beta|-3/2,\downarrow\rangle \tag{4.8}$$

This state is then encoded in $\alpha|\overline{0}\rangle + \beta|\overline{1}\rangle$ through four resonant pulses, as shown in the first section of Figure 4.2. After encoding we have the *memory time* T, during which information is stored in the qudit. After this time, the density matrix ρ is in a mixture given by Eq. 4.3, whose main contributions at short T/T_2 comes from E_k operators with $k = 0$ (identity) and $k = 1$ (I_z). The error *detection* step requires us to be able to distinguish the correct state $\alpha|\overline{0}\rangle + \beta|\overline{1}\rangle$ from the erred state $\alpha|\overline{E_0}\rangle + \beta|\overline{E_1}\rangle$. This is achieved by performing three distinct steps. First, we use three magnetic pulses (second section of Figure 4.2), which act on the two possible states as:

$$\begin{aligned} \alpha|\overline{0}\rangle + \beta|\overline{1}\rangle &\rightarrow \alpha|3/2\rangle + \beta|-1/2\rangle \\ \alpha|\overline{E_0}\rangle + \beta|\overline{E_1}\rangle &\rightarrow \alpha|1/2\rangle + \beta|-3/2\rangle \end{aligned} \tag{4.9}$$

Note how in these two states the superposition containing the information is still preserved. Second, by applying two magnetic pulses resonant with the transitions $|-3/2,\downarrow\rangle \leftrightarrow |-3/2,\uparrow\rangle$ and $|1/2,\downarrow\rangle \leftrightarrow |1/2,\uparrow\rangle$ we are able to distinguish these two states, exciting the ancilla state only in presence of a I_z error. Third, we measure

the ancilla causing its state to collapse either in $|E_0\rangle = (\alpha\,|3/2\rangle + \beta\,|-1/2\rangle) \otimes |\downarrow\rangle$, meaning that no error is detected, or in $|E_1\rangle = (\alpha\,|1/2\rangle + \beta\,|-3/2\rangle) \otimes |\uparrow\rangle$, detecting a I_z error. After measurement the *recovery* process consists in rebuilding the encoded state starting from $|E_0\rangle$ (three pulses) or from $|E_1\rangle$ (four pulses). Note that this case is different from what described in Figure 4.6 for a general qudit spin S, where we start by exciting the ancilla in the $k = 0$ case. This is because we only need one ancilla excitation for the qudit spin $I = 3/2$, making the two cases almost identical, except for the de-excitation of the ancilla, associated to a longer recovery step. In fact we decided to excite the ancilla in the $k = 1$ case given the higher probability of measuring $k = 0$ at short times, slightly improving the performance of our code. The recovered state is then ready to be used in a new QEC cycle. At this point it is also important to point out how short is the time during which the ancilla is excited (evident from Figure 4.3), so that its shorter electronic T_2^A is not able to relevantly hinder the performance of the code.

4.2.2 Simulating the QEC code on a nuclear I=3/2 qudit

The implementation of this QEC code on compound **1** was simulated by numerically integrating the Liouville-Von Neumann equation of motion for the density matrix:

$$\dot{\rho} = -i[H_0 + H_1, \rho] + \frac{2}{T_2}\left(I_z \rho I_z + \frac{1}{2} I_z^2 \rho + \frac{1}{2}\rho I_z^2\right) + \frac{2}{T_2^A}\left(\sigma_z^A \rho \sigma_z^A + \frac{\rho}{4}\right) \qquad (4.10)$$

where H_0 is the static spin Hamiltonian (Eq. 4.1), H_1 is the time-dependant spin Hamiltonian including all magnetic pulses and the second an third terms model pure dephasing as in Eq. 4.2 for the qudit and the ancilla, respectively. Gaussian-shaped circularly polarized pulses with peak amplitude $B_1 = 50G$ and are sent in a direction orthogonal to that of the static field. We report in Figure 4.3 the time evolution of the populations of the 8 states of the system as a function of time in units of the elementary gating time $\tau = 6\hbar\sqrt{\pi/2}/g_\perp B_1$, which corresponds to a few times the duration of a π rotation. In this figure we separated the "no error" case (for which we did not show the states with the ancilla in $|\uparrow\rangle$, since it is never populated) from the I_z error case for the sake of clarity.

The performance of the code was quantified as a function of memory time T by analysing the final error probability $\mathcal{E}$ and the gain $\mathcal{R}$, which are defined as:

$$\mathcal{E} = 1 - \langle\psi|\rho_f|\psi\rangle\,, \mathcal{R} = \mathcal{E}_U/\mathcal{E} \qquad (4.11)$$

where $|\psi\rangle$ is the ideal encoded state that our code is aimed at preserving, ρ_f is the density matrix obtained after simulating the code and $\mathcal{E}_U$ is the final error probability of an uncorrected isolated qubit undergoing pure dephasing. Results for $\mathcal{E}$ and $\mathcal{R}$ are shown in Figure 4.4 as a function of T/T_2 (blue and red circles), compared to the same quantities calculated on a $S = 1/2$ qubit subject to pure dephasing. It is evident how our procedure overcomes the uncorrected spin $S = 1/2$ case after $T/T_2 \gtrapprox 10^{-2}$, reaching its maximum gain $\tilde{\mathcal{R}} \approx 2.5$ at $T = \tilde{T} = 0.06T_2$, which we defined as the *optimal working point* for this system. The initial plateau

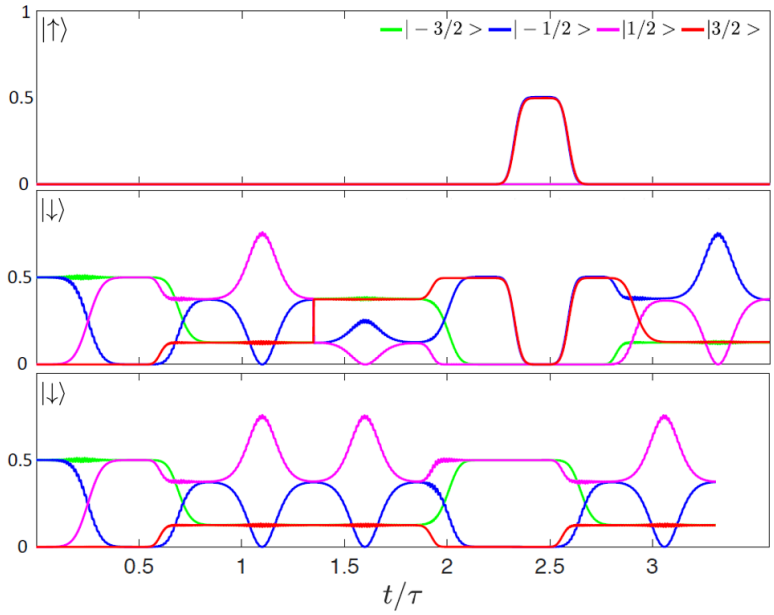

Figure 4.3: Diagonal elements of ρ as a function of t/τ. Bottom panel represents the states with the ancilla in $|\downarrow\rangle$ without any error acting on the system. Central panel represents the states with the ancilla in $|\downarrow\rangle$ with a I_z error acting on the system after encoding. Top panel represents the states with the ancilla in $|\uparrow\rangle$ with a I_z error acting on the system after encoding. In both cases idle states during memory time. Reprinted (adapted) with permission from [71]. Copyright (2020) American Chemical Society.

in $\mathcal{E}$ is caused by two factors: finite bandwidth of magnetic pulses leading to imperfect transitions and pure dephasing during QEC, introducing errors which the code is not able to correct. We report in Figure 4.4 the results of simulations performed ignoring gating errors (blue and red solid lines), which can be further reduced through a careful design of both molecule and pulse shape. Note that the improvement with respect to previous more realistic simulations is small. Hence the error that we introduce is mainly due to the non-negligible duration of the QEC procedure.

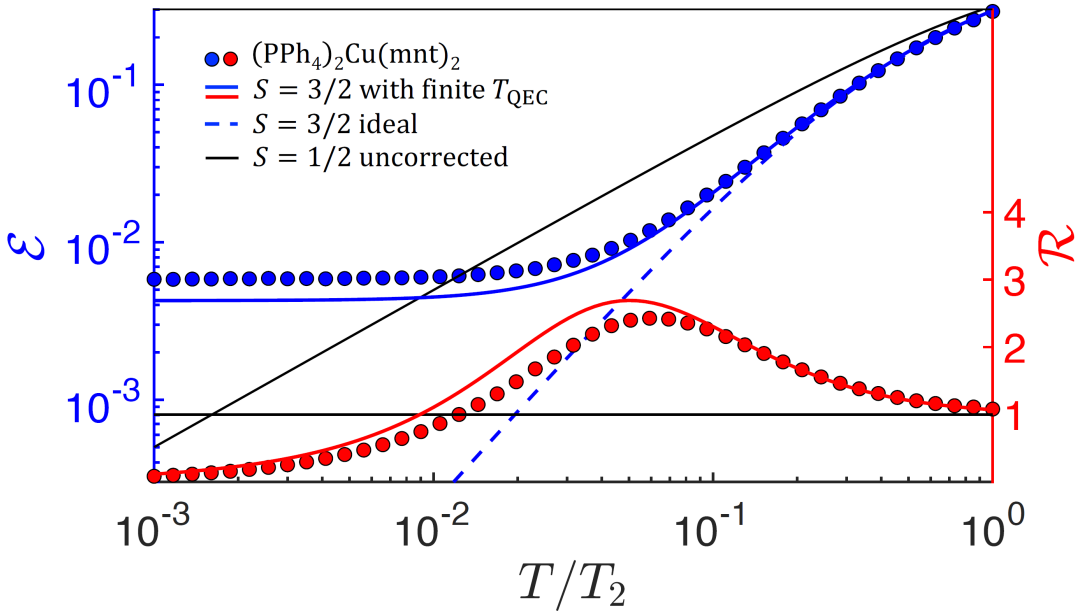

Figure 4.4: Simulated final error $\mathcal{E}$ (blue circles) as a function of T/T_2 and corresponding gain $\mathcal{R}$ (red), for the nuclear $I = 3/2$ ^{63}Cu qudit. Solid lines represent the same quantities for the same system ignoring gate errors (red and blue), and for an uncorrected qubit subject to pure dephasing (black). We also report the ideal performance of the code without both gate errors and dephasing during pulse sequences (dashed line). Reprinted (adapted) with permission from [71]. Copyright (2020) American Chemical Society.

A large $\tilde{T}$ value is of great importance for a QEC code since it represents the ideal idle time between subsequent implementations of the QEC code. The $\tilde{T} = 0.06T_2$ obtained from these simulations is really good, since it is enough to perform numerous gates between each correction step. In this regard, we simulated the effect of repeating the error-correction procedure in order to extract an enhanced T_2 describing the dephasing of our error-corrected logical qubit. We repeated n times the free evolution step and the detection/recovery steps, using $\tilde{T}$ as the idle time between correction cycles. In Figure 4.5 we report the result of this simulation, showing how the repetition of this code yields an effective $T_2^{eff} = 3.1T_2$ for the $I = 3/2$ nuclear qudit. The quantity plotted in Figure 4.5 is $2\mathcal{F}^2 - 1$ ($\mathcal{F}^2 = 1 - \mathcal{E}$), since for the uncorrected qubit it can be easily shown that $2\mathcal{F}^2 - 1 = e^{-t/T_2}$, obtaining a simple and effective comparison with our simulation.

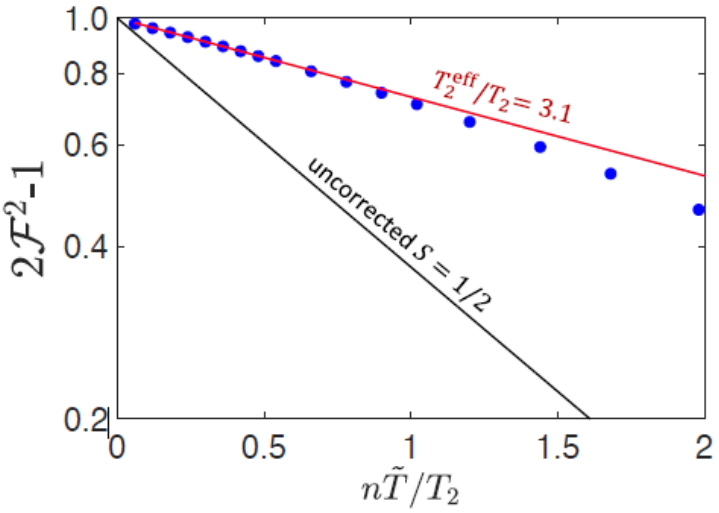

Figure 4.5: Simulated final $2\mathcal{F}^2 - 1$ (blue circles) as a function of $n\tilde{T}/T_2$, where $\tilde{T}$ is the optimal working point and n the number of QEC cycles performed. An exponential fit to our simulation (red line) shows how we effectively improve the T_2 of our system by a factor ≈ 3 if compared to the uncorrected qubit (black line). Reprinted (adapted) with permission from [71]. Copyright (2020) American Chemical Society.

4.3 $S > 3/2$

4.3.1 Pulse sequence

As stated before, incrementing the qudit spin S by 1 allows us to correct one additional power of S_z^k errors, constantly improving the performance of the code for longer T/T_2. Here, we generalised the pulse sequence for a half-integer S spin qudit, correcting S_z^k up to $k = S - 1/2$ (Figure 4.6). By expanding $\rho(t)$ over the eigenstates $\{|m\rangle\}$ we obtain this formula, describing the effect of pure dephasing on its matrix elements:

$$\rho(t) = \sum_{m,m'=-S}^{S} e^{-(m-m')^2 t/T_2} \langle m|\rho(0)|m'\rangle |m\rangle \langle m'| \tag{4.12}$$

where we note that off-diagonal elements experience an exponential decay which becomes faster for larger $|m - m'|$. Hence, dephasing has a much more disruptive effect on a high-S qudit, causing an amplification of dephasing errors during pulse sequences. Moreover, higher spin systems are also associated to longer pulse sequences, mitigating the increased correcting power of such systems.

The three sections of the code are the same shown before for the $I = 3/2$ qudit: encoding, detection and recovery. Encoding starts form the state

$$\alpha\,|-1/2,\downarrow\rangle + \beta\,|1/2,\downarrow\rangle \tag{4.13}$$

and through a carefully determined sequence of pulses (shown in Figure 4.6) we obtain the desired encoded state. The rotation angles of $|1/2,\downarrow\rangle \leftrightarrow |3/2,\downarrow\rangle$ and

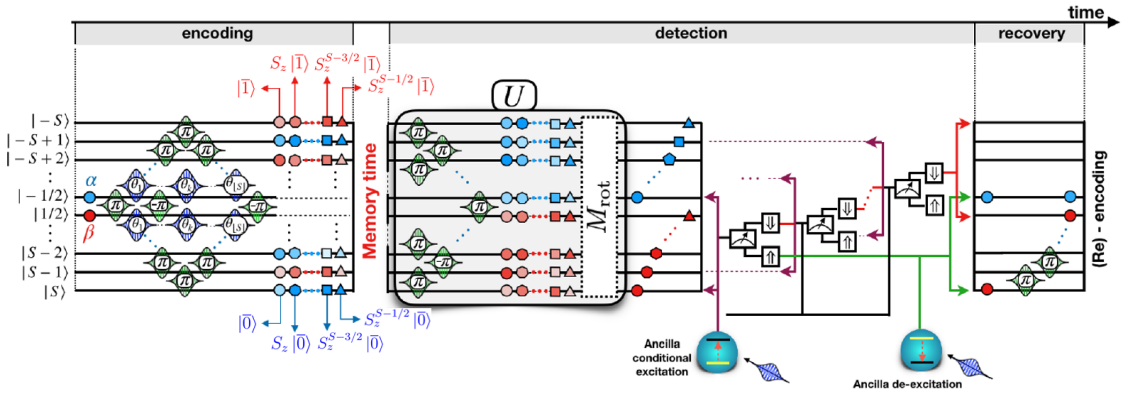

Figure 4.6: Visual representation of the pulse sequence designed to implement the QEC code on a generic half-integer spin S qudit. Horizontal lines represent the time evolution (from left to right) of the $2S+1$ eigenstates of the Hamiltonian in Eq. 4.1 with the ancilla in its non-excited state: $|m,\downarrow\rangle$. Gaussian-shaped peak functions placed between two levels represent magnetic pulses resonant with the associated $\Delta m = \pm 1$ transitions, with the rotation angle θ_k determined by Eq. 4.14. Blue (red) circles represent $|\overline{0}\rangle$ ($|\overline{1}\rangle$) states and blue (red) polygons represent $S_z^k|\overline{0}\rangle$ ($S_z^k|\overline{1}\rangle$) states. The colour intensity of circles and polygons is proportional to the modulus of the component. M_{rot} is an unitary transformation implementing the detection procedure. After the conditional excitation of the ancilla at the end of detection our procedure splits in $S+1/2$ distinct path, depending on the result of ancilla measurement. Reprinted (adapted) with permission from [71]. Copyright (2020) American Chemical Society.

$|-1/2,\downarrow\rangle \leftrightarrow |-3/2,\downarrow\rangle$ transitions are determined as:

$$\sin^2\left(\frac{\theta_k}{2}\right) = \frac{\binom{2S}{k-1}}{2^{2S-1} - \sum_{j=0}^{k-2}\binom{2S}{j}} \tag{4.14}$$

All other encoding pulses are $\pm\pi$ rotations with alternating signs in the $|1/2,\downarrow\rangle \leftrightarrow |-1/2,\downarrow\rangle$ transitions.

Note that in this more general case, the error states $S_z^k|\overline{0}\rangle$ and $S_z^k|\overline{1}\rangle$ do not form an orthonormal set like in the $I = 3/2$ case. However, implementing Gram-Schmidt orthonormalization of $S_z^k|\overline{0}\rangle$ and $S_z^k|\overline{1}\rangle$ allowed us to define the basis $|E_0^k\rangle$ and $|E_1^k\rangle$ for the error space. These orthonormal basis span the error space and fulfil Knill-Laflamme conditions (Equation 4.5). Keeping this in mind, the first step of our detection procedure is that of designing for a general spin S an unitary transformation U that brings each error state $|E^k\rangle = \alpha|E_0^k\rangle + \beta|E_1^k\rangle$ into a superposition of two qudit spin eigenstates $|m\rangle$, different for each $k = 0,\ldots,S-1/2$:

$$U|E^k\rangle = \alpha|-1/2-k,\downarrow\rangle + \beta|S-k,\downarrow\rangle \tag{4.15}$$

Note that the error states Note that the initial superposition is still preserved and each k is associated to two different $|m\rangle$, hence the error is always detectable and correctable. The determination of the pulse sequence implementing such transformation is non-trivial and details on its derivation can be found in the Supplementary Information for article [71], along the lines of [72]. The second step of error detection, just like for the $S = 3/2$ qudit, is that of conditionally exciting the ancilla to $|\uparrow\rangle$ for a given two-state superposition $U|E^k\rangle$ and measuring its state. If the measurement returns a $|\uparrow\rangle$ result, it means that the state collapsed into the corresponding error case and we proceed to the recovery step. Otherwise, if the measurement result is $|\downarrow\rangle$, then we know that the S_z^k error is not detected and we repeat this procedure for another k. We start from $k = 0$ up to $k = S-3/2$. If the last measurement returns $|\downarrow\rangle$, we apply recovery for the $k = S-1/2$ case, which is the only one that we do not need to conditionally excite. Recovery of the encoded state after ancilla measurement is achieved through a fairly simple sequence of pulses (see Figure 4.6) after which the encoding step has to be performed again.

The maximum total number of pulses needed for the implementation of this QEC code can be easily computed as $S^2 + 6S + 3/4$. However, if we calculate the duration T_{QEC} of the pulse sequence we obtain an almost linear scaling with S (Figure 4.7). This behaviour is explained by the increasingly great number of pulses that can be performed in parallel and by the faster transitions associated to larger S values.

4.3.2 Simulations

Simulations for a generic qudit spin S were performed as a function of T_2 ignoring errors arising from gate implementation, which, as shown above for the $I = 3/2$ case, give a minor effect. By analysing the gain $\mathcal{R}$, we focused on its optimal working point $\tilde{T}$ and maximum value $\tilde{\mathcal{R}}$ at $\tilde{T}$. These two values are reported in Figure 4.8 up to $S = 11/2$ as a function of T_2 in units of the elementary gating

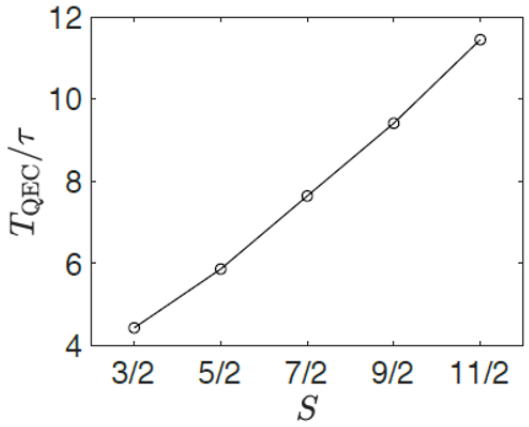

Figure 4.7: Duration T_{QEC} of the pulse sequence in units of the elementary gating time τ as a function of S. Reprinted (adapted) with permission from [71]. Copyright (2020) American Chemical Society.

time τ. A cut-off was applied excluding data with $\mathcal{E} < 0.03$ at $\tilde{T}$, hence all shown results have large final fidelities.

$\tilde{T}/\tau$ grows with the qudit spin S, thus large spin molecules require less frequent repetition of the correction procedure, which is an important aspect towards practical implementations. Moreover, such large $\tilde{T}/\tau$ values are associated to large error reductions $\tilde{\mathcal{R}}$. However, $\tilde{\mathcal{R}}$ shows a maximum for $S = 5/2$, indicating a trade-off between the longer duration of the code (causing more uncorrectable dephasing errors) and the higher number of correctable errors (up to S_z^k, with $k = S - 1/2$).

4.4 Conclusion and perspectives

In summary, in this work we have demonstrated how MNMs can prove crucial in the ongoing rush to fault-tolerant quantum computation. A single MNM with many accessible spin levels (electronic or nuclear) coupled to an electronic spin 1/2 can exploit the expanded Hilbert space to encode an error-corrected qubit. Inspired by bosonic binomial codes, we designed a QEC code able to correct dephasing errors (the most common source of errors in MNMs) on a generic spin S, even correcting higher-order S_z errors for higher qudit spins. Our proposed code has the great advantage of working within a single molecule when compared to standard QEC approaches which exploit multiple physical units. Moreover, this scheme makes much easier to implement logical operations on encoded states. As an example two-qubit gates could be implemented through the combined excitation of two coupled electronic ancillae, each one associated to its nuclear qudit, in the same fashion of what proposed in [2]. Code performance was simulated for a generic qudit spin S as a function of phase memory time T_2, obtaining promising results, especially for intermediate values of S. Additionally, realistic simulations were performed for the minimal case $S = 3/2$, correcting only S_z errors, using Hamiltonian parameters and T_2 measured on an already existing molecule[70], showing good gain and optimal working point even in this non-optimized system.

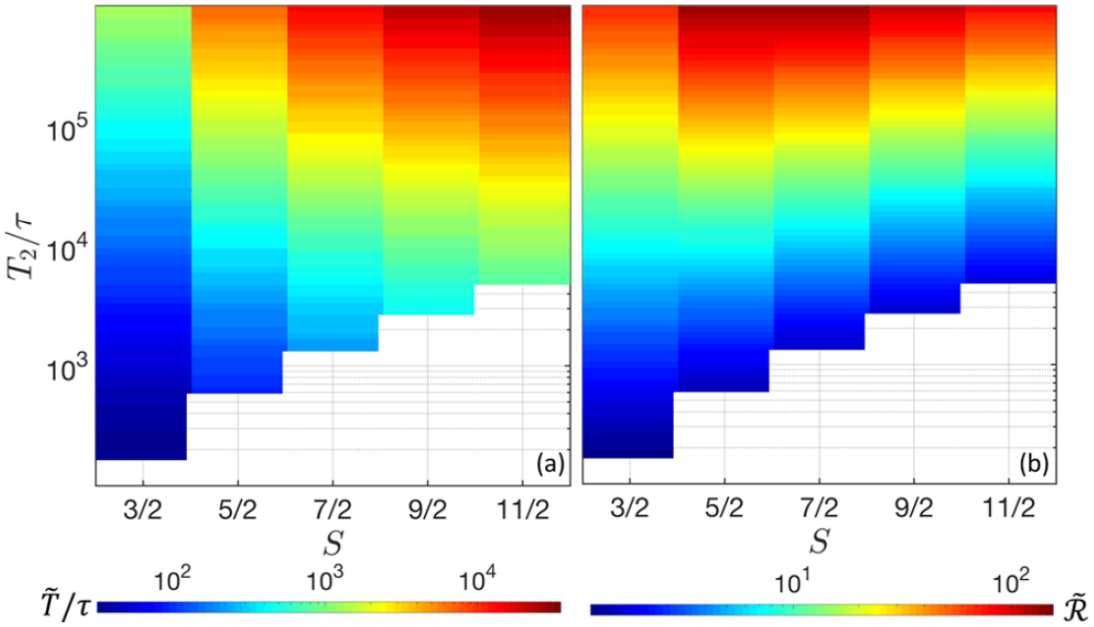

Figure 4.8: $\tilde{T}$ in units of τ and $\tilde{\mathcal{R}}$ as function of both qudit spin S and T_2/τ. Results from simulations with $\mathcal{E} > 0.03$ have been removed, showing only data associated to high fidelities. Reprinted (adapted) with permission from [71]. Copyright (2020) American Chemical Society.

It is relevant to point out that many improvements can be brought to this scheme: molecule design could lead to the synthesis of MNMs tailored for this application, careful pulse shape design could improve both gating errors and code duration, and MNMs with different level structures could be used to implement similarly derived codes. As an example for the latter possibility, molecules with competing magnetic interactions with low-spin and low-energy multiplets are good candidates. A smaller Δm between the states when compared to a spin S qudit should ensure slower dephasing (Eq. 4.12) and non-zero matrix elements between multiplets obtained with different g values could enable a shorter pulse sequence.

Chapter 5

Inelastic Neutron Scattering Investigating Phonons in High-Temperature Single Molecule Magnets

A. Chiesa, F. Cugini, R. Hussain, E. Macaluso, G. Allodi, E. Garlatti, M. Giansiracusa, C. A. P. Goodwin, F. Ortu, D. Reta, J. M. Skelton, T. Guidi, P. Santini, M. Solzi, R. De Renzi, D. P. Mills, N. F. Chilton and S. Carretta, Understanding magnetic relaxation in single-ion magnets with high blocking temperature, *Physical Review B*, **101**, 174402 (2020)

This chapter is focused on the three inelastic neutron scattering (INS) experiments in which I took part during the first two years of my PhD. All the experiments have been performed on single molecule magnets (SMMs) containing a single Dy^{3+} ion and were aimed at determining the phonon density of states of such samples.

This work was inspired by the recent discovery of magnetic hysteresis up to 60 K[8] in the $[Dy(Cp^{ttt})^2][B(C_6F_5)_4]$ (from now on referred to as *dysprosocenium*[8]) single ion magnet (SIM), where the high energy barrier for inversion of magnetization is generated by the high anisotropy of the ion's ligand cage. This discovery led to the design of similar molecules with really high energy barriers, obtaining both outstanding results[32] as well as less performing systems[73–75]. This wide performance gap is associated to the temperature dependence of magnetization relaxation times, which strongly varies between different samples. The slow relaxation of magnetization within these SIMs is strongly affected by phonons, with various effects contributing to its overall temperature dependence. Because of this, we decided to use neutrons as a probe to extract the phonon density of states (DOS) of three prototypical SIMs with high energy barriers but extremely different temperature performances. With these experimental data we have been able to both validate *ab-initio* calculations of the phonon DOS and to assess the

role of various spin relaxation processes, obtaining important indications to reach high-temperature magnetic bi-stability in this class of SIMs.

5.1 Background: high-temperature magnetic bi-stability in SIMs

Dysprosocenium-inspired SIMs are characterized by a strong easy-axis anisotropy of the ligand cage around the single rare-earth ion contained in their magnetic core. This causes a high energy barrier (U_{eff}) to separate the two magnetic ground states, hence at low temperature the system displays magnetic bi-stability and slow relaxation of magnetization between the two states. The most-important parameter when evaluating the performance of SMMs is the *blocking temperature*, which in this work is defined as the temperature at which the magnetic relaxation time reaches 100 s[33,76]. Usually, for transition metal ions-based SMMs[7], slow relaxation of magnetization in SMMs was mainly described with thermally activated Orbach processes *over* the energy barrier[77,78], with a rate $\approx e^{-U_{eff}/K_BT}$, hence with U_{eff} as the main figure of merit of the performance. However, in lanthanide-based SIMs this process alone is not able to describe the experimental results: a high U_{eff} value is not always associated to high T_B[73,75]. An evident trend in this class of SMMs is shown by the temperature dependence $\approx T^n$ of the relaxation rate in the lower-temperature regime driven by two-phonons Raman processes[33]. In fact, high T_B compounds are characterized by small n values, causing Raman relaxation to become inefficient. Greater n values are instead associated to fast Raman relaxation, leading to T_B values lower than temperatures typical of the Orbach regime. Another important process that contributes to the determination of T_B is the quantum tunnelling of magnetization (QTM), which is a temperature-independent phenomenon. The magnetization relaxation rate associated to QTM is therefore another crucial parameter, since it can hinder magnetic bi-stability even at low temperatures.

The INS experiments presented here are part of a bigger work in which combined experimental techniques and theoretical calculations have been used to understand relaxation in this class of SIMs. A precise determination of the phonon DOS of a particular system is in fact crucial to derive the correct Raman exponent which, together with U_{eff}, allows one to estimate the system's overall performance. Comparison between theoretical predictions (from *ab-initio* calculations) and experimental results allowed us to validate such simulations, obtaining an effective way to determine relaxation properties. In fact, being the INS detection of the phonon DOS too much of a cumbersome task to be undertaken for every newly-synthesized molecule, the possibility to achieve reliable predictions from *ab-initio* calculations is important. Moreover, the experimentally-detected $\rho_{nw}(E)$ is different from the phonon DOS $\rho(E)$ required for computing the relaxation dynamics. Indeed, *ab-initio* calculations allowed us to obtain both quantities, comparing $\rho_{nw}(E)$ with the experiments to validate the approach and then using $\rho(E)$ when computing relaxation dynamics.

5.2 INS experiments

INS experiments were performed on three different Dy-based SIMs: $[Dy(Cp^{ttt})^2][B(C_6F_5)_4]$ (**1**)[8], $[Dy(^tBuO)Cl(THF)_5][BPh_4]\cdot 2THF$ (**2**)[73] and $[Dy(Mes^*O)_2(THF)_2Br]$ (**3**)[79]. All molecules were synthesized and characterized by our collaborators from the University of Manchester, and the three molecular structures are shown in Figure 5.1.

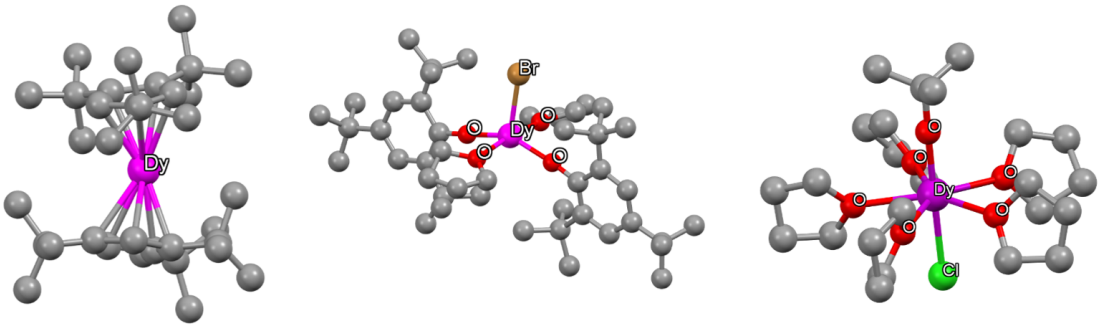

Figure 5.1: From left to right: molecular structures of **1**, **2** and **3**. Carbon atoms are in grey, hydrogen atoms are not shown for the sake of clarity and other elements are labelled within the figure.

All three molecules display high U_{eff}: 1760 K for **1**, 950 K for **2** and 1210 K for **3**. However, a greater disparity is shown in the blocking temperatures T_B of the same samples: 60 K for **1** and 4 K for **2**. Note that for **3** it is not possible to define a T_B, since relaxation due to quantum tunnelling of magnetization is too fast for this sample to display magnetic bi-stability[79]. The Raman-associated exponents were measured as $n \approx 2$ for **1**, $n \approx 5$ for **2** and $n \approx 2$ for **3**, matching the expected correlation between low n and high T_B for the first two samples.

For INS experiments we used $\approx$ 2 g of polycrystalline powder of the three samples, as well as the same amount for diamagnetic analogue samples containing a Y^{3+} ion in place of Dy^{3+}. These three additional samples allowed us to identify crystal field (CF) transitions, not present in the diamagnetic sample, and ensure the vibrational origin of the other excitations. We performed the experiments on the MERLIN spectrometer[46], at ISIS Neutron and Muon Source (STFC Rutherford Appleton Laboratory, UK). Using neutron beams with incident energies $E_i = 90$ meV, $E_i = 130$ meV and $E_i = 180$ meV, combined with a Gd Fermi chopper in repetition rate multiplication mode, we have been able to measure spectra using four/five different incident energies on the sample at the same time (Figure 5.2). This allowed us to collect spectra with optimized experimental resolution for each exchanged energy (E) regions, as shown in Figure 5.2. All spectra used for the determination of the phonon DOS have been collected at $T = 5K$.

5.3 Results

The first step of our investigation was to identify the CF excitations, expected around $50 - 60$ meV[8,73]. The spectra collected with $E_i = 90$ meV on **1** and **2** had

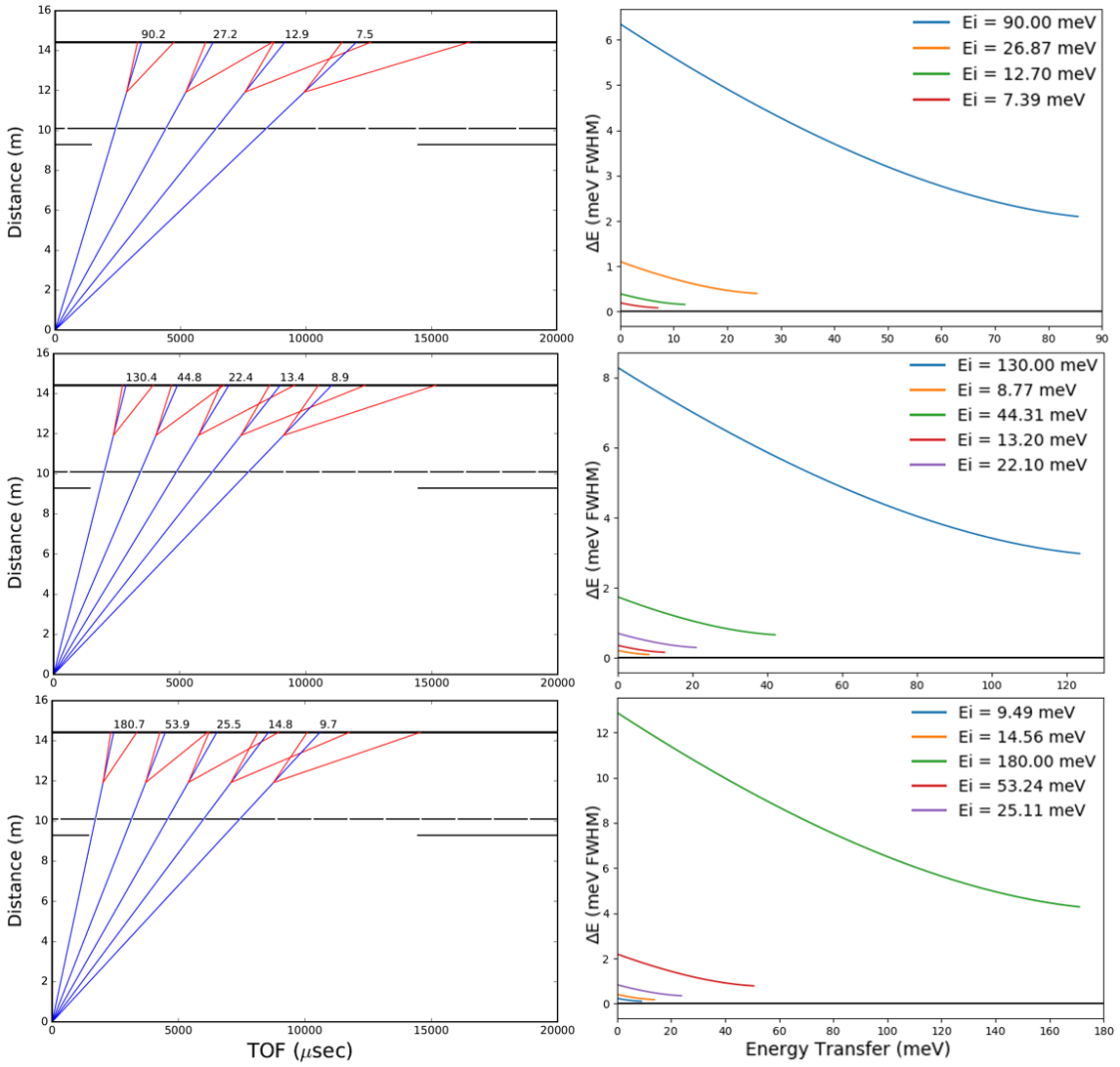

Figure 5.2: Left column: neutron incident energies for the three different experimental configurations ($E_i = 90$ meV and $\nu = 250$ Hz, $E_i = 130$ meV and $\nu = 350$ Hz, $E_i = 180$ meV and $\nu = 350$ Hz). Right column: experimental resolution (FWHM) of the measured signal for the same three configurations. Each plot shows all the possible incident energies of that configuration given the RRM mode. Figures generated using the Mantid software package[45].

the right experimental resolution to detect CF excitations at energies close to those expected. This was possible through careful subtraction of the spectra collected on the analogue diamagnetic samples to those collected on magnetic samples. By studying the dependence of the remaining signal on the exchanged moment Q we found only one peak for each compound to be of magnetic origin (Figure 5.3, top panels). In fact, vibrational excitations' signal increases with Q^2, as opposed to magnetic excitations, which rapidly decrease by increasing Q. These magnetic excitations were found at $E = 67$ meV for **1** and at $E = 62$ meV for **2**, compatible with previous *ab-initio* simulations (≈ 58 meV for **1**[8] and ≈ 49 meV for **2**[73]).

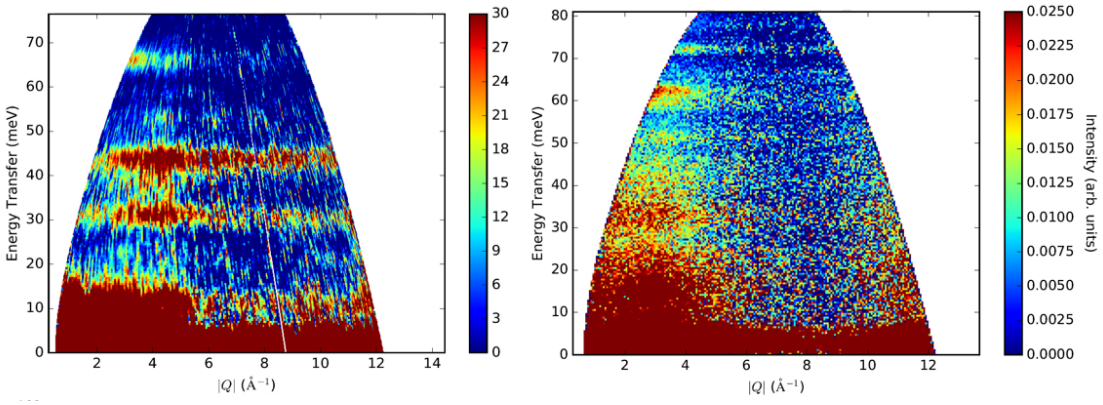

Figure 5.3: Spectra collected with $E_i = 90$ meV on **1** (left) and **2** (right) after the subtraction of the same spectra collected on the respective diamagnetic analogues.

Our next step consisted in the extraction of the neutron-weighted phonon DOS $\rho_{nw}(E)$ through the incoherent approximation (Eq. 1.35), using the Mantid built-in function *ComputeIncoherentDOS*[45]. In order to correctly implement the function, we had to carefully choose an (E, Q) range, respecting the requirements of the incoherent approximation (see section 1.4.5). By doing so, we obtained a $\rho_{nw}(E)$ for each measured spectrum, which we successively merged into one single curve by keeping for each energy range only the values with the best resolution (i.e. the smallest E_i, Figure 5.2 bottom row). It is worth to underline that in order to merge different curves we had to normalize each spectrum based on the intensity of the neutron beam incident on the sample, which varies for different E_i. This quantity, measured during the experiments by several monitors, was used to correct the corresponding spectra, obtaining a good agreement in all the merging points between different E_i measurements.

The final results for the experimental determination of $\rho_{nw}(E)$ are shown as coloured circles in Figure 5.4 for all three molecules. Each colour indicates a different incident energy: for **1** we used $E_i = 13, 25, 54, 90, 180$ meV; for **2** we used $E_i = 13, 27, 54, 90, 180$ meV; for **3** we used $E_i = 13, 25, 27, 54, 90, 130$ meV. The same quantity was also determined *ab-initio* by our collaborators, starting from the partial phonon DOS $\rho_k(E)$ which are computed for each element. *Ab-initio* calculations on **1** were performed by the Manchester group using CASTEP software[80] for structure optimization and Phonopy[81] for phonon DOS calculations on an $8 \times 8 \times 8$ grid in **k** space. The same calculations on **2** and **3** were performed here in Parma using QuantumESPRESSO code[82–84] for structure optimization and

Phonopy[81] for phonon DOS calculations on a $2 \times 2 \times 2$ grid in $\mathbf{k}$ space. In all three simulations (Figure 5.4, solid lines), $\rho_{nw}(E)$ was obtained using the experimental FWHM (Figure 5.2, bottom row) for each energy range.

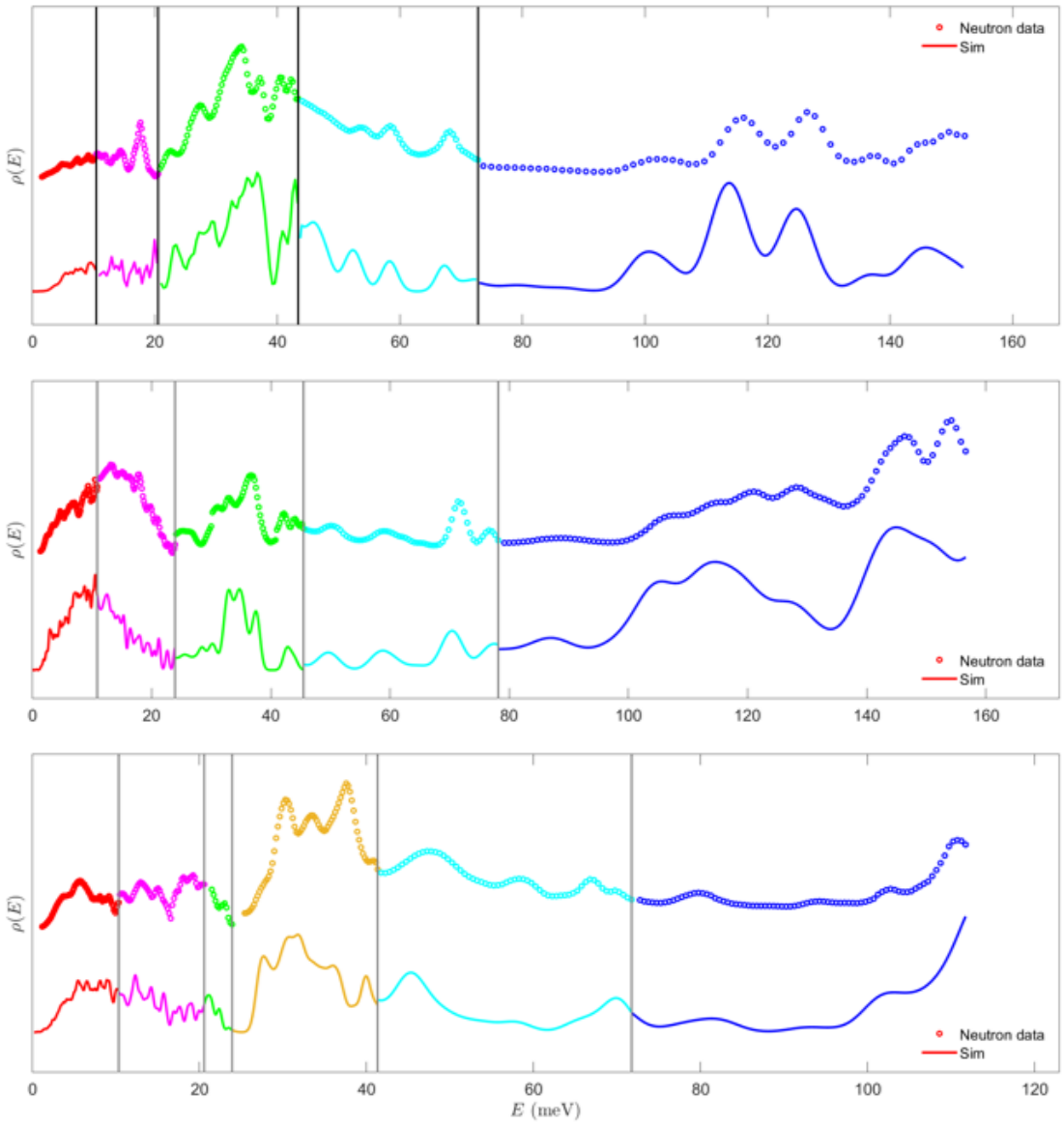

Figure 5.4: Comparison between experimentally-determined $\rho_{nw}(E)$ (circles) and those obtained from *ab-initio* calculations (solid lines) for **1** (top), **2** (middle) and **3** (bottom).

5.4 Discussion and conclusions

The agreement between the experimentally determined $\rho_{nw}(E)$ and the calculated ones is excellent, demonstrating the robustness of *ab-initio* calculations in determining the phonon DOS of these compounds. The neutron-weighted phonon DOS $\rho_{nw}(E) = \sum_k \frac{\sigma_{inc,k}}{2M_k}\rho_k(E)$ is calculated based on simulations of all the partial DOS $\rho_k(E)$, which can also be combined to reconstruct the phonon DOS

$\rho(E) = \sum_k \rho_k(E)$. In fact, INS experiments are only able to probe $\rho_{nw}(E)$, whereas *ab-initio* calculations require $\rho(E)$. Hence, through INS experiments we validated DFT calculations, which have been then used to compute relaxation dynamics for **1**.

A reliable method for calculating the phonon DOS of rare-earth SIMs is crucial for determining the efficiency of relaxation driven by Raman processes. These have been modelled on **1** starting from the *ab-initio* calculated phonon DOS and compared with experimental findings (DC and AC magnetometry and high-field NMR). A very good agreement was found between prediction and experimental results (see Figure 5.5) over a very wide temperature range[85]. This results also yield profound insight on relaxation mechanisms, confirming the important role of Raman processes in the high-temperature magnetic bi-stability of **1**. The Raman exponent derived from the calculated DOS is $n = 2.1 - 2.3$, in excellent agreement with experiments[8]. This low n value is associated to the flat shape of the phonon DOS in the range $\approx 5 - 20$ meV (associated to low-energy optical modes) and to a large CF energy gap between the two lowest Kramers doublets. These are the key ingredients leading to the suppression of Raman relaxation and high-temperature magnetic bi-stability in rare-earth SIMs.

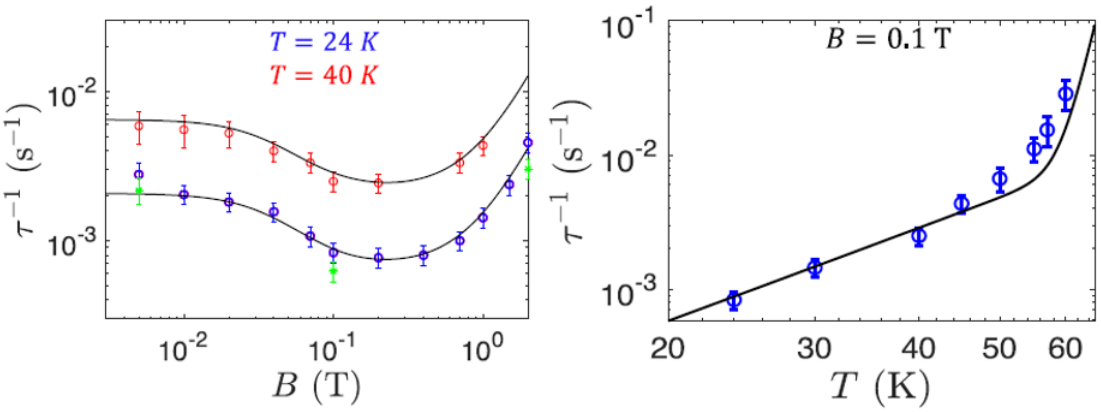

Figure 5.5: Left: relaxation rate τ^{-1} as a function of magnetic field at 24 K (blue) and 40 K (red). Experimental data (circles) extracted from DC magnetization measurements are compared to calculations (lines). Data in green circles are collected at 24 K and $\theta = 0°$. Right: relaxation rate τ^{-1} as a function of temperature with $B = 0.1$ T and $\theta = 60°$. Experimental data (circles) extracted from DC magnetization measurements are compared to calculations (lines). Reprinted figure with permission from [A. Chiesa, F. Cugini, R. Hussain, E. Macaluso, G. Allodi, E. Garlatti, M. Giansiracusa, C. A. P. Goodwin, F. Ortu, D. Reta, J. M. Skelton, T. Guidi, P. Santini, M. Solzi, R. De Renzi, D. P. Mills, N. F. Chilton, and S. Carretta, Physical Review B, 101, 174402 (2020), DOI: 10.1103/PhysRevB.101.174402][85], Copyright (2020) by the American Physical Society.

Looking at the phonon DOS of **2**, we expect to find a higher Raman exponent, given the steeper growth in the $5 - 8$ meV range when compared to **1**, similar to what was experimentally determined[73]. This large n value leads to fast relaxation driven by Raman processes, at temperatures much lower than those associated to Orbach relaxation, which is consistent with the low blocking temperature measured

for **2**. However, further analysis of relaxation dynamics based on the phonon DOS of **2** and **3** are in the works.

In summary, the INS experiments presented in this chapter played a key role in the validation of the DFT simulations of the phonon DOS, allowing one to compute relaxation properties of SIMs starting from *ab-initio* calculations. A comparison between experimental results and theoretical calculations of the relaxation dynamics on **1** confirmed the fundamental role played by slow Raman relaxation in order to achieve more performing SIMs. However, thermally-activated Orbach processes are still crucial when describing these systems, effectively determining the blocking temperature of a given compound.

Chapter 6

Many-body+DFT Investigating Transport Through a Molecular Ni Dimer

A. Chiesa, E. Macaluso, P. Santini, S. Carretta and E. Pavarini, First-principles many-body models for electron transport through molecular nanomagnets, *Physical Review B*, **99**, 235145 (2019)

In this chapter we focus on how the combination of density functional theory (DFT) and many-body (MB) methods can yield profound insight on electron transport through strongly-correlated MNMs. In recent years, advances in molecular spintronics have led to the possibility of manipulating a single molecular spin[86] by electric fields, which is of great interest for quantum information processing[87]. Such systems could in principle be used for gate implementation and read-out of single qubits[86–90]. Molecular qubits enable the bottom-up construction of complex structures binding MNMs to each other or grafting them to surfaces[91,92]. One of the simplest physical realizations of a transport experiment with MNMs consists in linking the molecule to two conducting nanoleads and to a gate voltage (V_G), which guarantees control over the quantized charge on the MNM. This configuration resembles a single-electron transistor[93,94], in which we can control the electron tunnelling through the molecule by manipulating V_G and the bias voltage V applied to the nanoleads. In this work we simulated transport phenomena on a prototypical Ni_2 molecular dimer in a junction configured as described above. In order to do this, we combined *ab-initio* calculations with many-body models (DFT+MB), in the same fashion of [36], correctly describing effects associated to the strong correlation typical of these systems. The results confirmed the efficiency of our method, demonstrating how DFT+MB proves itself as a valuable tool even in describing transport properties of strongly-correlated systems, in addition to static magnetic properties.

6.1 Outline

A precise theoretical prediction of electron transport is essential for the correct design of molecular spintronic nanostructures. However, strongly-correlated molecules such as MNMs pose a challenge to most *ab-initio* simulations of transport experiments. Most classical DFT approaches include correlation effects at a static mean-field level[34], thus failing in correctly representing phenomena out of reach for this description, such as negative differential conductance or current suppression[95]. What we propose in this work was describing transport properties of MNMs using the MB+DFT approach described in Section 1.2.3, which is effective in describing magnetic properties of MNMs at equilibrium by correctly including correlation effects[36]. The use of a generalized Hubbard model naturally suits to transport phenomena, since it describes states with a different number of electrons using the same parameters. Therefore, we tested the performance of this method on a prototypical Ni_2 molecular dimer[96,97] ($[(Ni(hfacac)_2)_2(bpym)]$, see Figure 6.1 for its molecular structure), weakly coupled to two clusters modelling the gold nanoleads[98,99]. This is an ideal system in which we reasonably expected to find effects clearly associated to strong correlation.

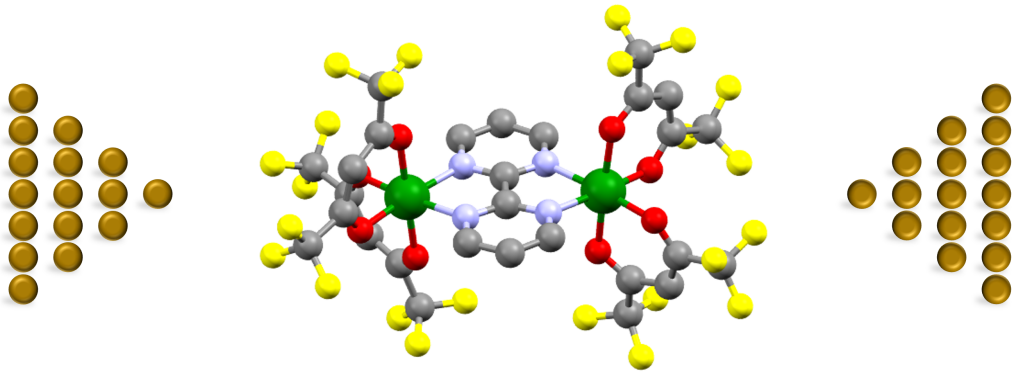

Figure 6.1: Molecular structure of the molecule $[(Ni(hfacac)_2)_2(bpym)]$. Ni atoms are shown in green, O in red, N in light purple, F in yellow and C in grey. H atoms are not shown for better visualization of the structure. The orange triangles on both sides represent the two gold leads weakly coupled to the molecular dimer.

In order to obtain a complete description of transport properties we first need to build a system-specific Hubbard model for the system. This is what my work was mainly focused on obtaining. These results are the basis on which the transport model was then built through the master equation formalism, simulating transport phenomena strictly associated to strong correlation, which we explicitly considered with the DFT+MB method.

6.2 Hubbard model for the Ni dimer

The first step consisted in performing local density approximation (LDA) DFT calculations for the molecule on the NWChem[38] code, employing a triple-zeta

valence basis set. This process allowed us to recognize the d-like states close to the Fermi level on which we apply the Foster-Boys localization[100]. The Foster-Boys orbitals obtained from this process were used to build a generalized Hubbard model for the molecule:

$$\begin{aligned}\hat{H} = &-V_G \sum_{i,m,\sigma} c^{\dagger}_{im\sigma} c_{im\sigma} - \sum_{i,i'} \sum_{m,m',\sigma} t^{i,i'}_{m,m'} c^{\dagger}_{im\sigma} c_{i'm'\sigma} + \\ &+ \frac{1}{2} \sum_{i,\sigma,\sigma'} \sum_{m \neq m'} (U - 2J_H - J_H \delta_{\sigma,\sigma'}) \hat{n}_{im\sigma} \hat{n}_{im'\sigma'} + \\ &- \sum_{i,m \neq m'} J_H \left[\hat{c}^{\dagger}_{im\uparrow} \hat{c}^{\dagger}_{im\downarrow} \hat{c}_{im'\uparrow} \hat{c}_{im'\downarrow} + \hat{c}^{\dagger}_{im\uparrow} \hat{c}_{im\downarrow} \hat{c}^{\dagger}_{im'\downarrow} \hat{c}_{im'\uparrow} \right] + \\ &+ \sum_i \lambda_i \sum_{m,m',\sigma,\sigma'} \xi^i_{m\sigma m'\sigma'} c^{\dagger}_{im\sigma} c_{im'\sigma'} - \hat{H}_{DC}\end{aligned} \tag{6.1}$$

where $c^{\dagger}_{im\sigma}$ and $c_{im\sigma}$ are, respectively, creation and annihilation operators of $3d$ electrons with spin σ on site i in the Foster-Boys orbital m. The first term accounts for gate potential energy V_G, which is multiplied to the total number operator. The second term is the hopping term, where the parameters $t^{i,i'}_{m,m'}$ are the crystal-field (CF) integrals if $i = i'$ or the hopping integrals if $i \neq i'$. The third term includes same-site Coulomb repulsion and the fourth term pair-hopping and spin-flip (explained in Section 1.2.3), both depending on the averaged screened Coulomb couplings U and J_H. The fifth term accounts for spin-orbit interaction, whose strength is quantified by the parameter λ_i, equal for all electrons of the same site; $\xi^i_{m\sigma m'\sigma'}$ are spin-orbit matrix elements written in the Foster-Boys basis (see Section 1.2.3). H_{DC} is the double-counting correction, removing the already included mean-field part of same-site Coulomb interaction.

The determination of these parameters was done based on the results obtained by DFT-LDA simulations. Coulomb couplings U and J_H were calculated with a constrained-LDA (cLDA, see Section 1.2.3) approach, obtaining $U = 6.3$ eV and $J_H = 0.26$ eV. CF integrals are evaluated by diagonalization of the on-site matrix $t^{i,i'}_{m,m'}$, obtaining orbital energies $\varepsilon^1_m = 0, 0.116, 0.248, 1.666, 1.721$ eV on the first Ni site and $\varepsilon^2_m = 0.071, 0.155, 0.260, 1.662, 1.716$ eV on the second Ni site, where energy grows by increasing $m = 1, ..., 5$ on each site. Note that the approximately octahedral environment of the Ni^{2+} ions splits the energy levels into higher e_g-like states and lower t_{2g}-like states, as outlined in Figure 6.2. The strength λ_i of the spin-orbit coupling can be determined by comparing single-electron CF splittings calculated with or without the inclusion of spin-orbit interaction in the DFT calculations. Since such relativistic self-consistent calculations are extremely time-consuming, we opted to use tabulated[39] single-ion λ_i values, which yield a very good approximation in these compounds, as already shown in [36].

6.3 Low-energy effective spin Hamiltonian

In order to correctly describe the neutral molecule we need to diagonalize H within the subspace with $N = 16$ electrons (8 per site). The lowest energy states with

$N = 16$ electrons are a singlet, a triplet and a quintet, arising from $s_i = 1$ ionic configurations, as shown in figure 6.2. This subspace can be described with an effective spin Hamiltonian composed of an isotropic Heisenberg exchange term and a zero-field splitting (ZFS) term:

$$H_{eff} = J\mathbf{s}_1 \cdot \mathbf{s}_2 + \sum_i \mathbf{s}_i \cdot \mathbf{D}_i \cdot \mathbf{s}_i \tag{6.2}$$

where J is the isotropic coupling and $\mathbf{D}_i$ the ZFS tensor. $\mathbf{D}_i$ is determined by the combined effect of CF and spin-orbit interaction and was calculated by downfolding the spin-orbit matrix in the $s_i = 1$ ground multiplet, obtaining the effective ZFS Hamiltonian. From this Hamiltonian we derived the $\mathbf{D}_i$ tensor, whose diagonalization allowed us to determine ZFS parameters $d_1 = 90$ μeV, $d_2 = 34$ μeV and $e_i = 0.12 d_i$, indicating easy-plane anisotropy in both Ni^{2+} ions. Small differences between the ligand cages of the two ions (a compression along z and a tilt with respect to the anisotropic axis) are associated to the different values of d_1 and d_1 Isotropic coupling J is obtained as the sum of the ferromagnetic screened Coulomb coupling J_H (already obtained by cLDA calculations) and an antiferromagnetic superexchange $\mathcal{J}$. The latter was determined by considering the effect of the hopping term of H in the $N = 16$ subspace with $N_1 = 7, 8, 9$ electrons on the first ion and $N_2 = 9, 8, 7$ electrons on the second, respectively. Through diagonalization of the hopping matrix written in this subspace, the 9 lowest energy states that we found correspond to the same three total spin multiplets described by the effective Hamiltonian 6.2. This procedure allowed us to precisely determine $\mathcal{J} = 3.3$ meV, since those levels are separated by energies $\mathcal{J}$ and $2\mathcal{J}$ (Figure 6.2), with a negligible split induced by anisotropic exchange. This value is in accordance with what was previously experimentally measured via inelastic neutron scattering[97].

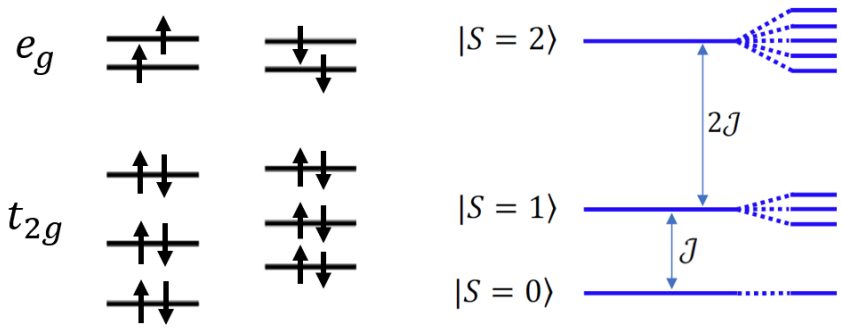

Figure 6.2: Left: orbital occupations on both sites in the $N = 16$ ground state. Right: energy scheme described by Hamiltonian 6.2, evidencing the splitting between total-spin multiplets induced by isotropic exchange $\mathcal{J}$.

Moreover, to describe transport phenomena we need to study the properties of the ionized system with $N + 1$ electrons. In this case we found a ground multiplet with $S = 3/2$, which means that the ground state of the system changes from $S = 0$ to $S = 3/2$ upon injecting an extra electron. This happens because the antiferromagnetic superexchange between the two ions is dominated by the *Nagaoka*[99] *mechanism*, which maximizes the spin. In this state, in fact, it is possible for the

extra electron to gain kinetic energy by hopping between ion sites without any Coulomb energy cost, causing an energy gain in the hopping integral and an effective ferromagnetic interaction between the ions. This property potentially enables control over the spin state by manipulating bias and gate voltage. Moreover, since without spin-orbit coupling transitions with $\Delta S > 1/2$ are forbidden, interesting transport phenomena like spin blockade and negative differential conductance are possible for certain (V, V_G) values.

6.4 Simulations of transport and conclusions

Whereas my work was for the most part focused on obtaining the parameters of the many-body model studying the properties of the $N = 16$ and $N+1$ electrons ground states, we also simulated transport phenomena through the sample. Using these precisely determined parameters we were able to compute current and differential conductance through the molecule. The first step towards this goal was including the two gold electrodes in the DFT calculations as finite clusters. With the orbitals obtained from these calculation we built the total Hamiltonian

$$H_{tot} = H + H_{el} + H_T \tag{6.3}$$

where H is the Hubbard Hamiltonian defined in Eq. 6.1 H_{el} is the Hamiltonian written on the two electrodes and H_T the Hamiltonian describing electron tunnelling between electrodes and molecular orbitals. In the weak electrode-molecule interaction limit we can treat H_T as a perturbation of the system, considering only single-electron tunnelling processes. H_{tot} was then used in the master equation formalism to compute time-dependent transport phenomena. This allowed us to calculate the current in an out of the molecule as a function of bias (V) and gate (V_G) voltage (we report current and differential conductance in Figure 6.3). Results included negative conductance (represented by the dark line in the right panel of Figure 6.3) and *spin blockade* effect, in which certain transitions are suppressed in a fixed (V, V_G) region, allowing controlled current suppression through the molecule. This possibility of electrically controlling the spin state of this system is of great interest in the field of both spintronics and QIP.

In summary, we simulated transport phenomena through a Ni_2 dimer weakly coupled to gold leads. In order to correctly consider the strong-correlation typical of MNMs, we used the DFT+MB method (Section 1.2.3). This approach exploits DFT calculations to determine the parameters of a many-body Hubbard Hamiltonian for the system, without any *a priori* assumption on its form. By studying the lowest energy states of the molecule with $N = 8 + 8$ electrons, we were able to describe this 9-levels subspace with a spin Hamiltonian comprised of an Heisenberg exchange term and a ZFS term, which were both precisely determined starting from the many-body model. This model, with the addition of many-body Hamiltonians for the gold leads and tunnelling electrons, was then used to calculate single-electron currents through the molecule as a function of both V and V_G. The $N+1$ electrons state in which the molecule is brought by adding an electron during transport is really interesting, since it has a $S = 3/2$ (maximum spin) ground multiplet, as opposed to the $S = 0$ ground state of the neutral system. This leads to

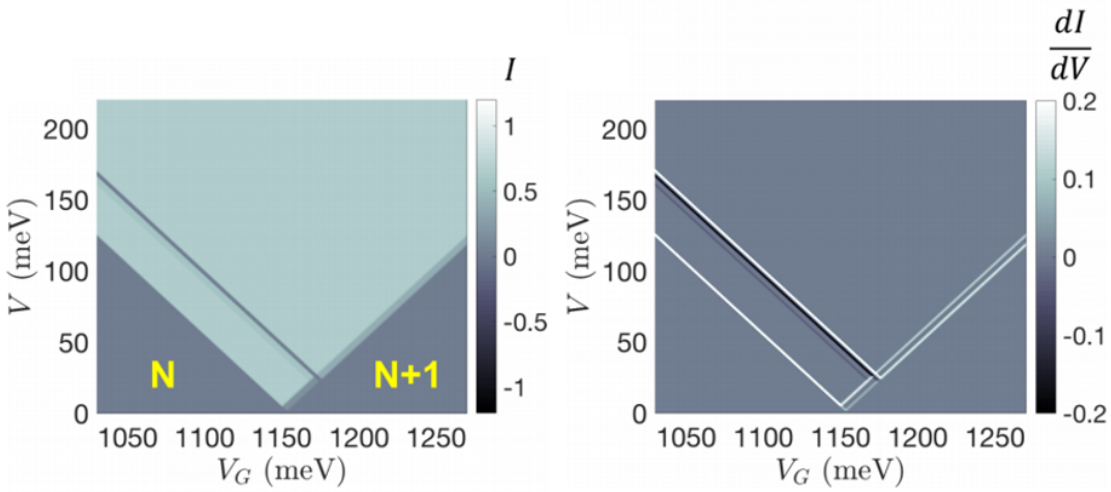

Figure 6.3: Calculated current I (left) and differential conductance dI/dV (right) as a function of bias (V) and gate (V_G) voltage at $T = 2$ K. Reprinted figure with permission from [A. Chiesa, E. Macaluso, P. Santini, S. Carretta and E. Pavarini, Physical Review B, 99, 235145 (2019)][101] Copyright (2019) by the American Physical Society.

spin blockade and negative conductance for certain values of bias and gate voltages. These phenomena are direct consequences of strong intra-molecular correlations, which we explicitly included in our model using the DFT+MB approach. This method had been previously proven[36] as a valuable tool in calculating magnetic properties of strongly-correlated MNMs and, in this case, we also tested its reliability in simulating transport properties of the same systems. Such properties of this Ni_2 molecular dimer have been investigated only in the strong electrode-molecule coupling regime[102], evidencing Kondo mechanisms at play. Hence experiments in the weak-coupling regime, as we simulated within this work, would make for an interesting test for the reliability of this method.

Chapter 7

Conclusions

Drawing a comprehensive conclusion covering the different chapters of this PhD thesis is not an easy task, but I feel that it is possible to confidently separate the final remarks into two distinct areas.

Molecular magnetism and quantum error correction. The two works exposed in chapters 3 and 4 place themselves in a really important and thriving theme in quantum information processing: the realization of logical units supporting quantum error correction, which represents one of the most important steps of the NISQ era[11]. Future upscaling of quantum computers' size and computational power requires this step to be taken in order to fulfil the extraordinary expectations in this field. Molecular nanomagnets have already been extensively studied as potential $S = 1/2$ qubit candidates, given the remarkably long coherence times found in certain compounds and the high degree of control given by coordination chemistry. In these two works we propose a different role for molecular nanomagnets in the rush towards scalable quantum computing architecture. Tailored interaction between different magnetic ions and the use of nuclear spins allowed us to exploit the additional spin levels of these systems to encode an error-protected qubit within a single physical unit. We followed two different approaches: a repetition code on multiple spins $S = 1/2$ and a binomial code using higher-spin states $S \geq 3/2$. In both cases, my contribution was focused on designing the actual codes and performing realistic simulations of their implementation, using parameters determined from real molecules, finally obtaining really promising performances. Moreover, in chapter 3 I also determined spin Hamiltonian parameters through an extensive fitting of experimental data. These results showcase how molecular nanomagnets tunability could be a key factor in the development of quantum error-corrected units for quantum computation, even through targeted molecule design.

Theoretical investigation of molecular nanomagnets. In the last two chapters molecular nanomagnets and molecule design are indeed the major focuses. In fact, the predictive power of theoretical tools in determining the properties of a given molecule is fundamental in improving design and driving synthetic efforts. In chapter 5 we outline how rare-earth single-ion magnets represent the ultimate goal in miniaturization of magnetic information storage units. I directly contributed

to performing the inelastic neutron scattering experiments and the subsequent extraction of neutron-weighted phonon density of states from collected spectra. This quantity allowed us to validate *ab-initio* simulations of phonon density of states of Dy-based single-ion magnets, obtaining an excellent agreement. These results are essential in understanding the main mechanisms of spin relaxation and their interplay in rare-earth single-ion magnets, as well as in improving theoretical prediction methods. In chapter 6, the combination of many body (MB) models with *ab-initio* density functional theory (DFT) simulations allowed us to prove the possibility of extending such predictive methods to transport phenomena. In particular, I performed MB+DFT calculations on a prototypical Ni dimer, as described in section 1.2.3, fully accounting for electron correlations, which play a key role in determining the properties of strongly correlated systems like molecular nanomagnets. Transport phenomena are also of great interest in potential quantum information processing applications for molecular nanomagnets, since read-out and manipulation of molecular spins by electronic means are definitely a promising way of addressing single quantum units.

Nonetheless, these diverse research topics share a prominent position in current research on quantum computation and information storage. A series of important breakthroughs is to be expected in the next few years, with new technologies constantly on the rise and new research avenues opening up. I think that the possibility to spend my PhD years working in fields of such current relevance constitutes an invaluable income for me, both as a scientist and as a person.

Bibliography

[1] M. Mannini, F. Pineider, C. Danieli, F. Totti, L. Sorace, P. Saintctavit, M.-A. Arrio, E. Otero, L. Joly, J. C. Cezar, A. Cornia and R. Sessoli, *Nature*, 2010, **468**, 417–421.

[2] M. Atzori, A. Chiesa, E. Morra, M. Chiesa, L. Sorace, S. Carretta and R. Sessoli, *Chem. Sci.*, 2018, **9**, 6183.

[3] M. D. Jenkins, D. Zueco, O. Roubeau, G. Aromí, J. Majer and F. Luis, *Dalton Trans.*, 2016, **45**, 16682.

[4] A. Gaita-Ariño, F. Luis, S. Hill and E. Coronado, *Nature Chem.*, 2019, **11**, 301–309.

[5] F. Troiani, A. Ghirri, M. Affronte, S. Carretta, P. Santini, G. Amoretti, S. Piligkos, G. Timco and R. E. P. Winpenny, *Phys. Rev. Lett.*, 2005, **94**, 207208.

[6] M. Mannini, F. Pineider, P. Sainctavit, C. Danieli, E. Otero, C. Sciancalepore, A. M. Talarico, M.-A. Arrio, A. Cornia, D. Gatteschi and R. Sessoli, *Nature Mater.*, 2008, **8**, 194–197.

[7] R. Sessoli, D. Gatteschi, A. Caneschi and M. A. Novak, *Nature*, 1993, **365**, 141–143.

[8] C. A. P. Goodwin, F. Ortu, D. Reta, N. F. Chilton and D. P. Mills, *Nature*, 2017, **548**, 439–442.

[9] M. Evangelisti, A. Candini, A. Ghirri, M. Affronte, E. K. Brechin and E. J. L. McInnes, *Applied Physics Letters*, 2005, **87**, 072504.

[10] J. J. Baldoví, S. Cardona-Serra, J. M. Clemente-Juan, L. Escalera-Moreno, A. Gaita-Ariño and G. Mínguez-Espallargas, *Eur. Phys. Lett.*, 2015, **110**, 33001.

[11] J. Preskill, *Quantum*, 2018, **2**, 79.

[12] F. Arute, K. Arya, R. Babbush, B. D, J. C. Bardin, R. Barends, R. Biswas, S. Boixo, F. G. L. Brandao, D. A. Buell and et. al., *Nature*, 2019, **574**, 505–510.

[13] D. P. DiVincenzo, *Fortschritte der Physik*, 2000, **48**, 771–783.

[14] G. Wendin, *Rep. Prog. Phys.*, 2017, **80**, 106001.

[15] F. Luis, A. Repollés, M. J. Martínez-Pérez, D. Aguilá, O. Roubeau, D. Zueco, P. J. Alonso, M. Evangelisti, A. Camón, J. Sesé, L. A. Barrios and G. Aromí, *Phys. Rev. Lett.*, 2011, **107**, 117203.

[16] J. Ferrando-Soria, E. Moreno-Pineda, A. Chiesa, A. Fernandez, S. A. Magee, S. Carretta, P. Santini, I. Vitorica-Yrezabal, F. Tuna, E. J. L. McInness and R. E. P. Winpenny, *Nat. Commun.*, 2016, **7**, 11377.

[17] M. J. Martínez-Pérez, S. Cardona-Serra, C. Schlegel, F. Moro, P. J. Alonso, H. Prima-García, J. M. Clemente-Juan, M. Evangelisti, A. Gaita-Ariño, J. Sesé, J. van Slageren, E. Coronado and F. Luis, *Phys. Rev. Lett.*, 2012, **108**, 247213.

[18] R. Hussain, G. Allodi, A. Chiesa, E. Garlatti, D. Mitcov, A. Konstantatos, K. Pedersen, R. D. Renzi, S. Piligkos and S. Carretta, *J. Am. Chem. Soc.*, 2018, **140**, 9814–9818.

[19] M. Trif, F. Troiani, D. Stepanenko and D. Loss, *Phys. Rev. Lett.*, 2008, **101**, 217201.

[20] M. Atzori, L. Tesi, E. Morra, M. Chiesa, L. Sorace and R. Sessoli, *J. Am. Chem. Soc.*, 2016, **138**, 2154–2157.

[21] M. Atzori, L. Tesi, S. Benci, A. Lunghi, R. Righini, A. Taschin, R. Torre, L. Sorace and R. Sessoli, *J. Am. Chem. Soc.*, 2017, **139**, 4338–4341.

[22] M. Atzori, S. Benci, E. Morra, L. Tesi, M. Chiesa, R. Torre, L. Sorace and R. Sessoli, *Inorg. Chem.*, 2018, **57**, 731–740.

[23] M. Atzori, E. Morra, L. Tesi, A. Albino, M. Chiesa, L. Sorace and R. Sessoli, *J. Am. Chem. Soc.*, 2016, **138**, 11234–11244.

[24] J. M. Zadrozny, J. Niklas, O. G. Poluektov and D. E. Freedman, *ACS Cent. Sci.*, 2015, **1**, 488.

[25] C.-J. Yu, M. J. Graham, J. M. Zadrozny, J. Niklas, M. D. Krzyaniak, M. R. Wasielewski, O. G. Poluektov and D. E. Freedman, *J. Am. Chem. Soc.*, 2016, **138**, 14678–14685.

[26] D. Aguil'a, D. Barrios, V. Velasco, O. Roubeau, A. Repollés, P. Alonso, J. Sesé, S. Teat, F. Luis and G. Aromí, *J. Am. Chem. Soc.*, 2014, **136**, 14215.

[27] A. Chiesa, G. F. S. Whitehead, S. Carretta, L. Carthy, G. A. Timco, S. J. Teat, G. Amoretti, E. Pavarini, R. E. P. Winpenny and P. Santini, *Sci. Rep.*, 2014, **4**, 7423.

[28] C. Bonizzoni, A. Ghirri, M. Atzori, L. Sorace, R. Sessoli and M. Affronte, *Sci. Rep.*, 2017, **7**, 13096.

[29] K. Bader, M. Winkler and J. van Slageren, *Chem. Commun.*, 2016, **52**, 3623–3626.

[30] S. Carretta, P. Santini, G. Amoretti, M. Affronte, A. Candini, A. Ghirri, I. S. Tidmarsh, R. H. Laye, R. Shaw and E. J. L. McInnes, *Phys. Rev. Lett.*, 2006, **97**, 207201.

[31] W. Wernsdorfer, T. Ohm, C. Sangregorio, R. Sessoli, D. Mailly and C. Paulsen, *Phys. Rev. Lett.*, 1999, **82**, 3903–3906.

[32] F.-S. Guo, B. M. Day, Y.-C. Chen, M.-L. Tong, A. Mansikkamäki and R. A. Layfield, *Science*, 2018, **362**, 1400–1403.

[33] M. J. Giansiracusa, A. K. Kostopoulos, D. Collison, R. E. P. Winpenny and N. F. Chilton, *Chem. Commun.*, 2019, **55**, 7025–7028.

[34] C. D. Pemmaraju, I. Rungger and S. Sanvito, *Phys. Rev. B*, 2009, **80**, 104422.

[35] D. M. Tomecka, V. Bellini, F. Troiani, F. Manghi, G. Kamieniarz and M. Affronte, *Phys. Rev. B*, 2008, **77**, 224401.

[36] A. Chiesa, S. Carretta, P. Santini, G. Amoretti and E. Pavarini, *Phys. Rev. Lett.*, 2013, **110**, 157204.

[37] A. Chiesa, S. Carretta, P. Santini, G. Amoretti and E. Pavarini, *Phys. Rev. B*, 2016, **94**, 224422.

[38] M. Valiev, E. Bylaska, N. Govind, K. Kowalski, T. Straatsma, H. Van Dam, D. Wang, J. Nieplocha, E. Apra, T. Windus and W. de Jong, *Computer Physics Communications*, 2010, **181**, 1477 – 1489.

[39] A. Abragam and B. Bleaney, *Electron Paramagnetic Resonance of Transition Metal Ions*, Clarendon, Oxford, 1970.

[40] E. Garlatti, T. Guidi, A. Chiesa, S. Ansbro, M. L. Baker, J. Ollivier, H. Mutka, G. A. Timco, I. Vitorica-Yrezabal, E. Pavarini, P. Santini, G. Amoretti, R. E. P. Winpenny and S. Carretta, *Chem. Sci.*, 2018, **9**, 3555–3562.

[41] M. Affronte, J. C. Lasjaunias and A. Cornia, *Eur. Phys. J. B*, 2000, **15**, 633–639.

[42] G. L. Squires, *Introduction to the Theory of Thermal Neutron Scattering*, Courier Corporation, 1996.

[43] A. Furrer, J. F. Mesot and T. Straessle, *Introduction to the Theory of Thermal Neutron Scattering*, World Scientific Publishing Company, 2009.

[44] S. W. Lovesey, *Theory of neutron scattering from condensed matter*, Clarendon Press; Oxford (UK), 1984.

[45] O. Arnold, J. Bilheux, J. Borreguero, A. Buts, S. Campbell, L. Chapon, M. Doucet, N. Draper, R. Ferraz Leal, M. Gigg, V. Lynch, A. Markvardsen, D. Mikkelson, R. Mikkelson, R. Miller, K. Palmen, P. Parker, G. Passos, T. Perring, P. Peterson, S. Ren, M. Reuter, A. Savici, J. Taylor, R. Taylor, R. Tolchenov, W. Zhou and J. Zikovsky, *Nuclear Instruments and Methods in Physics Research Section A: Accelerators, Spectrometers, Detectors and Associated Equipment*, 2014, **764**, 156 – 166.

[46] R. Bewley, R. Eccleston, K. McEwen, S. Hayden, M. Dove, S. Bennington, J. Treadgold and R. Coleman, *Physica B: Condensed Matter*, 2006, **385-386**, 1029 – 1031.

[47] M. Russina and F. Mezei, *Nuclear Instruments and Methods in Physics Research Section A: Accelerators, Spectrometers, Detectors and Associated Equipment*, 2009, **604**, 624 – 631.

[48] M. A. Nielsen and I. L. Chuang, *Quantum Computation and Quantum Information*, Cambridge University Press, Cambridge, England, 2000.

[49] S. M. Barnett, *Quantum Information*, Oxford University Press, 2009.

[50] J. Kempe, in *Approaches to Quantum Error Correction*, ed. B. Duplantier, J.-M. Raimond and V. Rivasseau, Birkhäuser Basel, Basel, 2007, pp. 85–123.

[51] B. Terhal, *Rev. Mod. Phys.*, 2015, **87**, 307.

[52] F. Arute and et al., *Nature*, 2019, **574**, 505.

[53] IBM, *Qiskit: Open-Source Quantum Development*.

[54] E. Pednault, J. Gunnels, D. Maslov and J. Gambetta, *On "Quantum Supremacy"*, 2019.

[55] P. W. Shor, *Phys. Rev. A*, 1995, **52**, R2493–R2496.

[56] A. M. Steane, *Phys. Rev. Lett.*, 1996, **77**, 793–797.

[57] P. W. Shor, Proceedings 35th Annual Symposium on Foundations of Computer Science, 1994, pp. 124–134.

[58] G. Aromí, V. Velasco, L. A. Barrios, M. Schütze, O. Roubeau, F. Luis, S. J. Teat and D. Aguilá, *Chem. Eur. J.*, 2019, **25**, 15228.

[59] J. H. V. Vleck, *The Theory of Electric and Magnetic Susceptibilities*, Oxford University Press, 1932.

[60] E. Macaluso, M. Rubín, D. Aguilà, A. Chiesa, L. A. Barrios, J. I. Martínez, P. J. Alonso, O. Roubeau, F. Luis, G. Aromí and S. Carretta, *Chem. Sci.*, 2020, **11**, 10337–10343.

[61] S. Stoll and A. Schweiger, *Journal of Magnetic Resonance*, 2006, **178**, 42 – 55.

[62] S. Stoll, *Ph.D. thesis*, ETH Zurich, 2003.

[63] O. J.W., *Electron paramagnetic resonance*, Gordon and Breach, 1969.

[64] J. Pilbrow, *Journal of Magnetic Resonance (1969)*, 1984, **58**, 186 – 203.

[65] E. Moreno-Pineda, M. Damjanovic, O. Fuhr, W. Wernsdorfer and M. Ruben, *Angew. Chem. Int. Ed.*, 2017, **56**, 9915–9919.

[66] H.-P. Breuer and F. Petruccione, *The Theory of Open Quantum Systems*, Oxford University Press, 2007.

[67] M. D. Jenkins, Y. Duan, B. Diosdado, J. J. García-Ripoll, A. Gaita-Arino, C. Giménez-Saiz, P. J. Alonso, E. Coronado and F. Luis, *Phys. Rev. B*, 2017, **95**, 064423.

[68] L. Hu, Y. Ma, W. Cai and et. al., *Nat. Phys.*, 2019, **15**, 503–508.

[69] E. Knill and R. Laflamme, *Phys. Rev. A*, 1997, **55**, 900–911.

[70] K. Bader, D. Dengler, S. Lenz, B. Endeward, S.-D. Jiang, P. Neugebauer and J. van Slageren, *Nat. Commun*, 2014, **5**, 5304.

[71] A. Chiesa, E. Macaluso, F. Petiziol, S. Wimberger, P. Santini and S. Carretta, *The Journal of Physical Chemistry Letters*, 2020, **11**, 8610–8615.

[72] D. D'Alessandro, *Introduction to Quantum Control and Dynamics.*, Chapman and Hall/CRC Applied Mathematicsand Nonlinear Science, CRC Press, 2007.

[73] Y.-S. Ding, K. X. Yu, D. Reta, F. Ortu, R. E. P. Winpenny, Y.-Z. Zheng and N. F. Chilton, *Nat. Comm.*, 2018, **9**, 3134.

[74] Y.-S. Ding, T. Han, Y.-Q. Zhai, D. Reta, N. F. Chilton, R. E. P. Winpenny and Y.-Z. Zheng, *Chemistry – A European Journal*, 2020, **26**, 5893–5902.

[75] Y.-S. Ding, N. F. Chilton, R. E. P. Winpenny and Y.-Z. Zheng, *Angew. Chem., Int. Ed.*, 2016, **55**, 16071–16074.

[76] K. Randall McClain, C. A. Gould, K. Chakarawet, S. J. Teat, T. J. Groshens, J. R. Long and B. G. Harvey, *Chem. Sci.*, 2018, **9**, 8492–8503.

[77] G. A. Craig and M. Murrie, *Chem. Soc. Rev.*, 2015, **44**, 2135–2147.

[78] M. N. Leuenberger and D. Loss, *Phys. Rev. B*, 2000, **61**, 1286–1302.

[79] V. S. Parmar, F. Ortu, X. Ma, N. F. Chilton, R. Clérac, D. P. Mills and R. E. P. Winpenny, *Chemistry – A European Journal*, 2020, **26**, 7774–7778.

[80] S. J. Clark, M. D. Segall, C. J. Pickard, P. J. Hasnip, M. I. J. Probert, K. Refson and M. C. Payne, *Zeitschrift für Kristallographie - Crystalline Materials*, 2005, **220**, 567 – 570.

[81] A. Togo and I. Tanaka, *Scr. Mater.*, 2015, **108**, 1–5.

[82] P. Giannozzi, O. Andreussi, T. Brumme, O. Bunau, M. B. Nardelli, M. Calandra, R. Car, C. Cavazzoni, D. Ceresoli, M. Cococcioni, N. Colonna, I. Carnimeo, A. D. Corso, S. de Gironcoli, P. Delugas, R. A. D. Jr, A. Ferretti, A. Floris, G. Fratesi, G. Fugallo, R. Gebauer, U. Gerstmann, F. Giustino, T. Gorni, J. Jia, M. Kawamura, H.-Y. Ko, A. Kokalj, E. Küçükbenli, M. Lazzeri, M. Marsili, N. Marzari, F. Mauri, N. L. Nguyen, H.-V. Nguyen, A. O. de-la Roza, L. Paulatto, S. Poncé, D. Rocca, R. Sabatini, B. Santra, M. Schlipf, A. P. Seitsonen, A. Smogunov, I. Timrov, T. Thonhauser, P. Umari, N. Vast, X. Wu and S. Baroni, *Journal of Physics: Condensed Matter*, 2017, **29**, 465901.

[83] P. Giannozzi, S. Baroni, N. Bonini, M. Calandra, R. Car, C. Cavazzoni, D. Ceresoli, G. L. Chiarotti, M. Cococcioni, I. Dabo, A. Dal Corso, S. de Gironcoli, S. Fabris, G. Fratesi, R. Gebauer, U. Gerstmann, C. Gougoussis, A. Kokalj, M. Lazzeri, L. Martin-Samos, N. Marzari, F. Mauri, R. Mazzarello, S. Paolini, A. Pasquarello, L. Paulatto, C. Sbraccia, S. Scandolo, G. Sclauzero, A. P. Seitsonen, A. Smogunov, P. Umari and R. M. Wentzcovitch, *Journal of Physics: Condensed Matter*, 2009, **21**, 395502.

[84] P. Giannozzi, O. Baseggio, P. Bonfà, D. Brunato, R. Car, I. Carnimeo, C. Cavazzoni, S. de Gironcoli, P. Delugas, F. Ferrari Ruffino, A. Ferretti, N. Marzari, I. Timrov, A. Urru and S. Baroni, *The Journal of Chemical Physics*, 2020, **152**, 154105.

[85] A. Chiesa, F. Cugini, R. Hussain, E. Macaluso, G. Allodi, E. Garlatti, M. Giansiracusa, C. A. P. Goodwin, F. Ortu, D. Reta, J. M. Skelton, T. Guidi, P. Santini, M. Solzi, R. De Renzi, D. P. Mills, N. F. Chilton and S. Carretta, *Phys. Rev. B*, 2020, **101**, 174402.

[86] S. Thiele, F. Balestro, R. Ballou, S. Klyatskaya, M. Ruben and W. Wernsdorfer, *Science*, 2014, **344**, 1135–8.

[87] C. Godfrin, A. Ferhat, R. Ballou, S. Klyatskaya, M. Ruben, W. Wernsdorfer and F. Balestro, *Phys. Rev. Lett.*, 2017, **119**, 187702.

[88] L. Bogani and W. Wernsdorfer, *Nature Mater.*, 2008, **7**, 179–186.

[89] R. Vincent, S. Klyatskaya, M. Ruben, W. Wernsdorfer and F. Balestro, *Nature*, 2012, **488**, 357–360.

[90] E. Burzurí, A. S. Zyazin, A. Cornia and H. S. J. van der Zant, *Phys. Rev. Lett.*, 2012, **109**, 147203.

[91] T. Sanada, T. Suzuki, T. yoshida and S. Kaizaki, *Inorg. Chem.*, 1998, **37**, 4712–4717.

[92] G. A. Timco, E. J. L. McInnes and R. E. P. Winpenny, *Chem. Soc. Rev.*, 2013, **42**, 1796–1806.

[93] S. Thiele, F. Balestro, R. Ballou, S. Klyatskaya, M. Ruben and W. Wernsdorfer, *Science*, 2014, **344**, 1135–1138.

[94] M. Urdampilleta, S. Klayatskaya, M. Ruben and W. Wernsdorfer, *ACS Nano*, 2015, **9**, 4458–4464.

[95] S. Wagner, F. Kisslinger, S. Ballmann, F. Schramm, R. Chandrasekar, T. Bodenstein, O. Fuhr, D. Secker, K. Fink, M. Ruben and H. B. Weber, *Nature Nano*, 2013, **8**, 575–579.

[96] L. Zhang, A. Bagrets, D. Xenioti, R. Korytár, M. Schackert, T. Miyamachi, F. Schramm, O. Fuhr, R. Chandrasekar, M. Alouani, M. Ruben, W. Wulfhekel and F. Evers, *Phys. Rev. B*, 2015, **91**, 195424.

[97] S. Ansbro, E. Moreno-Pineda, W. Yu, J. Ollivier, H. Mutka, M. Ruben and A. Chiesa, *Dalton Trans.*, 2018, **47**, 11953–11959.

[98] A. Donarini, M. Niklas, M. Schafberger, N. Paradiso, C. Strunk and M. Grifoni, *Nat. Commun.*, 2019, **10**, 381.

[99] Y. Nagaoka, *Phys. Rev.*, 1966, **147**, 392–405.

[100] S. F. Boys, *Rev. Mod. Phys.*, 1960, **32**, 296–299.

[101] A. Chiesa, E. Macaluso, P. Santini, S. Carretta and E. Pavarini, *Phys. Rev. B*, 2019, **99**, 235145.

[102] L. Zhang, A. Bagrets, D. Xenioti, R. Korytár, M. Schackert, T. Miyamachi, F. Schramm, O. Fuhr, R. Chandrasekar, M. Alouani, M. Ruben, W. Wulfhekel and F. Evers, *Phys. Rev. B*, 2015, **91**, 195424.

Acknowledgements

First and foremost I would like to thank Prof. Stefano Carretta, Dr. Alessandro Chiesa, Dr. Elena Garlatti and Prof. Paolo Santini, who all guided me in the last three years. Starting from scratch in a completely different field would have been much more difficult without their passion, advices and expertise to support me. I am truly grateful for the scientific landscape which I had the privilege to glance on and for the unique opportunities I had during my PhD. With them I would also like to thank the rest of the Magnetism Research Group, together with Dr. Francesco Petiziol and Prof. Sandro Wimberger, all of which I had the pleasure of collaborating with here in Parma. I would also like to thank all collaborators from different universities (Barcelona, Zaragoza, Manchester) that made (literally) possible all the research work exposed in this thesis. In this regard I address special thanks to Dr. Tatiana Guidi, who carefully instructed me during my two weeks at ISIS neutron and muon source and who organized last year's school on neutron and muons for magnetism. In a much more general way, I extend my thanks to the organizers of all the schools, conferences, meetings and workshops which I had the pleasure to participate in: they really do something special for all students! Since I'm still writing in English, I take this opportunity to thank all the nice people I met in schools and conferences, with which I had really interesting conversations as well as a really good time. There's no good science without good people.

A questo punto passo volentieri all'italiano, per ringraziare innanzitutto tutto il personale del dipartimento di fisica: non temete, continuerete a perdere contro di me al fantacalcio di dipartimento. Tra loro un ringraziamento speciale spetta a tutti gli (ex-)studenti e (ex-)dottorandi con cui ho condiviso le pause pranzo e tutti i momenti, migliori o peggiori che siano, di questi tre anni. Ovviamente un grazie a tutti i miei amici al di fuori del dipartimento: non ho bisogno di fare nomi dato che starei qui fino a domani ma sappiate che il tempo passato insieme è sempre stato per me la priorità in questi anni, anche quando non sono stato molto presente. Ringrazio la mia famiglia per il costante supporto e per i preziosi consigli di vita ma anche scientifici sui quali ho sempre potuto contare. Ringrazio i vari gruppi di D&D con cui ho avuto il piacere di vivere una realtà parallela assurda quasi quanto le leggi della realtà che ho studiato negli ultimi 8 anni (ricordo ora che una delle primissime sessioni della mia vita è stata la sera che avevo scoperto di aver vinto questo posto di dottorato). Ringrazio ifnine il circolo ARCI Argonne per avermi dato un posto in cui stare in questa strana estate di questo strano anno facendomi sentire a casa ogni giorno. Potrei ampliare ogni frase appena scritta e raddoppiare il volume di questa tesi solo per spendere buone parole per le persone fantastiche da cui sono circondato, ma ormai è da sottomettere.

We will never know world peace,
until three people can simultaneously
look each other straight in the eye.